UNIVERSIDADE D
COIMBRA

Catarina Guerra Batista

Brain response functions and neurovascular coupling in Type 2 Diabetes: insights from fMRI

Thesis submitted to the Faculty of Science and Technology of the University of Coimbra for the degree of Master in Biomedical Engineering with specialization in Image and Radiation, supervised by Professor Miguel Castelo Branco, PhD and João Valente Duarte, PhD.

December 2020

1 2 9 0

FACULDADE DE CIÊNCIAS E TECNOLOGIA
UNIVERSIDADE D COIMBRA

Brain response functions and neurovascular coupling in Type 2 Diabetes: insights from fMRI

Catarina Guerra Batista

Thesis submitted to the Faculty of Sciences and Technology of the University of Coimbra
for the degree of Master in Biomedical Engineering with specialization in Image and Radiation

Supervisors:
Professor Miguel Castelo Branco, PhD (Advisor)
João Valente Duarte, PhD (Advisor)

Faculty of Medicine, University of Coimbra, Coimbra, Portugal
ICNAS - Institute of Nuclear Sciences Applied to Health, University of Coimbra, Coimbra, Portugal
CIBIT - Coimbra Institute for Biomedical Imaging and Translational Research, University of Coimbra, Coimbra, Portugal

Coimbra, December 2020

This work was developped in collaboration with:

Faculty of Medicine, University of Coimbra

ICNAS - Institute of Nuclear Sciences Applied to Health, University of Coimbra

CIBIT - Coimbra Institute for Biomedical Imaging and Translational Research, University of Coimbra

Dedication

Em primeiro lugar, gostaria de agradecer aos meus orientadores, o Professor Doutor Miguel Castelo Branco e o Doutor João Duarte Valente, por me terem concedido a oportunidade de poder trabalhar neste projeto inovador - que me fez sentir como parte de algo bem maior e, cuja técnica desde cedo me fascinou e me fez pensar mais além -, pelas condições que me disponibilizaram para o poder concretizar, pelas aprendizagens que me proporcionaram, pelo incentivo e feedback, e pela compreensão e paciência que tiveram comigo durante todo este trajeto.

Expresso também a minha mais profunda gratidão por esta cidade, que passou a ser *Casa* para mim, e onde fui verdadeiramente feliz. Foram cinco anos de desafios e lutas, de novas experiências e aventuras, que muito me permitiram aprender, crescer e tornar-me na pessoa que hoje sou. Foram também cinco anos de muitas histórias para um dia contar e de várias pessoas que me marcaram e que levo para a vida. Ao Carlos, pelo teu apoio e presença incondicionais, pela tua grande paciência, por todos os bons momentos, por me fazeres sorrir como mais ninguém consegue, por toda a ajuda, conselhos e ensinamentos e por me teres feito crescer imenso enquanto pessoa. Aos meus afilhados Leonie, Pedro, Rita e *Beta*, por me terem deixado entrar no vosso percurso académico e acompanhado cada etapa ao detalhe, celebrando cada vitória e estando lá sempre quando e para o que foi preciso, e por termos criado a forte ligação que até hoje em dia mantemos e que muito prezo em continuar. À Mariana e à *Sis*, pelas longas amizades, pelo apoio, conselhos e longos desabafos, independentemente da distância a que nos encontremos. À Ana Rita e à *maltinha de LM*, por nunca me falharem, por todos os jantares épicos, cafés, gargalhadas e por me darem a conhecer outros mundos. A Cristo e à Sampaio, por terem sido as minhas *bússolas* desde o momento em que comecei este trajeto, guiando-me, ajudando-me e aconselhando-me sempre que precisei, e por todas as memórias que partilhamos. Ao Tiago e a muitos outros amigos e colegas que, através do seu bom companheirismo, permitiram tornar Coimbra um sítio bem mais acolhedor, e que sem dúvida não seria o mesmo sem todos os momentos partilhados.

Por fim, gostaria também de agradecer à minha família, pelo incentivo e por assegurarem que nada me faltasse para poder alcançar os meus objetivos.

Abstract

Type 2 Diabetes *Mellitus* (T2DM) is an epidemic metabolic disease that promotes multiple vascular complications and potentially alters human neurophysiology, with growing evidence of an association with the increased risk for brain function loss, long-term cognitive impairment and dementia. Pathophysiological vascular changes can influence the blood flow regulation in cerebral microvasculature, possibly impairing the neurovascular coupling. As non-invasively studied with functional magnetic resonance imaging, decreases in the Blood Oxygenation Level-Dependent (BOLD) signal may reflect low neuronal activity or inefficient neurovascular coupling, thus underlying brain function impairments might be undistinguishable. Therefore, it becomes crucial to understand the neurobiological correlates of early brain dysfunction in this pathology.

In this project, it was questioned whether the Hemodynamic Response Function (HRF) would be compromised in individuals with T2DM, whether it would depend on the brain region or would instead represent a general cortical phenomenon and/or whether it would rely on the displayed type of stimulus by measuring the BOLD response to performance-matched visual motion stimuli. Anatomical and functional magnetic resonance data from 141 subjects (64 patients with T2DM and 77 healthy controls) in response to the aforementioned psychophysical stimulation task, which was separately implemented in two classes of paradigms - block and event-related paradigms, were processed. The analysis of the processed data concerning the block stimulation task allowed to localize activated brain regions, in which, by a deconvolution, we extracted the HRF during the event-related stimulation task. Ultimately, the differences between the HRFs of the two populations were assessed.

Overall, and as expected, diabetic participants revealed significantly different HRFs. Notably, this outcome extended to all brain regions, regardless of the type of stimulus, suggesting that this is a general phenomenon. Diabetic participants displayed HRFs with higher variability, more sluggish, and with lower peak amplitude. The HRFs in these participants also included an initial dip, which was larger than the controls', and when it was witnessed, a less prominent, but a later and longer undershoot. Most HRF parameters were significantly different between the two populations, with diabetic participants presenting a higher dispersion and variability. Furthermore, they also displayed a higher peak latency and lower relative slope to peak, area under the curve, positive curve section area, and negative curve section area.

In short, the results unveiled an impaired HRF in the early stages of T2DM, which may be due to a neurovascular uncoupling without neurosensory deficits, as demonstrated by preserved

perceptual thresholds. Therefore, the HRF is proven to be a relevant tool in functional studies about the mentioned pathology, and it should be considered as a biomarker in the development and testing of therapeutic strategies in patients with T2DM. However, further research regarding neurovascular coupling and its mechanisms is required to better understand and potentially halt the deterioration of the brain function in T2DM.

Keywords: BOLD signal, Brain Imaging, Cerebral Hemodynamics, Hemodynamic Response Function, Magnetic Ressonance Imaging, Neurovascular Coupling, Type 2 Diabetes *Mellitus*

Resumo

A Diabetes *Mellitus* Tipo 2 (T2DM) é uma doença metabólica de caráter epidémico que promove várias complicações vasculares e potencialmente altera a neurofisiologia humana, tendo evidências crescentes de uma associação com o risco acrescido de desenvolvimento de perda de função cerebral, danos cognitivos a longo prazo e demência. Alterações vasculares patofisiológicas podem influenciar a regulação do fluxo sanguíneo na microvasculatura cerebral, possivelmente danificando o acoplamento neurovascular. Como estudado de forma não invasiva pela imagem por ressonância magnética funcional, decréscimos do sinal Dependente do Nível de Oxigenação Sanguínea (BOLD) podem refletir baixa atividade neuronal ou acoplamento neurovascular pouco eficiente, pelo que as deficiências subjacentes da função cerebral podem ser indistinguíveis. Deste modo, torna-se fulcral a compreensão das correlações neurobiológicas da disfunção cerebral precoce nesta patologia.

Neste projeto questionou-se se a Função de Resposta Hemodinâmica (HRF) estaria comprometida em indivíduos com T2DM, se dependeria da região cerebral ou se representaria um fenómeno cortical geral e/ou se seria influenciada pelo tipo de estímulo exibido ao medir a resposta BOLD a estímulos *performance-matched* de movimento visual. Foram processados os dados anatómicos e funcionais de ressonância magnética pertencentes a 141 sujeitos (64 participantes com T2DM e 77 controlos saudáveis), relativos à tarefa de estimulação psicofísica anteriormente mencionada, que foi implementada distintamente em duas classes de paradigmas - paradigmas de blocos e *event-related*. A análise dos dados processados referentes à tarefa de estimulação de blocos permitiu localizar as regiões do cérebro por esta ativadas, nas quais, por meio de uma desconvolução, se extraiu a HRF durante a tarefa de estimulação de eventos. Por fim, foram avaliadas as diferenças entre as HRFs das duas populações.

De forma geral, e como esperado, os participantes diabéticos apresentavam HRFs significativamente diferentes. Notavelmente, este resultado estendeu-se a todas as regiões do cérebro, independentemente do tipo de estímulo, sugerindo tratar-se de um fenómeno geral. Os participantes diabéticos exibiam HRFs com maior variabilidade, mais lentas e com menor amplitude de pico. As HRFs destes participantes também incluíam um *initial dip*, maior que o dos controlos, e, quando observado, um *undershoot* menos evidente, porém mais tardio e longo. A maioria dos parâmetros da HRF era significativamente diferente entre as duas populações, sendo a dispersão e a variabilidade maiores nos participantes diabéticos. Para além disso, também evidenciavam uma maior latência de pico e menores declive relativo até ao pico, área abaixo da curva, área da

secção positiva da curva e área da secção negativa da curva.

Em suma, os resultados revelaram uma HRF comprometida nos estádios iniciais da T2DM, que se poderá dever a um desacoplamento neurovascular sem défices neurossensoriais, como demonstrado pelos limiares percetuais preservados. Deste modo, a HRF mostra ser uma ferramenta importante em estudos funcionais sobre a patologia mencionada, e deve ser considerada como um biomarcador no desenvolvimento e teste de estratégias de terapêutica nestes pacientes. No entanto, deve ser feita mais investigação relativamente ao acoplamento neurovascular e aos seus mecanismos para melhor entender e potencialmente prevenir a deterioração da função cerebral na T2DM.

Keywords: Sinal BOLD, Imagiologia Cerebral, Hemodinâmica Cerebral, Função de Resposta Hemodinâmica, Imagem por Ressonância Magnética, Acoplamento Neurovascular, Diabetes *Mellitus* Tipo 2

List of Acronyms

AMR - Anatomical Magnetic Resonance project

AR(1) - First-order autoregression process

AR(2) - Second-order autoregression process

ASL - Arterial Spin Labeling

AUC - Area Under the Curve

BA - Brodmann Area

BBB - Blood-Brain Barrier

BBR - Boundary-Based Registration

BOLD - Blood Oxygenation Level-Dependent

CBF - Cerebral Blood Flow

CBV - Cerebral Blood Volume

$CMRO_2$ - Cerebral Metabolic Rate of Oxygen

CV - Coefficient of Variation

DCM - Dynamic Causal Modelling

DICOM - Digital Imaging and Communications in Medicine

EPI - Echo-Planar Imaging

FA - Fine-Tuning Alignment

FDR - False Discovery Rate

FFT - Fast Fourier Transform

FID - Free Induction Decay

FMR - Functional Magnetic Resonance project

fMRI - Functional Magnetic Resonance Imaging

FOV - Field of View

FWHM - Full Width at Half Maximum

GE - Gradient Echo

GLM - General Linear Model

GRE - Gradient Refocused Echo

HRF - Hemodynamic Response Function

IA - Initial Alignment

IIHC - Intensity Inhomogeneity Correction

ISI - Inter-Stimulus Interval

MNI - Montreal Neurological Institute

MPRAGE - Magnetization-Prepared Rapid Gradient Echo

MR - Magnetic Resonance

MRI - Magnetic Resonance Imaging

MVPA - Multi-Voxel Pattern Analysis

NCSA - Negative Curve Section Area

NGF - Normalized Gradient Fields

NVC - Neurovascular Coupling

NVU - Neurovascular Unit

PCSA - Positive Curve Section Area

PET - Positron Emission Tomography

RF - Radio Frequency

RFX - Random-effects Analysis

ROI - Region of Interest

SNR - Signal-to-Noise Ratio

T1-w - T1-Weighted

T2DM - Type 2 Diabetes *Mellitus*

TE - Echo Time

TI - Inversion Time

TR - Repetition Time

VMR - Volumetric Magnetic Resonance project

VTC - Volume Time Course

Other Abbreviations

Biological and Chemical Abbreviations

20-HETE - 20-hydroxyeicosatetraenoic acid

AA - araquidonic acid

AMPA - α-amino-3-hydroxy-5-methyl-4-isoxazole epropionic acid receptor

ATP - adenosine triphosphate

BK - Large-conductance calcium-activated potassium channels

Ca^{2+} - calcium ion

CO_2 - carbon dioxide

dHb - deoxyhemoglobin

EET - epoxyeicosatrienoic acid

H^+ - proton

HbO_2 - oxyhemoglobin

K^+ - potassium ion

K_{ir} - potassium inward-rectifier channels

mGluRs - Metabotropic glutamate receptors

NMDA - N-methyl-D-aspartate receptor

O_2 - oxygen

ROS - Reactive Oxygen Species

SMC - Smooth Muscle Cell

Symbols and Measurement Units

$^{\circ}$ - degrees

a.u. - Arbitrary units

$\mathbf{B_0}$ - External Magnetic Field

CNT - Control subjects

Hz - hertz

M - Net Magnetization Vector

MHz - megahertz

mm - millimeters

ms - milliseconds

$\mathbf{M_{xy}}$ - Net Magnetization Vector (transverse component)

$\mathbf{M_z}$ - Net Magnetization Vector (longitudinal component)

pH - Potential of Hydrogen

s - seconds

T - Tesla

List of Figures

List of Tables

Contents

1

Introduction

Type 2 Diabetes *Mellitus* (T2DM) is a multifactorial metabolic disorder and it has become an increasingly serious health problem, being the sixth leading cause of disability in 2015 [1, 2]. T2DM is the world's most common type of diabetes, representing about 90% of all Diabetes *Mellitus* cases [3]. This disease currently affects 422 million people worldwide and is tightly correlated with 1.6 million deaths per year [4]. Furthermore, an estimated 193 million people have undiagnosed diabetes, and an additional 318 million people are at a preclinical state of impaired glucose regulation, although, through lifestyle adjustments, pharmacotherapy, or both, the flourishing of T2DM may be reversed or delayed [2].

Both the incidence and prevalence of T2DM have raised drastically and are tied to rising rates of multiple risk factors such as obesity, sedentary lifestyles, increased energy intake and reduced energy expenditure, and aging [2, 5]. It is projected an increase to 642 million people worldwide affected by T2DM by 2040 [2].

In order to mitigate the expected projections for this pathology and to improve the accuracy of early treatment with the aim of reducing the damage induced to its patients, and thus, contribute to the decrease of the death rates associated with this disease per year, new diagnostic and/or prognostic methods for T2DM have been developed and adopted. The vast majority of them are structural methods. However, there are still several functional methods to be explored. This thesis aims to validate the feasibility of a medical imaging functional biomarker for T2DM by enabling the detection of the induced neurovascular damage as well as its location, resorting to the analysis of processed Functional Magnetic Resonance Imaging (fMRI) data.

1.1 Contextualization

In T2DM, also known as "non-insulin-dependent diabetes" [6], insulin resistance rises, that is, the peripheral tissues increasingly fail to recognize insulin [7] - which is produced in the pancreatic β-cells - as efficiently as they used to. As a result, the secreted insulin is no longer enough to suppress the increased levels of plasmatic glucose, causing hyperglycemia. Consequently, at an initial stage, the β-cells increase insulin production in order to balance its inefficient action, resulting in the onset of hyperinsulinemia [6]. In the short term, this response manages to work, however, in the long term, it becomes an unsustainable solution, as the β-cells become overloaded due to excessive insulin production - which is still unable to suppress the

induced hyperglycemia condition - and its function becomes compromised [6, 5]. Ultimately, they may collapse and stop producing insulin.

Although its specific driving forces are yet unknown, T2DM has several risk factors [6] associated with genetics and lifestyle [8], which affect its prevalence and incidence [9]. Some of them include overweight, high-calorie diet, reduced physical activity, race/ethnicity, perinatal factors (e.g. nutrition in the womb), family history of diabetes, or other co-morbidities (e.g. hypertension) [9]. Nevertheless, the mechanisms underlying the individual differences in the predisposition to T2DM remain unexplained [5].

T2DM produces macro and microvascular disorders [5], which can cause long-term damage, dysfunction, and deterioration in several tissues and organs such as the pancreas, liver, kidneys, brain, eyes, small intestine, adipose tissue, heart, and blood vessels [2, 7], thus increasing morbidity and mortality [5]. Macrovascular disorders include hypertension, stroke, and cardiovascular, peripheral arterial, or cerebrovascular disease [6], and can change cerebral hemodynamics, chronic cerebral ischemia, hypoxia, and energy metabolism [1]. On the other hand, microvascular disorders comprise retinopathy with prospective vision loss, nephropathy leading to renal failure, peripheral neuropathy with increased risk of limb ulcers or amputations [7], endothelial dysfunction, micro-vessel formation, and basement membrane thickening at a microvascular level [1]. However, these disorders have a tremendously difficult early detection.

So far, there is still no cure for diabetes. However, it can be treated and controlled. In order to try to delay or prevent the development of diabetes-related health problems [10], insulin resistance may improve with lifestyle changes (healthy eating and regular exercise) [8], weight reduction, and/or pharmacological treatment of hyperglycemia, but is seldom restored to normal [6]. Also, since the autoimmune destruction of β-cells does not happen, at least initially and often throughout their lifetime, T2DM patients may not need insulin treatment to survive [6].

Due to its association with increased risk for brain function loss, long-term cognitive impairment and dementia [11, 12], in order to develop preventive interventions, it becomes crucial to understand the neurobiological correlates of early brain dysfunction in T2DM, which can be studied and evaluated by fMRI [12].

1.2 Objectives

The main goal of this project is to characterize and evaluate the Hemodynamic Response Function (HRF) in the brain of patients with T2DM, associating the response to neurosensory stimuli with visual motion perception paradigms, in order to allow its application in the prognosis and monitoring of neurovascular complications of this pathology.

Through an fMRI data analysis from a sample including healthy controls and patients with T2DM, the HRF of all participants in the several regions activated by a task performance will be estimated. Then, in each of these regions, the HRF parameters will be extracted and analyzed per group (diabetic subjects/controls) and region, to ascertain if significant differences prevail and in which region they take place, and thus, according to its location, understand what sort

of physiological changes arise with T2DM and what consequences they can cause.

In order to accomplish this goal, several sub-tasks were established:

1. Data collection: Functional and structural MRI data from control and Type 2 diabetic subjects were collected at ICNAS regarding the performance of a psychophysical task according to two paradigm classes: block and event-related paradigms.
2. Data processing: After its collection, the data were preprocessed, underwent structural-functional co-registration, and were normalized.
3. Obtainment of the regions involved in the task performed by the participants: The functional block paradigm data, after its processing, underwent a standard General Linear Model (GLM) analysis in order to get a map of the activations/deactivations provided in response to the task executed in this paradigm (further details about this step will be given in section 4.3.1.1).
4. HRF estimate for each participant: After the previously mentioned regions were obtained, the functional event-related processed data underwent a GLM deconvolution analysis (further details about this step will be given in section 4.3.1.2).
5. Evaluation of each group's data: After estimating the HRF for each participant, the average HRF and its parameters (peak amplitude, peak latency, relative slope to peak, area under the curve, positive section curve area, and negative section curve area) were determined in each region and group of participants, using MATLAB. Then, these were compared to correlate the obtained values with its underlying physiology, and consequently, to infer conclusions about its meaning.

1.3 Document Structure

This document is organized as it follows:

- Chapter 2 - Background Knowledge: The fundamental principles to understand this work are explained;
- Chapter 3 - State of Art: The literature review regarding the currently used paradigms in the fMRI, and the role of the HRF as a functional imaging biomarker, including in T2DM is pointed out;
- Chapter 4 - Material and Methods: The experimental procedure of the task and the methods applied in this work in order to achieve its intended purpose are described;
- Chapter 5 - Results: The achieved results in this work are presented and described;
- Chapter 6 - Discussion: The reasons underlying the obtained results are explained;
- Chapter 7 - Conclusion and Future Work: The conclusions of this work and its future directions are summarized;
- Appendices: Further results are presented.

2

Background Knowledge

2.1 Magnetic Resonance Imaging Principles

Magnetic Resonance Imaging (MRI) is a very comprehensive imaging technique with countless measurement methods that, by manipulating both static and dynamic magnetic fields and by using radio frequency pulses, collects and localizes proton signals which derive from their spin angular momentum and that are found all over the body. The resulting signals are then converted into digital images, representing the signal from each image voxel [13].

Given this, MRI produces high-contrast and high-resolution images with the aid of the natural magnetic properties of the body, without employing any kind of ionizing radiation [14, 15, 16]. It is also possible to further improve the Signal-to-Noise Ratio (SNR) and the resolution by enhancing the magnetic field strength, in order to obtain a clinically and diagnostically useful image [14, 13]. However, high field strength can cause artifacts, other sorts of technical issues and also physiological effects such as visual abnormalities [14].

This technique puts to good use the hydrogen protons existing in the human body due to its properties, since hydrogen is one of the most abundant nuclei in the human body, existing in organic molecules such as proteins or fatty acids, and in water, which composes about 70% of the human body [13]. The hydrogen nuclei consist of a single proton that carries a positive electrical charge and is constantly spinning around its axes. These spinning charged particles, therefore, produce their own magnetic field, which is called the magnetic moment [17]. Without any external magnetic field, these magnetic moments become randomly orientated, canceling each other out. Therefore, the summation of all the magnetic moments, the net magnetization vector (M), becomes null [18]. Nevertheless, when a strong and constant external magnetic field (B_0) is applied, they align either with (parallel) or against (antiparallel) the external field. There is no state in between [17]. What sets the alignment orientation is the amount of energy associated with each proton, as a consequence of the strength of B_0 as well as the temperature of the sample. Protons with a little extra energy, possibly from some local increased heat, will line up against the main magnetic field, and therefore, are in the high-energy state. That being said, protons lining up with the main magnetic field, require less energy and are in the low-energy state. Bearing this in mind, since less energy is required, most protons tend to align with B_0 than against it [17].

Furthermore, when protons are exposed to an external static magnetic field, they also move around the long axis of B_0. This motion is named precession and it is similar to movement of a spinning top. When spun, the top wobbles but does not fall over and the handle of the spinning top follows a circular path [17].

The precession rate, known as the Larmor frequency, is the number of times the protons precess per second, setting the value of a short burst of electromagnetic energy - known as the radio frequency (RF) pulse - transmitted to induce proton resonance or excitation [19, 17]. It is proportional to the intensity of B_0, as shown by the following expression, the Larmor equation: [19]

$$\omega = \gamma B \tag{2.1}$$

in which ω is the Larmor frequency (MHz), γ is the gyromagnetic ratio (MHz/T) and B is the intensity of B_0 (T) [19].

This precession movement produces both longitudinal and transverse components in the magnetic moments of the protons, resulting in a not null net magnetization vector. Since most protons align parallel with the z component of B_0 and they are not spinning in phase with each other, canceling each other out, the magnetization vector is mainly in the longitudinal direction (M_z), and consequently, the transverse component (M_{xy}) does not contribute considerably to M. Notwithstanding, it is worth noticing that even though the main net magnetization in the z-direction is precessing, the MRI receiver coil, which detects signals, perceives it as a stationary vector. Hence, only by performing a resonance phenomenon, in which an RF pulse is applied in the vicinity of the protons with the same frequency value as the precessional frequency of the protons, the Larmor frequency, the receiver coil can detect signals from the protons [19].

Therefore, when the RF pulses set at the Larmor frequency are applied, protons absorb energy and fall out of alignment with B_0, that is, they flip into the high energy state, aligning antiparallel to B_0 [17]. Thus, this state's spin population increases and protons move in phase with each other, that is, synchronized in the same direction and at the same rate, rather than moving randomly, a phenomenon known as phase coherence [19, 17]. Consequently, the net magnetization vector tips from its longitudinal axis into its transverse plane while still rotating about the z-axis at the Larmor frequency [19]. As a result, protons once again cancel each other out, which leads to a decrease in longitudinal magnetization and an increase in the net magnetization vector component that is perpendicular to the main magnetic field B_0 located in the x-y or transverse plane, known as the transverse magnetization vector, which moves in line with the precessing protons at the Larmor frequency [17].

However, the existing number of spins and the RF pulse amplitude and time length influence this process [19]. For instance, if the absorbed energy is high enough to push about 50% of the proton population into the high energy state, longitudinal magnetization becomes null as the opposing magnetic forces counterweight each other out [17].

Subsequently, if a conductive receiver coil is placed in the surroundings, the rotation of the transverse magnetization at the resonant frequency of the local protons will induce an alternating voltage across the coil, which in turn generates an electrical current. The latter can be collected with a coil or an antenna, producing a radio signal with the same frequency. Once the RF pulse is removed, the protons dephase, that is, they phase out with each other and precess separately, thus returning to their equilibrium state. Consequently, the relaxation processes - longitudinal and transverse relaxation - begin [17].

2.1.1 Relaxation processes

Longitudinal relaxation is a process in which the resonating protons return to their equilibrium energy state, dissipating its previously absorbed energy with their surroundings, the lattice, as heat. During this process, as molecules tumble, a fluctuating magnetic field is produced, to which protons in nearby molecules are exposed to. When this fluctuating magnetic field is closer to the Larmor frequency, the energy transfer, and thus, the longitudinal relaxation, becomes more favorable [17]. As a result, protons realign parallel to the external magnetic field, resetting the energetic spin populations to their initial state and causing a net increase in the longitudinal magnetization [19, 17, 14].

Since not all protons return to their original energy state at the same time, longitudinal relaxation is a continuous process, thus it is difficult to determine when it ends. Therefore, T1 is a relaxation constant which describes the longitudinal relaxation rate, in particular, the time needed for the longitudinal magnetization to recover from 0 to (1 - e^{-1}), or to approximately 63% of its final value. This value depends on the molecular motion frequency - the tumbling rate - of the molecule in which the proton resides, and is affected by tissue composition and structure [17].

However, different molecules have different tumbling rates, and thus, longitudinal relaxation can own different efficiencies. For instance, free water has a small molecular size and tumbles very rapidly, and hydrogen protons bound to large macromolecules which tumble very slowly. Hence, both have ineffective longitudinal relaxation, and subsequently, approximately long T1. Therefore, when water is partially bound, its tumbling rate can be slowed down to a rate closer to the Larmor frequency, resulting in a T1 value smaller than that in free water. On the other hand, fat has a short T1 value due to similarities between the frequencies of the carbon bonds located at the fatty acid endings and the Larmor frequency, which allow an efficient energy exchange [17].

Transverse relaxation is a process in which the magnetic spin of protons is affected by internal magnetic field inhomogeneities, that is, small magnetic field variations within the local tissue, from neighboring proton spins, which have a higher impact than the external magnetic field applied. Protons thus repel each other and move apart, phasing out progressively in the x-y plane, due to microscopic interactions between nearby protons, which cause random variations of the Larmor frequency of individual protons and, subsequently, an energy transfer between proton spins [19, 17]. As a result, transverse magnetization decreases and disappears [17].

T2 is the relaxation constant that describes the transverse relaxation rate, in particular, the time needed for the transverse magnetization to decay to e^{-1}, or approximately 37% of its initial value. Nevertheless, different molecules in different tissues have different spin-spin interactions, thus different transverse relaxation speeds. For instance, free water, which contains rapidly moving small molecules that are relatively far apart, has less spin-spin interactions and thus fewer field inhomogeneities, resulting in longer T2 values than in water-based tissues with large macromolecular content, since they interact more with each other [17].

As longitudinal relaxation requires mandatory energy exchange from the spin system, transverse relaxation may occur with or without overall energy loss. Therefore, transverse relaxation is usually much faster than longitudinal relaxation, resulting in T2 values always less or equal than T1 [17].

However, in fact, inhomogeneities in B_0 are also possible, resulting in a phase coherence loss process which produces slightly different Larmor frequencies in protons at different locations within the field. This dephasing has not a random disposition since it is caused by a constant, thus it can be potentially reversible.

Consequently, considering the effects caused by transverse relaxation and by B_0 inhomogeneities, protons dephase at a different rate, T2* [19]. This rate is shorter than T2 because spins dephase much quicker due to B_0 inhomogeneities rather than transverse relaxation. Its length depends on the number of inhomogeneities existing in the magnetic field, that is, the shorter T2* is, more inhomogeneities exist in the magnetic field. Using T2* relaxation, it is possible to determine the actual rate of decay observed when a Free Induction Decay (FID) signal is measured [17].

2.2 Functional Magnetic Resonance Imaging

fMRI is a non-invasive technique based on MRI, with excellent temporal and good spatial resolution, which allows to study brain function, linking neuronal activity and hemodynamics [20, 21] by mapping the patterns of brain activation and connectivity. The most widely used method is based on the Blood Oxygenation Level-Dependent (BOLD) signal change, which is due to small changes in blood flow and oxygen metabolism associated with neuronal activity, either in response to a specific task or when at rest [22, 23].

2.2.1 The Blood Oxygenation Level-Dependent signal

The BOLD signal takes advantage of the hemoglobin oxygenation state differences caused by neural metabolism, that result in magnetic field changes surrounding the red blood cells [24, 25], and therefore affect the magnetic resonance (MR) signal intensity. This intrinsic contrast mechanism based on the oxygenated/deoxygenated hemoglobin ratio in the blood does not directly measure neuronal activity itself and its underlying physiology, but instead measures the neuronal metabolic demands. BOLD contrast allows to indirectly study the hemodynamic responses to neural firing [26], by reflecting the dynamic interaction between neural activity,

the Cerebral Metabolic Rate of Oxygen ($CMRO_2$), the Cerebral Blood Flow (CBF), and the Cerebral Blood Volume (CBV) [27]. Besides, it also eases the recognition of brain areas or networks where neuronal activity is modulated during a certain task or function since it is co-localized with the neuronal activation site [28].

BOLD contrast uses several T2*-weighted MRI sequences, in which each voxel represents a certain spatial location with an associated specific intensity depending on the T2* signal differences, since this signal's sensitivity to local magnetic inhomogeneities is caused by neurovascular changes that accompany psychological and behavioral functions [27, 29]. Hence, by cracking the voxel value in each of the subsequent images, a time series of intensity values in that spatial location across time can be obtained. Therefore, the BOLD signal is used as a biomarker for neural activity [29], highlighting magnetic uniformity effects to create high contrast images [24].

Besides its relatively high sensitivity and simplicity of measurement, due to the Gradient Echo (GE) acquirement, BOLD contrast adds a further feature to MRI, by providing a dynamic time window of the hemodynamic response, due to the fMRI's high temporal resolution [26, 30]. However, BOLD contrast has its disadvantages. First, its spatial resolution may be good but it is limited, since the BOLD signal includes contributions from veins that irrigate nearby activated regions, especially in large surface vessels, when they receive more oxygenated venous blood from the aforementioned areas [23]. As a result, signaling alterations between the brain and the vasculature might seriously confound BOLD interpretation [28]. Given that, this contrast only recognizes a certain share of neural activity changes caused by a specific task or physiological state. Therefore, if the net metabolic demand of some regions is not modified, changes in neural activity may be displayed, even when the latter is missed [31]. Secondly, the BOLD signal has a complex interpretation [26, 30] and cannot provide information on blood flow changes before applying any stimulus [24]. And lastly, it has a slow response time, which, on one hand, easily allows to measure and to track slow neural events, but, on the other hand, can induce an overlap of fMRI signals in neural events shorter than the fMRI response time, making it harder to resolve individual events [23].

2.2.1.1 The physiological basis of the BOLD signal

When a brain region becomes more active, neural firing and other signaling processes - such as the production and propagation of action potentials, the release of neurotransmitters across the synaptic gap or their reception and regeneration of action potentials in the postsynaptic structures - increase. As a result, energy requirement locally increases, which, in turn, raises $CMRO_2$ in the affected brain region. While the oxygen consumption caused by glycolysis in tissues surrounding the capillaries rises, accumulating its corresponding metabolites, a few seconds later, several chemical signals (e.g. carbon dioxide (CO_2), nitric oxide (NO), protons (H^+)) induce the vasodilation of the capillary bed, which overcompensates the blood flow [31, 25], increasing both CBV and CBF. The net effect will depend on the interaction between $CMRO_2$, CBV, and CBF. However, CBF prevails upon CBV [27], and therefore, local oxygen (O_2) levels increase in order to overcome the transient deficit caused by the $CMRO_2$ raise [31, 25]. Nev-

ertheless, the CBF increase is disproportional to the $CMRO_2$ raise, meaning that the oxygen supply is greater that the required to balance its consumption - which is known as the CBF and $CMRO_2$ *uncoupling* [27, 25].

Consequently, the hemodynamic response takes place. The local O_2 concentration raise increases the oxygen extraction from oxygenated hemoglobin in the blood, known as oxyhemoglobin (HbO_2), thus becoming deoxygenated and increasing its concentration [28]. This hemoglobin variety, known as deoxyhemoglobin (dHb), which is paramagnetic and owns a strong magnetic moment, increases both in intravascular and extravascular spaces [25]. As the paramagnetic state further exposes iron atoms to the surrounding water [32, 27], tissue oxygenation decreases and the local magnetic susceptibility changes in the red blood cells, inducing magnetic susceptibility differences between the blood and the surrounding tissue [23]. Subsequently, these differences create an interaction between the bulk magnetization of the deoxygenated blood and the external magnetic field, producing small and local magnetic field gradients within and around the blood vessels [32]. The strength of these induced gradients relies on the magnetic susceptibility differences caused by hemoglobin oxygenated state changes and the external magnetic field strength [27], which in turn depend on hemoglobin concentration [25] since higher deoxyhemoglobin levels prompt stronger magnetic susceptibility differences [27]. Then, these gradients are detected by water protons, altering the signal decay, which is described by T2* time constant [23]. Therefore, T2* decreases, causing a faster signal decay and a local depletion in the BOLD signal regarding the surrounding tissues, thus producing a darker image of the veins [28, 26]. But, shortly after, the vasodilatory response reverts the aforementioned state, increasing the levels of oxyhemoglobin - which is diamagnetic, so it does not disturb the surrounding field and it is magnetically indistinguishable from brain tissue - and decreasing deoxyhemoglobin concentration, both in intravascular and extravascular spaces [25]. As a result, a more homogeneous magnetic field is produced, in which the T2* time constant is higher [28, 26], implying a reduced signal loss and an increased BOLD signal in the activated region [28], thus generating a lighter image of the veins [26]. Therefore, when the deoxyhemoglobin level varies, the relaxation of the water protons changes, and those variations become noticeable in fMRI [23]. As a conclusion, the BOLD signal stems from venous and capillary blood instead of arterial blood [31], and its variation depends on the balance between CBF, $CMRO_2$ and CBV changes of blood compartments that contain deoxyhemoglobin and on volume exchange effects which grow with the field strength [31, 33].

The susceptibility effects caused by deoxyhemoglobin modulate the T2 and T2* relaxation times of intravascular and extravascular blood signal, thus influencing BOLD signal change [25]. Although it may be smaller than the extravascular signal, the intravascular signal owns higher sensitivity to blood oxygenation since it is closer to deoxyhemoglobin. Consequently, the intravascular contribution likely accounts for half or more of the witnessed BOLD signal changes [33]. The modulation of the intravascular and extravascular signals is produced by, correspondingly, diffusion and intravoxel dephasing [25], and it depends on the selected field strength, pulse sequence, and time to echo [24]. Furthermore, the acquisition becomes more sensitive to T2* and T2 using a Gradient Refocused Echo (GRE) MRI pulse sequence. Below 3 T,

T2* contrast becomes predominant and largest in venules, whereas above the designated value, the diffusion-weighted T2 contrast gains further importance, providing deeper spatial specificity since signals generated in capillaries and tissue with spin-echo acquisitions are preferred [25].

2.3 The Hemodynamic Response Function

After a brief period of neural activity, the BOLD signal changes over time [34, 30]. This relationship is described in the HRF - the mathematical transfer function between neural activity and its corresponding BOLD fMRI signal [35]. The HRF is slow, enduring several seconds even with a very brief stimulus [34, 30, 36], and it is intrinsically delayed regarding neural activity, due to an hemodynamic lag induced by the increase in oxygen demands [37]. By convolving the HRF with a stimulus, it is possible to model the BOLD response and to gain more insights about it [31], such as to describe the set of local changes linked to neuronal activity that took place in CBV, CBF, and $CMRO_2$ [38], and to identify active brain regions [31].

The canonical HRF has a consistent shape [39], depicted by a gradual rise at 1 to 2 seconds after the onset of neural activity [31], peaking approximately 5 to 8 seconds after the neural activity reached its maximum. Then, a return to the baseline takes place roughly 12 seconds after the stimulus, and it is followed by a subsequent small post-stimulus undershoot [26] - a BOLD signal decrease which may persist tens of seconds before the signal returns to the baseline [40]. Ensuingly, the HRF stabilizes again, between 20 to 30 seconds after the mentioned onset, depending on the length of the stimulus [26]. On occasions, as illustrated in figure 2.1, it can be seen a small initial decrease below the baseline at the beginning of the HRF and before its peak, known as the *initial dip* [26, 33].

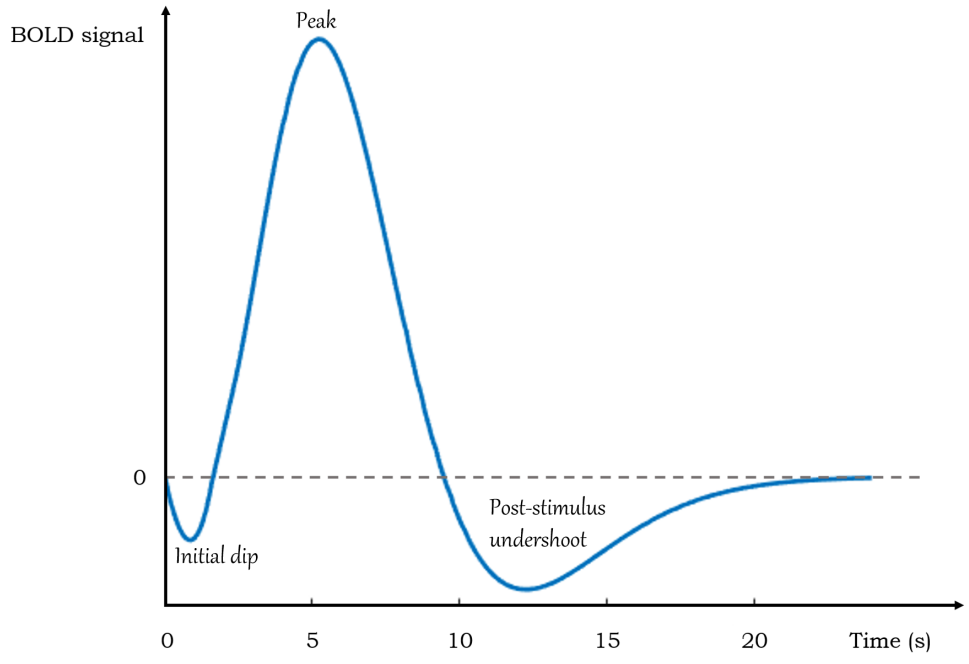

Figure 2.1: Example of an HRF with an initial dip. Adapted from Worsley et al. (2001) [41].

Given its higher spatial specificity for activations, the initial dip is more localized to neuronal activity areas than the HRF peak [31]. However, it is inconsistent, variable, and more frequently noticed in higher magnetic fields [42]. Therefore, this HRF segment so far has not been reliably observed, and thus, its existence remains controversial [31]. Furthermore, its physiological origin remains an open question since two different hypotheses have been presented to explain it [22, 42, 26, 33]. The first one postulates that, between the neural activity increase and the oxygenated blood inflow, there is an early increase in oxygen consumption ($CMRO_2$) [31]. As a consequence, blood oxygenation diminishes, and the deoxyhemoglobin concentration relatively increases, thus decreasing the BOLD signal [43]. Following this premise, the initial dip may be better localized to increased metabolism areas than the primary BOLD effect, since the CBF rise may include a broader area, and it may represent a transient uncoupling of CBF and oxygen metabolism [26]. The other hypothesis suggests that the initial dip may reflect an arterial CBV increase caused by volume exchange effects associated with magnetic field strength changes [42, 33].

In turn, the HRF peak is due to a local CBF rise, in which the oxygen supply increases disproportionately instead of just reaching a level that meets the area's metabolic needs [42]. Therefore, the oxygen becomes more supplied than consumed [31], causing an oversupply in oxygenated blood, and thus, the deoxyhemoglobin concentration decreases [43]. As a result, a transient increment in the oxyhemoglobin to deoxyhemoglobin ratio emerges, and the MR signal increases [42].

The post-stimulus undershoot is a variable segment of the HRF, and it is frequently seen in long-stimulus experiments [42]. However, there is still no consensus on its physiological origin since several possibilities have been presented to explain it. These include a neural activity undershoot, with CBF and $CMRO_2$ following along; a slow recovery of $CMRO_2$ after CBF and CBV returned to the baseline; a slow recovery of venous CBV after CBF and $CMRO_2$ returned to baseline; or a transient undershoot of CBF after $CMRO_2$ returned to baseline [33]. Therefore, in brief, there is an unclear connection between these parameters, which increases deoxyhemoglobin in previously active brain regions [31] as a result of reduced hemoglobin saturation in venous blood or increased venous/capillary blood volume [33]. Hence, the oxyhemoglobin to deoxyhemoglobin ratio decreases, so as the MR signal [42]. As a result, the HRF diminishes below the baseline level, and it is sustained at the end of the stimulus for approximately 10 seconds [31].

2.3.1 The non-linearity of the Hemodynamic Response Function

The HRF delay depends on the stimuli length. In brief sensory events, the HRF is wider and delayed for about 2 seconds after neuronal activity. However, in long neural events (events that last a second or more), the HRF presents a delay which lasts from 10 to 12 seconds after neuronal activity, causing longer recovery periods for certain and more subtle function segments. This does not mean that neuronal events must be well separated in time so that they can be determined [44], but that, overall and at first sight, the HRF summates roughly linearly, over trials and over time, implying that multiple consecutive HRFs from neural sequential events

tend to overlap [34, 44, 21]. Therefore, when a long set of repeated stimuli is applied, as long as the time between multiple stimuli surpasses 4 to 5 seconds, they can be added together almost linearly [42]. Thus, the individual HRFs produced by each stimulus are convolved with the stimuli, producing a resulting HRF which portrays the moving average of the individual HRFs. As a consequence, the HRF shape becomes wider, the peak turns into a sustained plateau, proportional to the stimuli length, and it returns to baseline only once the latter has ended [39]. Sometimes in these cases, considerable variations as a small initial undershoot, a slow ramp or an overshoot can be seen [42, 33].

However, when stimulus events are extremely rapid, the HRF has subtle but clear departures from linearity. This non-linearity is mainly temporal, affecting the HRF amplitude and response timing (such as latency or response width), and causes an over-prediction of the true response to extended stimuli by using a shifted and further response to a brief stimulus. This effect becomes even more pronounced when brief stimuli are shorter than 4 seconds and extended stimuli longer than 6 seconds. Nonetheless, this temporal non-linearity becomes reduced when short and long duration stimuli longer than approximately 4 seconds are compared [26].

The reason underlying these departures is yet to be completely understood, since the non-linearities may reflect an intrinsic non-linear property of the hemodynamic response or of the summation of the underlying neuronal activity itself [21]. However, a large contribution comes from converting the CBF response into BOLD signal changes, because when a shorter stimulus is narrower than the CBF response width, it is introduced a non-linear response [26]. Therefore, a hypothesis suggests that, although the basic coupling between net neuronal activity and hemodynamic response is roughly linear, the relationship between neuronal response and stimulus/task parameters is often non-linear. If linearity prevails, separate sensory and higher-level cognitive events can be rapidly and consecutively generated, and their response separated and analyzed [44].

2.3.2 Variability sources of the Hemodynamic Response Function

The timing, magnitude and shape of the HRF present noticeable variability [45, 46, 44] in parameters such as time-to-peak, widths, delays, and/or post-undershoot shapes [36]. This variability can be structured into three main categories, which cause the most significant variations: intra-subject, intra-group inter-subject, and inter-group variability. Intra-subject variability regards the HRF differences found across distinct brain regions of interest (ROIs) in the same individual; on the other hand, intra-group inter-subject variability concerns the HRF differences found across different individuals from the same group, in a certain brain region; at last, inter-group variability relates to the HRF differences found between different groups for a given brain region [35]. However, HRF variabilities across voxels, experimental tasks (either sensory, motor and/or cognitive), time (hours or days), and/or scans can also be found, even though they cause smaller differences [45, 46, 36, 30].

The HRF variabilities hinder an accurate quantification of an individual's BOLD signal using a canonical HRF [44] since the covariates produced when a standard model is used will

not be perfectly valid. Hence, a large variation of this error and of its degree between experimental designs can expected, potentially resulting in an inability to fully model experimentally introduced variance [34]. As a consequence, statistical methods which identify signal change regions will have to consider the hemodynamic response timing and/or shape variance to be sensitive to all sorts of signal change [44].

HRF variability depends on several neural and non-neural factors, which will affect the HRF even with consistent changes in neural activity and possibly lead to misclassifications, for instance, in brain connectivities [35, 36]. Some of them include diseases, age, blood vessel structure, hematocrit concentration, vasculature density and diameter within each voxel [36], lipid, alcohol or caffeine ingestion [35], inhaled CO_2 and O_2 concentration changes, intravenous saline administration [36], neural activity timing, and neurovascular coupling differences [45, 46], which include, for instance, baseline CBF [47]. Other encompass slice timing, global magnetic susceptibilities, venal partial volume imaging [35], thermal noise, breathing and heart rate changes, hardware instabilities, cognitive state changes, and task approach strategy [36].

2.4 Neurovascular Coupling

Despite being a highly metabolic organ [48], consuming about 20% of the body's total energy when at rest [49], the brain has a limited intracellular energy storage capacity [50], making it harder to obtain when it is needed. Therefore, this organ requires relatively constant blood flow in order to regulate the numerous local and dynamic supplies and demands imposed by its activity [51, 52], at rates close to those of the metabolic and neuronal processes [53]. In order for such regulation not to be compromised [50], blood circulation needs to reach the brain at the exact place in the right timing and amount, because if, for instance, there is an inadequate flow supply for a given brain region, as a consequence, the carried glucose and oxygen might not correspond to its energetic demands [52]. As a result, brain changes can appear [54], which can potentially damage neurons and/or the glia, eventually leading to their death [49] and, consequently, to brain damage [54].

Therefore, to guarantee that the blood flow ensures the metabolic demands of a specific brain region [48, 50], thus maintaining cerebral homeostasis [55, 49, 56], not only the brain is highly vascularized [48], but it also has developed Neurovascular Coupling (NVC) [49]. These biophysical properties of the neural systems [57] reflect the close temporal and spatial link between neuronal activity and CBF [50], allowing to change the vascular tone to sophisticatedly regulate local cerebral perfusion according to the brain activity by diverse cell signaling pathways [51]. NVC is performed in the cortex and in deep brain structures, regardless of any structural and functional differences depending on its location [51, 45, 52].

So that the NVC can take place, it is required to have an essential structure, the Neurovascular Unit (NVU) [51], whose concept has been developed in recent years [52]. The NVU, as depicted in figure 2.2, represents the interface between neuronal, vascular and glial structures [51], comprising vascular (endothelial cells, smooth muscle cells (SMCs), and pericytes), neuronal

(neurons, interneurons, pyramidal cells) and glial cells (astrocytes, microglia, oligodendrocytes) [51, 48, 50]. These components are differently distributed across multiple cerebrovascular network levels [48] and intercommunicate with each other in order to produce a brain function as efficient as possible [55], highlighting the symbiosis as well as the developmental, structural and functional interdependence between each one of them, both in health and in disease [52].

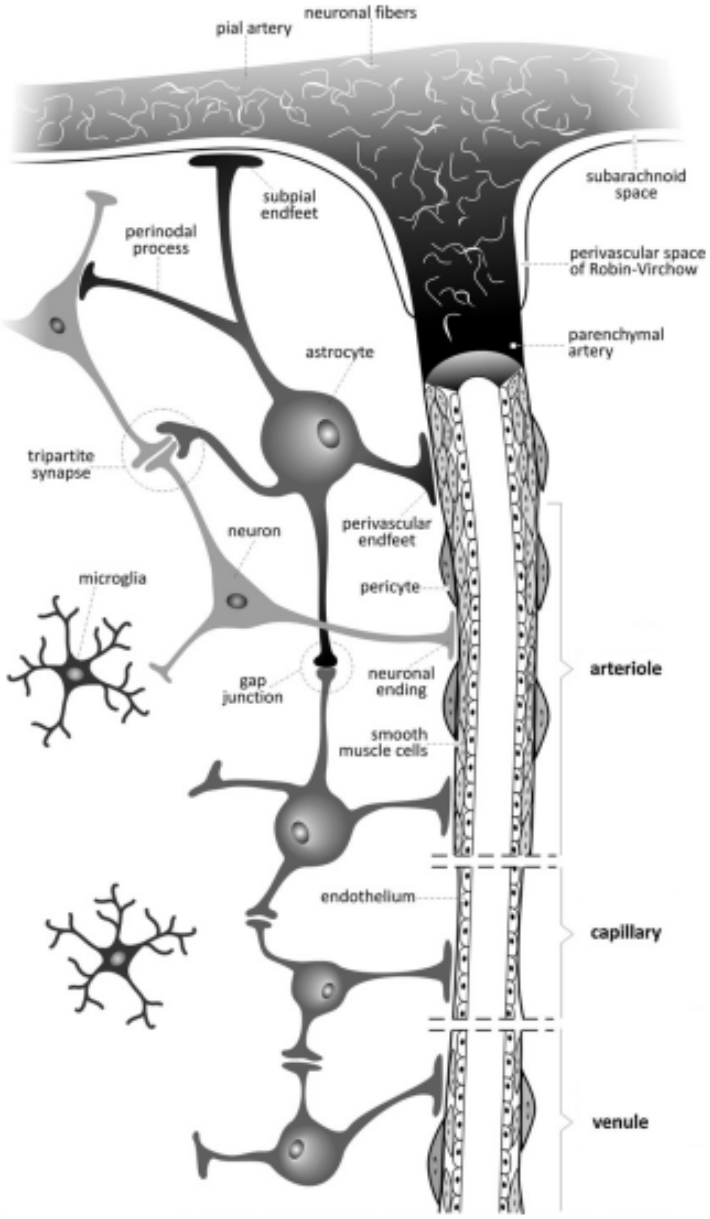

Figure 2.2: Representation of the morphological structure of the NVU. Retrieved from Kowiański et al. (2013) [58].

Although there is some mechanistic knowledge about this process, the current understanding of the NVC in humans is limited and incomplete due to the use of inappropriate and consistent analysis strategies and stimulation paradigms [51].

2.4.1 Neurovascular Coupling Mechanisms

There is no single mechanism accountable for NVC [59], so, in order to better understand the overall neural function, pathology-related, or even age-related changes, it becomes crucial to distinguish the multiple mechanisms underlying this phenomenon. As mentioned, although the knowledge associated with it still remains limited and incomplete, progress has been made to better enlighten how each component of the neurovascular unit interacts and intercommunicates with each other, and what consequences it entails [53]. Next, I will briefly discuss some regulating mechanisms of the NVC, in the different segments that comprise it.

2.4.1.1 Neuronal cells

Currently, it is considered that metabolism-dependent (feedback) and independent (feed-forward) blood flow regulation mechanisms can coexist in the neurons [52, 49]. As for the former, they assume that an increase in tissue metabolic and clearance demands deriving from neural activity leads to a rise in blood flow distribution [52]. In the latter, which make up the majority of the existing processes, neurotransmitters are produced, which, directly or indirectly (for instance, via astrocytes), act on blood vessels, creating the vascular response [52, 49]. The engagement degree of each of these mechanisms in the mentioned regulation will depend on the timing, intensity, and duration of the activation, as well as the brain's regions and state of development [52]. Next, the mechanisms which regulate the CBF via CO_2, adenosine triphosphate (ATP) (adenosine), glutamate, and O_2 in neurons will be elucidated.

In order to enable CO_2 clearance at high intracellular levels, this gas is diffused through the neuronal membrane, reaching the extracellular space. Consequently, in this milieu, the potential of hydrogen (pH) increases, causing an efflux of potassium ions (K^+) into the extracellular space by voltage-gated K^+ channels. As a result, endothelial cells undergo a hyperpolarization and relax, subsequently causing vasodilation [60]. On the other hand, increased ATP concentration, and thus, adenosine levels, promotes its binding to purinergic receptors in SMCs and endothelial cells, easing vasodilation [53].

As for glutamate, it is released by presynaptic neurons during synapses, activating α-amino-3-hydroxy-5-methyl-4-isoxazole epropionic acid (AMPA) and N-methyl-D-aspartate (NMDA) post-synaptic neuronal receptors. Subsequently, the calcium ion (Ca^{2+}) gets into the post-synaptic neurons, and its intracellular concentration increases. As a result, as illustrated in figure 2.3, two vasodilators are produced, prostaglandins - arising from araquidonic acid (AA) - and NO [52].

However, the blood O_2 concentration, does not have a linear influence as the above-mentioned molecules. A O_2 concentration decrease causes a Ca^{2+} release in the astrocytes, and if the concentration of this cation becomes higher than the existing under physiological conditions, vasoconstriction happens. Otherwise, vasodilation takes place. This effect is due to a blood modulation mechanism between O_2 and NO [49].

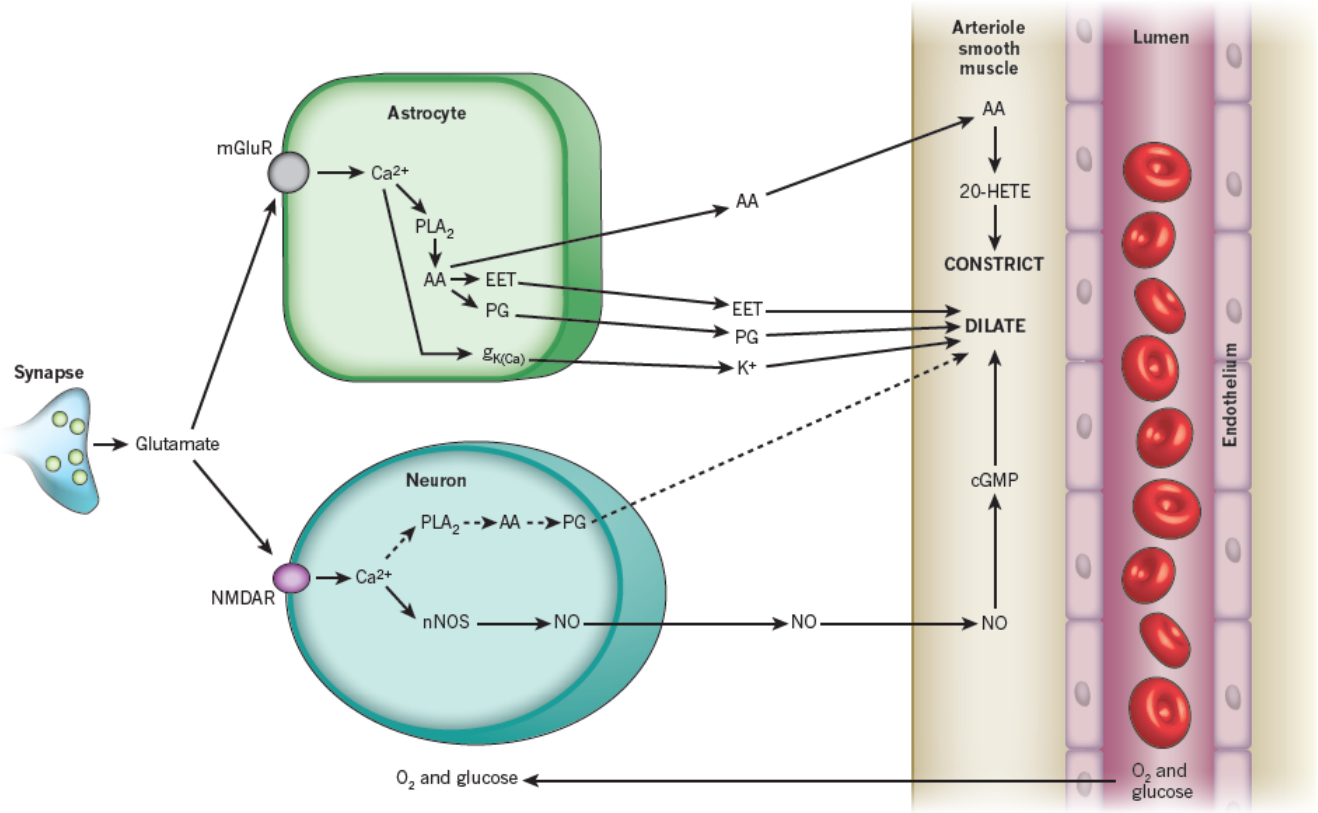

Figure 2.3: Representation of the glutamate CBF regulation pathways. Retrieved from Attwell et al. (2010) [49].

2.4.1.2 Glial cells

The role of glial cells in the NVC is way less understood than that performed by the neuronal and vascular components of the NVU. However, there is increasing evidence that these cells [61], by conferring the greatest bridge between neurons and blood vessels, own a privileged position mediating the NVC, representing important intermediate roles in complex processes [53]. Next, I will explain the glutamate regulation mechanism in astrocytes and the neuron-astrocyte lactate shuttle.

As in neurons, during neuronal activation, astrocytes also respond to the glutamate release at synapses, capturing it through metabotropic glutamate receptors (mGluRs), in order to regulate CBF by directly and indirectly transmitting vasomodulatory signals to the SMCs [50, 49]. However, these are not only vasodilators since there are also vasoconstrictors. With the astrocytic glutamate uptake, the Ca^{2+} concentration increases [53, 49], stimulating, in this cell, the activation of two different pathways, as illustrated in figure 2.3: one based on the K^+ ion and other based on AA metabolites. In the former, the Ca^{2+} increase triggers the opening of large-conductance calcium ion (Ca^{2+})-activated K^+ (BK) channels in the astrocytic terminations, releasing K^+ into the SMCs, thus causing vasodilation. In the latter, the Ca^{2+} increase produces AA. From this molecule, it can be generated one of two vasodilators or a vasoconstrictor: prostaglandin, epoxyeicosatrienoic acid (EET), or 20-hydroxyeicosatetraenoic

acid (20-HETE), respectively [49]. The obtained outcome (vasodilation or vasoconstriction) will vary according to the frequency, kinetics, and spatial propagation of the released vasomodeling substances, which depend on the total Ca^{2+} concentration in the processes and somatic body of the astrocytes [51], and on the interaction with other factors such as O_2 concentration [52, 49], pre-existing vessel tone [52, 49] or other cellular messengers [51, 52].

The astrocyte-neuron lactate shuttle, in turn, is a mechanism originated in astrocytes, in which the direct metabolic support of neurons is carried out. Glucose in the blood vessels is absorbed through its astrocytic membrane receptors and is then converted into pyruvate via glycolysis. As pyruvate is prevented from undergoing oxidative metabolism in astrocytes, it is converted into lactate, and then transported to neuronal axons. Once it arrives in the axon, lactate is converted to pyruvate and enters the Krebs cycle, where it is converted to water and ATP in order to restore the membrane's resting potential so that the neuron may fire again [53].

2.4.1.3 Vascular cells

At the vascular level, the NVC reflects a coordinated action of several mediators from different cells [48, 49] that operate at different cerebrovascular network levels by specific mechanisms for each segment in order to regulate the CBF [52]. Then, I will explain a retrograde vasodilation mechanism, which is illustrated in figure 2.4.

Due to synaptic activity, the O_2 concentration decreases, and extracellular K^+ is released. In turn, this cation stimulates the potassium inward-rectifier (K_{ir}) channels found in capillary endothelial cells and pericytes, hyperpolarizing the former. This hyperpolarization propagates backward in these two types of cells through gap junctions between pericytes and endothelial cells, and between adjacent endothelial cells, reaching the intraparenchymal arterioles [52, 49]. At the same time, the decrease in O_2 concentration increases the deformability of red blood cells, reducing blood viscosity, which increases capillary flow regardless of its diameter [52].

As the endothelial hyperpolarization from the capillaries reaches the intraparenchymal arterioles, the endothelium of these vessels is put through shear stress. Consequently, endothelial vasodilating factors are released, and it takes place the retrograde transfer of SMC hyperpolarization by myoendothelial junctions and gap junctions between SMCs and between endothelial cells. In addition, the vasoactive factors previously released by active neurons and astrocytes during neuronal activity are also delivered, and due to the decreased intravascular pressure and increased flow speed caused by downstream vasodilation, the local myogenic response arises. As a result, the SMCs relax, thus contributing to the preservation of vasodilation and subsequent retrograde propagation towards the pial arterioles. In the latter, which are remote from the activation site, vasodilation can come from two sources: the hyperpolarization from downstream arterioles and the local myogenic response [52].

The potential that each cerebrovascular segment will physically and pathologically own in CBF regulation [52] by controlling the capillary diameter via pericytes will depend on the hemodynamic resistance fraction of the vascular network to which the capillaries contribute [49]. Therefore, inside the brain, pial arterioles are the vessels which regulate the less CBF. In the

opposite direction, the capillaries, penetrating arterioles, and venules are the ones which control it the most [52].

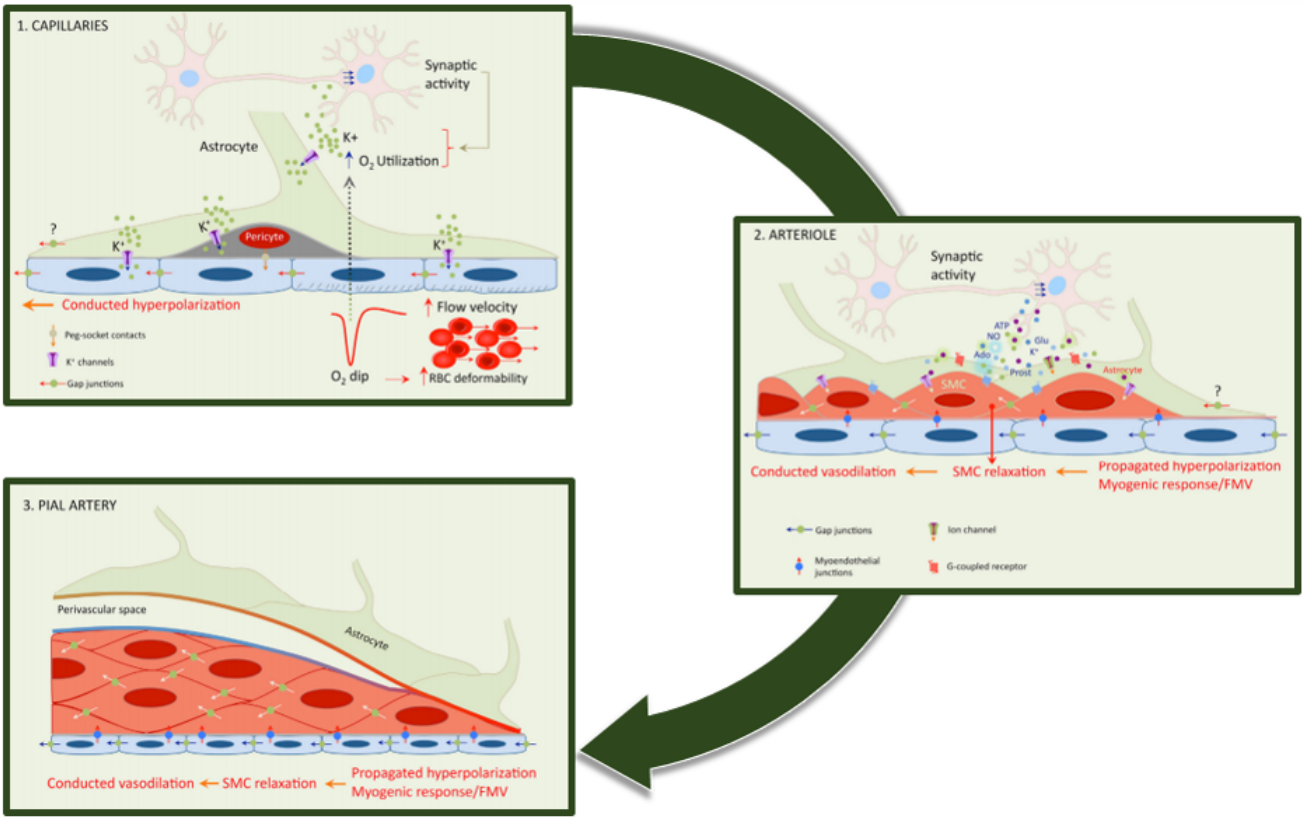

Figure 2.4: Representation of an NVC mechanism at the vascular level: retrograde vasodilation. Adapted from Iadecola et al. (2017) [52].

2.4.2 Neurovascular Coupling and the Hemodynamic Response Function

The BOLD response, as well as its properties, reflect the joint action of vasoactive molecules released by neuronal activity-triggered mechanisms [52, 49], and NVU's cells (neurons, interneurons, astrocytes, endothelial cells, and pericytes) [52]. This is due to the fact that the interaction between the two counterparts, known as NVC, allows the vasodilation and the vasoconstriction of local blood vessels, directly and indirectly modulating CBF, and consequently, blood oxygenation, in order to provide the required energy resources that best fit the metabolic demands of the neurons [53]. The components of the NVC will vary from region to region, and from condition to condition, governing how the coupling takes place [59], and consequently, the temporal properties of the hemodynamic response which are correlated with each element [51, 52].

Notwithstanding, the physiological mechanisms underlying this coupling, which is related to CBF and CBV variations, remain to be fully understood [62], complicating the comprehension of the relationship between the BOLD signal, CBF and $CMRO_2$, as well as the interpretation of the HRF [63]. Consequently, the HRF's own modulation has been hampered [63] since the multiple models developed, which attempt to elucidate it, have so far been only partially successful,

as they have failed to explain the whole mechanism underlying the BOLD response. Thus, it becomes difficult to determine which is the best dynamic model that captures a specific NVC mechanism, with the choice depending on the implemented experimental paradigm, the nature and resolution of measured data, and/or the context and goal of the study [64].

3

State of Art

3.1 Functional Magnetic Resonance Imaging Paradigms

fMRI allows to observe the modulation of the BOLD effect in the brain based on neuronal activation. In order to induce it, it becomes crucial to develop paradigms - temporal organization structures of fMRI data acquisition, during which an individual performs (or not) a series of cognitive tasks at certain timepoints of interest [65]. Cognitive tasks can be explicit or implicit, corresponding to task-based or resting-state paradigms, respectively [22]. Most approaches employ the resting-state paradigm due to its straightforward implementation. However, in this project, task paradigms were used, so, next, I will address the three types of task-based paradigms currently most used: block, event-related, and mixed paradigms [42], and its characteristics.

3.1.1 Block Paradigms

The first dynamic fMRI experiments implemented pioneering functional imaging methods that were based on hemodynamics, which enabled to map brain activity patterns based on brain hemodynamic changes. However, the experimental paradigms initially employed were task-based paradigms derived from designs related to the aforementioned techniques [21] - block paradigms - in which only prolonged-state brain activity volumes were obtained [66].

Block designs have their greatest use in trial averaging, in order to achieve considerable SNR ratios while producing functional activation volumes [67]. Therefore, block designs are suitable in locating functional areas and studying steady-state processes, such as attention [68]. In these designs, different condition periods alternate with each other [42], that is, consecutive stimuli associated with a given condition are presented during an extended period (block) to maintain cognitive engagement, followed by blocks concerning other condition or the rest/baseline [22, 69] - as exemplified in figure 3.1. The most frequently used block paradigm encompasses a period during which a task is performed, followed by a rest period of the same length [42].

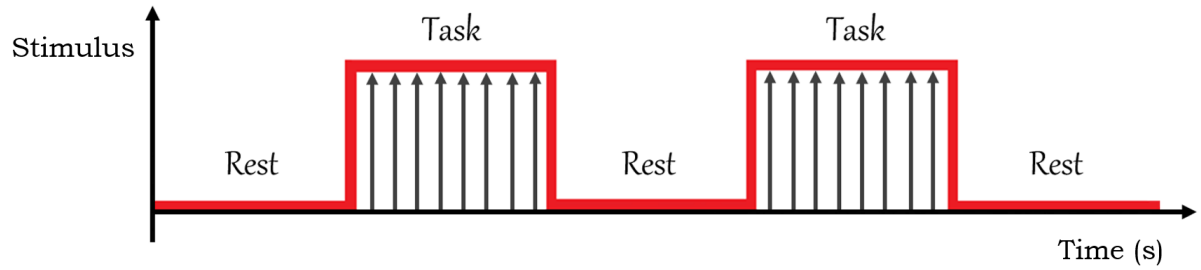

Figure 3.1: Example of a block fMRI paradigm.

This design has a simpler implementation [42], not demanding to randomize and space various sorts of stimuli [70], and a more direct analysis, not depending on an accurate HRF model [71]. As this paradigm presents trials in sequential blocks, data acquisition periods usually are extended, and thus, several images can be acquired during the block [72]. As a result, time efficiency becomes maximum and the design more robust concerning time uncertainty [69]. Besides, the statistical power, as well as the SNR, become higher [42], given that the statistical quality of individual images is relatively poor regarding changes in the signal of interest [72]. However, the order and length of the conditions can be anticipated [71], which introduces confounding variables. Furthermore, as blocks are relatively long (between 10 to 20 seconds) [42], not only the estimation power is weak [68], that is, it is difficult to accurately define the time-courses of the response to individual trials [22, 73], and consequently, distinguish their separation within the blocks [71], but also the participant can quickly get acquainted with the task [22], making it difficult to obtain information regarding the HRF and the timing of the fMRI signal [42].

The block design can be alternating or controlled. In the first case, different conditions are interchanged in different blocks, to determine which voxels display differential activity as a function of the variables. In the latter, different conditions are separated by null blocks, that is, by a control condition, allowing each block to identify which voxels were activated by each condition, separately and in both conditions [68].

3.1.2 Event-related Paradigms

When experiments which aimed to explore the signal responses to very short stimuli were carried out, it was found that within seconds after their onset, robust hemodynamic changes could be detected [37]. Consequently, the block design, although useful to investigate blood flow fluctuations that require a physiological quasi-equilibrium state during periods longer than 1 minute, it became unsuitable for the previously mentioned experimental protocols. As a result, the scientific community gradually began to drift from block designs [21], and it has developed a new class of experimental paradigms in order to detect and characterize the transient and regional alterations of the HRF [66] in response to brief stimuli or tasks [71], as well as to measure and to monitor its temporal evolution [37] - the event-related/trial-based paradigm. One topic that often applies this paradigm in its experimental procedure is decision making

studies, in which two options are presented in each event, and the participant has to choose one of them by pressing a button [74].

In this design, stimuli are presented for short periods, termed events, whose duration randomly varies between 0.5 to 8 seconds [22], at discrete time points [74] (see figure 3.2). The events are temporally separated by inter-stimulus intervals (ISIs), whose temporal range scopes between 0.5 to 20 seconds [22]. Moreover, the events can be randomly ordered, that is, the response to an event may not be mistaken by a subject's cognitive set nor consistently affected by previous events [66].

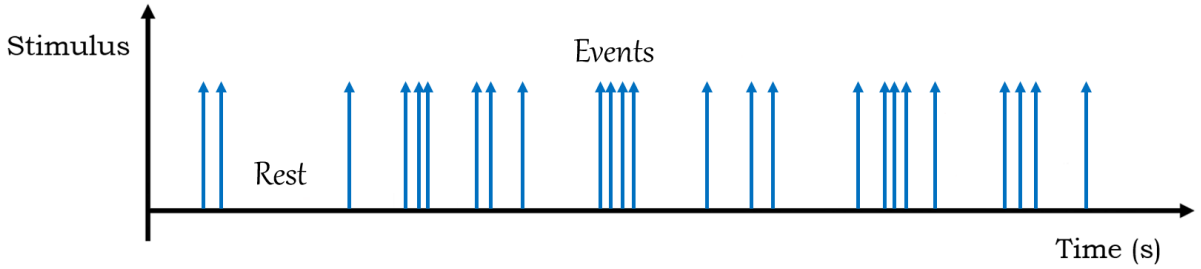

Figure 3.2: Example of a event-related fMRI paradigm.

This paradigm can be distinguished in slow or fast event-related designs, according to the ranges of the ISIs [22]. Slow event-related designs own ISIs slightly longer than the HRF, producing well-spaced events, and, consequently, preventing the overlapping of successive HRF stimuli. In fast event-related designs, the ISIs are shorter than the HRF, so the time spacing between events is shorter, potentially overlapping the HRF [22]. Additionally, event-related paradigms can also be classified into periodic or jittered, according to the type of ISIs they own: constant or random, correspondingly [69].

The event-related design contains high temporal resolution, and the random order of events is unpredictable [42], reducing the participant's boredom, anticipation, and habituation to the task, which in turn increases its flexibility in experiments [68]. Considering these advantages, the estimation power of the HRF's time course increases [75], allowing an independent analysis of cognitive processes, and consequently, its associated brain responses, linked to each event [74]. In contrast, as in this paradigm imaging times are shorter and there are few events per subject [22], data analysis becomes more complex and dependent on a more accurate HRF model [73] and SNR decreases, which consequently decreases both statistical power and efficiency [22]. This situation tries to be offset by extending the experiment time [71].

There are several approaches to optimize event-related designs in order to maximize its power to detect and estimate changes in the BOLD signal [74]. One way to overcome some of the aforementioned weaknesses is to use rapid event-related designs. They enable higher frequency stimulation, resulting in an increased statistical power [65]. However, random ISIs (stochastic design) - which minimize the habituation and expectation effects - must be implemented in order to produce a differential overlap of the HRF, reducing multicollinearity problems and better

characterizing each response condition [22, 75]. There are also alternative methods compatible with this type of paradigms, such as m-sequences and genetic algorithms, which allow flexible compromises between estimation efficiency and detection power to be reached [22].

3.1.3 Mixed Paradigms

The neuroimaging field has been in constant development [76]. Even though the advent of event-related designs did not solve problems regarding the block designs itself [74], it enabled event-based experiments [66], which allowed to increase the complexity of experiments and experimental paradigms, as well as to model more dynamic analysis methods. As a result, the research's scope has been extended, allowing to explore several topics that have never been considered before, such as brain connectivity or causality [74]. One of these directions included the investigation of interactions between existing processes at different time scales [68], seeking, in particular, the differences between distinct classes of cognitive functions [76], which had lead to a new variety of task paradigms, the mixed design. In this paradigm, block tasks take place simultaneously with semi-random events, with the latter possessing resting periods between them [42], resulting in a combination of the measurement of repetitive sets of stimuli regarding the block design with the transient responses detected by event-related designs [65] (see figure 3.3). The mentioned paradigm assumes that the activity concerning the block tasks must remain constant during them, even during intervals between events. On the other hand, the activity regarding the events must decrease during those same intervals. Therefore, this paradigm enables to separate both transient and continuous HRF segments, and consequently, to acquire information related to each one of them as the task is performed [65].

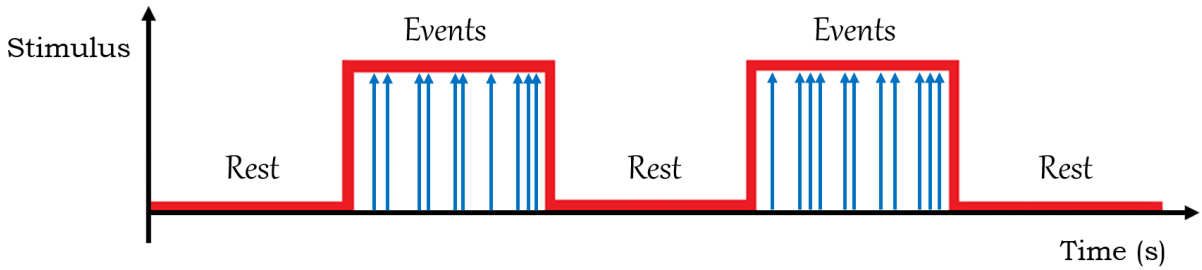

Figure 3.3: Example of a mixed fMRI paradigm.

This paradigm's features allowed to test a greater variety of psychological theories, and a more flexible interpretation of the functional behavior of the brain areas activated during a cognitive task, discerning them according to the functional role that each one owns, by separating them based on the time-courses of their activity, and not just by identifying which area is activated [76]. On the other hand, this paradigm presumes more assumptions than others and contains problems related to poor HRF estimates, since non-hemodynamic responses may be interpreted as transient neuronal responses and it is impossible to model the latter on GLM with presumed HRF shapes [65, 77, 78]. Furthermore, the ability to extract continuous activity relies on the consistent induction of the psychological state. Therefore, if the experimental

design fails to induce a consistent cognitive state, the neuronal correlations of that state cannot be extracted or interpreted [77]. Finally, since the statistical power of the continuous signal is weaker, this paradigm requires more subjects in order to measure continuous and statistically significant effects [78].

3.1.4 Future Directions

In the near future, as event-related designs have become strongly intertwined with fMRI, it is clear that this concept itself will represent a standard. That is, since it is so significant for the fMRI, instead of being a paradigm class itself, it will become the base paradigm used in fMRI studies, from which all the remaining, both the existing and the forthcoming ones, will be derived. In contrast, it may not happen the same with the block design, a special experimental paradigm that will remain relevant in experiments where maximum detection power is required [74].

It should also be noted that some technical developments in neuroimaging did not inevitably benefit the current design of the experiments [79]. For instance, with the increasing complexity of experimental designs, fMRI analyzes have become increasingly distant from the original data, which, on the one hand, allows a greater use of model-based fMRI, but, on the other hand, less often articles plot the activation time [74]. Thus, interest in more sophisticated analysis - such as Multi-Voxel Pattern Analysis (MVPA) or Dynamic Causal Modelling (DCM) - and search methods - such as the genetic algorithm - has increased. However, so that these approaches can be more widely used, it is required not only to have a robust and easy-to-use software implementation, but also to create designs that optimize the estimates obtained with these methods. It is thought that this will be the course to follow in order to develop a new class of optimal fMRI designs [79].

3.2 The HRF and its use as biomarker

The HRF has a complex interpretation as it reflects a fine-tuned interaction between the cellular structures that comprise the NVC. That is, any functional alterations may come from changes in vascular, neuronal, and/or glial components [55, 80], and not just from direct changes in neuronal activity and tasks [81]. For instance, consistent neuronal activity-independent age-related changes in vascular reactivity, blood flow, and tortuosity can generate age-related differences in the HRF [55, 82, 29]. Moreover, Turner et al. (2019) found that changes in glial cell intermediates were associated with NVC deficits and, consequently, decreases in neuronal processing function and speed [80]. In addition, several studies have shown that the NVC is affected by several pathologies, thus altering the HRF. For example, Roc et al. (2006) noticed in anterior circulation high-grade stenosis patients that, although the CBF value remained at the baseline, the blood flow responses which counterbalanced the metabolic demands were compromised. Thus, a more prolonged hemodynamic response was perceived, in which there was a larger response or an anticipated BOLD dip, followed by a delayed hyperemic response [83]. Since alterations in the HRF may reflect changes in the NVC and, consequently, pathophysiolog-

ical brain changes even at early stages, in specific brain regions, in order to assess neurovascular function in certain diseases, the use of the HRF as a imaging functional biomarker has been widely investigated [45], by comparing conditions, studies and populations of patients through the analysis of the relative changes of the HRF [84], enabling to monitor the recovery of individuals, either naturally or by medical intervention [45].

3.2.1 Hemodynamic Response Function Parameters: A Biomarker?

One way to use the HRF to collect information regarding neuronal or vascular pathologies [45] arising from alterations in the NVC - consequently causing changes at the metabolic level and in physiological parameters (such as synaptic activity and/or blood flow) [81] - is to distinguish the differences between HRF parameters such as peak amplitude or peak latency in different subjects and/or regions [45, 81]. To estimate and characterize these parameters, it becomes necessary to extract the shape of the HRF in different types of cognitive events [85]. Nevertheless, the interpretation of the parameters becomes complex. Firstly, they do not always maintain an unequivocal relationship with the underlying neuronal/glial activity changes [81], since they may highly correlate with extracellular postsynaptic activity measures [86], as well as with glial components. Secondly, spatial bias befalls, that is, the different brain regions exhibit biologically derived differences which do not relate to the overlying neuronal function. Finally, biophysical factors such as alterations in the NVC per brain regions can produce different changes in multiple features of the HRF parameters [85]. In other words, there is a cross-talk potential between the estimated parameters, in which one owns a biased value due to unrelated changes in another parameter [85].

Of the multiple studies carried out to date, in which the HRF has been used as a biomarker for certain pathologies by analyzing its parameters [87], most have focused on the assessment of the HRF magnitude, which is given by its peak. However, an interest in the evaluation of other parameters - such as the activation duration, and the time lag to the maximum activation amplitude, given respectively by full width at half maximum (FWHM) and peak latency - has increased [85, 84]. Peck et al. (2004), based on the analysis of the peak latency, suggested that the BOLD signal could be used as a biomarker to monitor and, consequently, improve the aphasia recovery [87]. By analyzing that same parameter, Bonakdarpour et al. (2007) inferred that the delay witnessed in stroke patients would not be explained by processing delays [88], but by an extended CBF delivery time from upstream pial vasculature, which induces local neuronal activity, suggesting that the pathology and its nature can modify the temporal behavior of the NVC (and thus, the HRF), and that in a population of patients, the protocol can discriminate these changes [45].

3.2.2 Type 2 Diabetes *Mellitus* and the Hemodynamic Response Function

The hyperglycemia condition inherent to T2DM causes an uncontrolled increase in the cellular respiration rate [89] which, after a certain point, causes an imbalance between reactive oxygen species (ROS) and antioxidants [53], thus promoting stress oxidative [90], which causes damage and dysfunction to any of the three components of NVU [53].

In neurons, oxidative stress causes mitochondrial dysfunction [90], disrupting Ca^{2+} regulation, which in turn increases its intracellular concentration, as well as that of ROS. Hence, the membrane potential increases and the neuronal excitability and metabolism change [53], possibly inhibiting neurovasodilatory signaling pathways dependent on that ion [53, 49], as well as generating axial regression and demyelination, which cause reactive astrogliosis [53]. Another outcome due to the oxidative stress in these cells is the insulin signaling decline and the subsequent decrease in the cellular response to insulin [89]. Consequently, the acetylcholine, serotonin, and dopamine levels decrease, the norepinephrine concentration increases, and the modulations of the expression of NMDA receptors and brain glucose metabolism become unfeasible, damaging neurons [89]. In addition, together with glial dysfunction, neural dysfunction hinders the mechanisms that deliver oxygen to neurons in a fast and regulated manner [53], promoting cellular anaerobic activity [89]. Finally, the cumulative effect of the oxidative stress and the subsequent cerebral autoregulation loss [48] prompt neuroinflammation and consequent neurodegeneration, culminating in the neuronal brain apoptosis (neuronal death) [89].

In astrocytes, this condition increases oxidative astrocytic metabolism, which amplifies the mitochondrial ROS production and modifies the astrocyte-neuron lactate shuttle, and hence, pyruvate is metabolized by the astrocytes, instead of being shuttled to the neurons as lactate. As a result, more oxidative stress and cell damage are produced. As an example, the microglia becomes toxic to the neurons, and the astrocytic glucose and glutamate uptakes, which take place at the perivascular astrocytic terminations and synapses, respectively, become compromised. Regarding the reactive astrogliosis, earlier mentioned as another consequence of the oxidative stress, it causes astrocytic hypertrophy and proliferation, increased astrocytic NO production, and overlapping of different astrocytic domains. The latter impairs Ca^{2+} signaling between nearby astrocyte endfeet, which is even further deteriorated by damaging Ca^{2+} sequestration in the endoplasmic reticulum [53].

The endothelial cells, due to the oxidative stress, become unable to down-regulate the expression of glucose transporters [91]. Therefore, as it happens in the two other units of the NVU, ROS are also produced in the mitochondria, causing inflammation and endothelial damage. As a result, vasodilatory functions of the endothelium become compromised [53], decreasing the bioavailability of NO and prostacyclins (vasodilators) within the vasculature [91, 92], affecting K^+ channels (responsible for the endothelial retrograde vasodilation) [52, 92] and increasing the levels of vasoconstrictors [53]. Due to the oxidative stress, pericytes are also lost [89], and tight junctions are degraded [53]. By changing the endothelial signal transduction and redox-regulated transcription factors, vascular endothelial permeability increases, promoting blood vessel leakages [53], leukocyte adhesion, and abnormal proliferation of endothelial cells [91], which precludes the autoregulatory efficiency of brain vessels [92]. As an example, the blood–brain barrier (BBB) is disrupted due to the oxidative stress, releasing toxic compounds, and causing even more damage to nerve structures [89]. On the other hand, endothelial dysfunction caused by hyperglycemia produces several vascular morphological changes. For instance, the lumen diameter reduces, and the cross-sectional areas, branching density [48] and stiffness of the vessels [61], tortuosity of the pial arteries, and the thickness of capillary walls increase [48], compromis-

ing the vessels' ability to dilate and constrict in response to blood pressure (myogenic response) or to changes in vasoactive substances [53, 61]. Consequently, blood perfusion decreases [91].

Furthermore, although no consensus has yet been reached, it is believed that T2DM induces a decrease in CBF [92], increasing neuronal activity but decreasing oxygen availability and neural efficiency [53]. It is therefore based on the aforementioned damages that T2DM promotes neurovascular decoupling, even in apparently normal intact brains [12], impairing the regulatory mechanisms that ensure the match between perfusion and neuronal demands, contributing to the macro and microvascular disorders later seen in this pathology [92]. Such consequences entail repercussions for the HRF [93], with Duarte et al. (2015) reporting that, in the early stages of T2DM, different physiological response curves were generated, with less overall amplitude, peak, initial dip and undershoot, and that the source of this difference may be possibly driven by the disruption of the NVC [12].

4

Material and Methods

4.1 Experimental Procedure

The experimental procedure employed in this project is succinctly displayed in figure 4.1. In each of the following sections, I will address each of its steps in further detail.

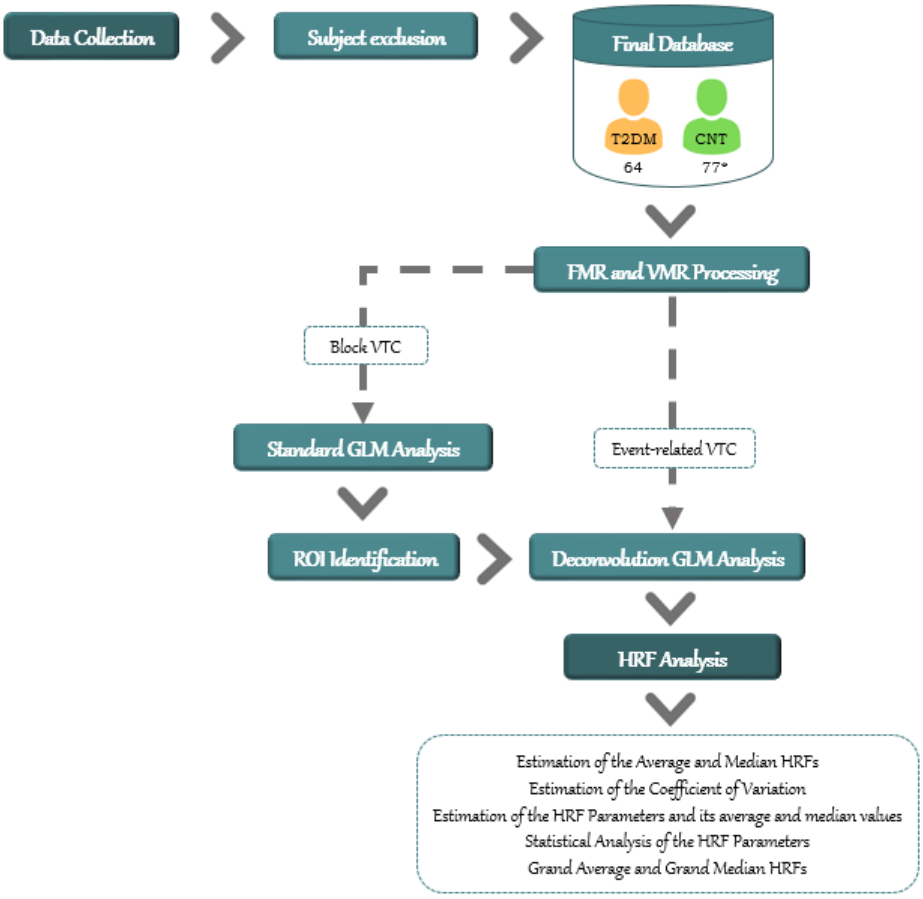

Figure 4.1: Experimental procedure pipeline implemented in this project.

*: Represents the final number of controls, already ruling out the subject excluded during co-registration.

4.1.1 Participants

The first step was the collection of MRI data from each participant at ICNAS. These arose from an existing dataset assembled from previous studies concerned with the topic, which implemented the same experimental protocol, so there was no need to acquire data. This dataset contained 190 subjects, who were separated into two distinct groups: 101 patients with Type 2 Diabetes (T2DM) and 89 healthy controls (CNT). Each subject was associated with its name and ID. These parameters were subsequently hidden by the used software to maintain the anonymity of the individuals.

Of these participants, 48 were excluded due to poor image quality, stemming from artifacts such as motion during the acquisition or even metallic splinters that existed in the head, which could compromise the statistical analysis resulting from their processing. Thus, 142 individuals remained, 75 of whom were male and 67 female. From this sample, there were 64 T2DM individuals (average age = 58,8 ± 8,9 years; age range: 40 - 76 years) and 78 CNT individuals (average age = 51,4 ± 8,7 years; age range: 45 - 72 years). However, a male subject was later removed during co-registration, since it was not possible to overlap the structural volume with the functional data, both when this step was performed through the workflow as well as individually. Below, more descriptive information about the participants can be found.

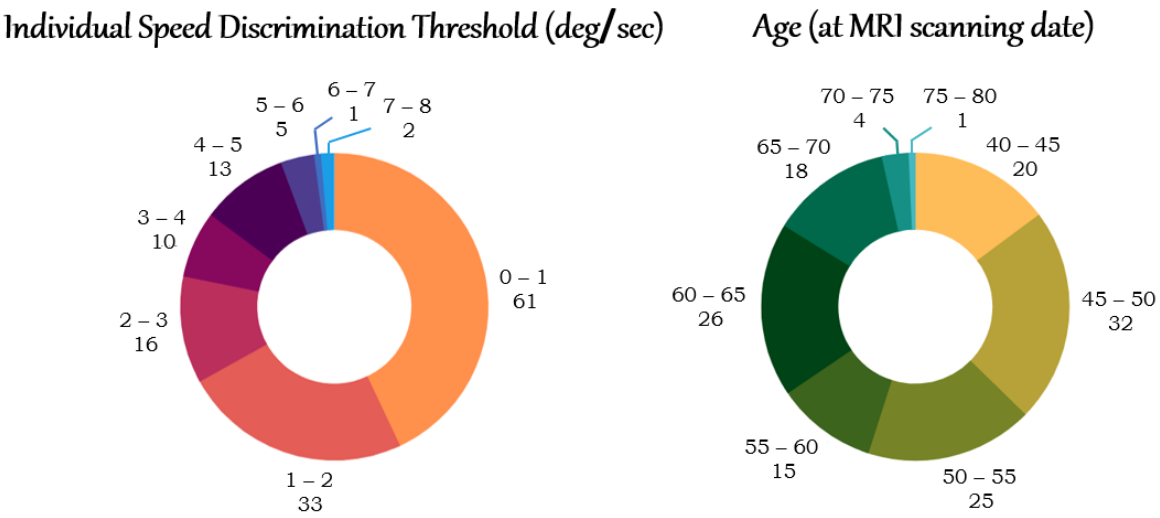

Figure 4.2: Descriptive information regarding the age and individual speed discrimination threshold of the participants.

Table 4.1: Descriptive information regarding the dominant eye and hand of the participants.

Dominant Eye		Dominant Hand	
Left	Right	Left	Right
54	87	3	138

The Helsinki Declaration of 1975 (and as revised in 1983) guidelines were followed throughout the study, and all participants consented to all experimental procedures, which were approved by the Ethics Committee of the Faculty of Medicine of the University of Coimbra.

4.1.2 Imaging Acquisition

Using a 3 T MRI scanner, it was acquired a 3D anatomical Magnetization-Prepared Rapid Gradient Echo (MPRAGE) scan, which applied a T1-Weighted (T1-w) GE pulse sequence, as well as a functional imaging series employing Echo-Planar Imaging (EPI) in block and event-related paradigms. The image characteristics of each acquisition type are shown in table 4.2.

Table 4.2: Descriptive information regarding the image acquisition.

<table>
<tr><th>MPRAGE</th><th colspan="2">EPI</th></tr>
<tr><td>TR = 2530 ms</td><td colspan="2">TR = 2500 ms</td></tr>
<tr><td>TE = 3,42 ms</td><td colspan="2">TE = 30 ms</td></tr>
<tr><td>TI = 1100 ms</td><td colspan="2">Flip angle = 90°</td></tr>
<tr><td>Flip angle = 7°</td><td rowspan="2">2 runs of 145/174 GE scans
(Block design paradigm)</td><td rowspan="2">1 run of 116 GE scans
(Event-related design paradigm)</td></tr>
<tr><td>176 slices</td></tr>
<tr><td>Voxel size = 1 x 1 x 1 mm</td><td colspan="2">Voxel size = 3 x 3 x 3 mm</td></tr>
<tr><td>FOV = 256 mm</td><td colspan="2">FOV = 256 mm</td></tr>
</table>

Key: TR - Repetition Time; TE - Echo Time; TI - Inversion Time; FOV - Field of View

4.1.3 Stimuli and Experimental Design

The methods were as described in Duarte et al. (2015). All individuals underwent a psychophysical task in which the speeds of two white dots (a reference and a target dot) were compared. The dots were randomly presented to them on a gray background, one in each visual hemi-field side by side so that they were asked to select with a button the hemi-field which displayed the fastest dot while fixating a central white cross [12]. Before performing this task, which was measured by the BOLD signal, the stimulus was individually tuned so that there were no significant differences in its performance. In other words, the difficulty level between groups was roughly the same in the selected sample.

Each participant performed three experimental fMRI runs: two block paradigm runs and one event-related paradigm run. All participants were presented with the same randomized sequences, with the stimuli's characteristics only differing in the implemented paradigm type and in its duration in each task, as illustrated in figure 4.3.

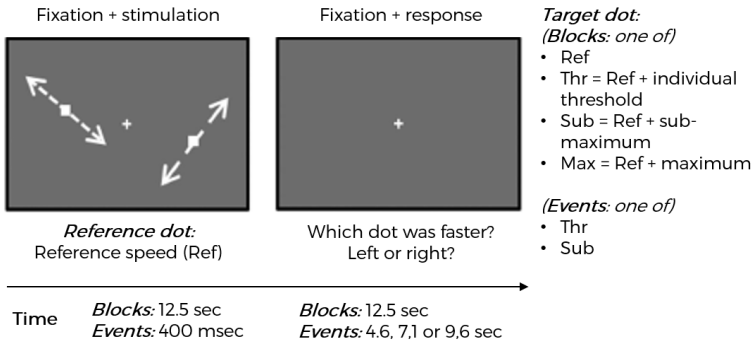

Figure 4.3: Information regarding the stimuli and each experimental protocols (block and event-related paradigms). Adapted from Duarte et al. (2015) [12].

The block paradigm was used in this experimental procedure bearing in mind its high statistical power [42], which increases the ability to locate functional areas activated by task performance [68]. In these paradigm's runs, the reference dot constantly moved at 5°/s, whereas the target dot moved at one of these four different velocities: the reference speed (Reference condition), the reference speed added to the individual discrimination threshold (Threshold condition), the reference speed added to the triple of the individual discrimination threshold (Submaximum condition), and a speed of 20°/s (Maximum condition). The reference condition was exhibited twice, in other words, both visual hemi-fields contained the dot moving with the reference speed, and each of the three remaining conditions was repeated four times with the fastest dot emerging twice in each visual hemi-field. A 12.5-second block was assigned to each condition, during which it was displayed. For all conditions, except the reference condition, the blocks were differentiated according to the visual hemi-field side where the fastest dot (left or right) appeared. Thus, there were 14 blocks of visual stimulation, each interposed by two blocks of baseline fixation, which accounts for a total of 29 blocks, all of them lasting 12.5 seconds. In this paradigm, two different protocols were applied in each of the two runs, according to the version of the stimulation program used (BrainEyeMRI). In the first protocol, which corresponds to the 1.0 and 1.1 versions of the program, each block contained five volumes, whereas, in the second protocol, which corresponds to the 1.2 and 2.0 versions of the program, each block contained six volumes. As a consequence, 145 and 174 volumes were generated, respectively, for the first and second protocols, as illustrated in figure 4.4. From the current sample, 44 and 98 individuals carried out the task according to the first and second protocols, successively.

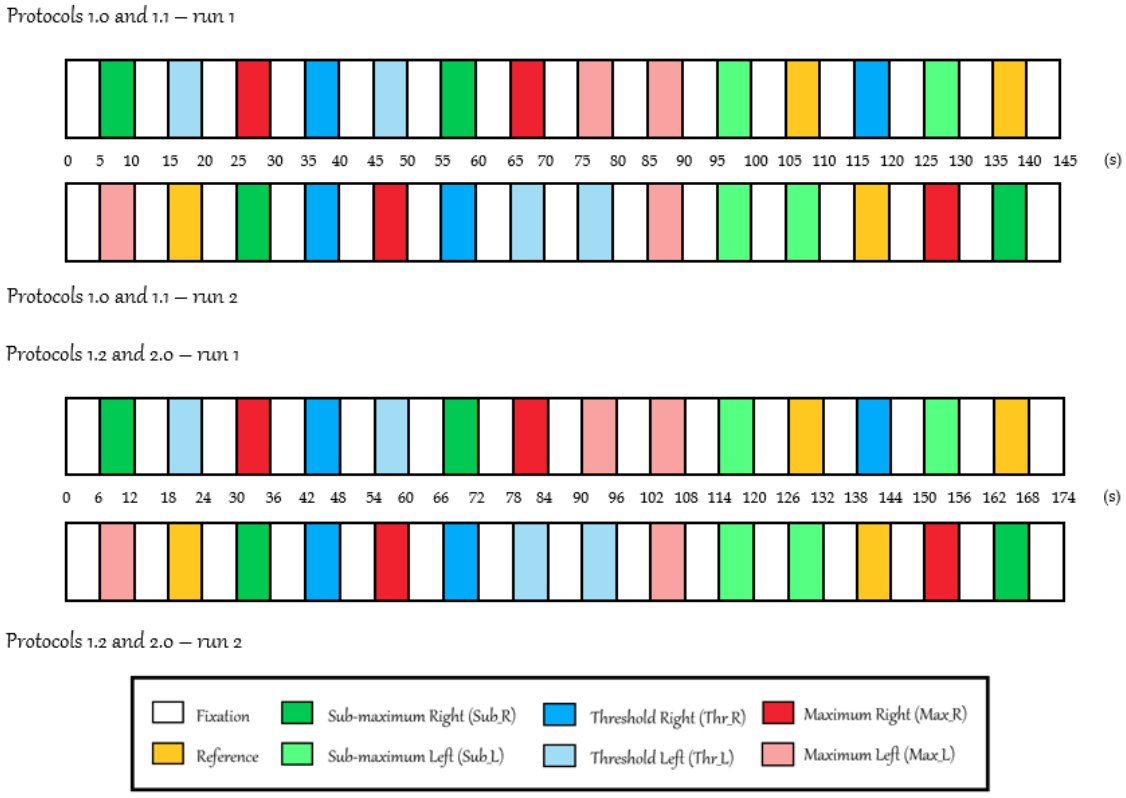

Figure 4.4: Block paradigm protocols implemented in each run.

On the other hand, the event-related paradigm was also implemented in this experimental procedure since the power to estimate responses to brief stimuli is greater [21], which allows to more accurately estimate the HRF [75]. In the runs of this paradigm, the interchange between stimulation and baseline fixation, as well as lateralized conditions, were preserved, yet only the Threshold and Submaximum conditions were presented. Event-related paradigms own way less statistical power than block paradigms [42], therefore requiring more trials per event. Thus, due to efficiency reasons, each of these two conditions, which represent intermediate and representative difficulty levels, was presented 20 times, 10 per hemi-field, as portrayed in figure 4.5. Each visual stimulation period endured 400 milliseconds, whereas each baseline fixation period randomly lasted one of the following values: 4600, 7100, or 9600 milliseconds. In this paradigm, unlike what happens in the block paradigm, only a single protocol was applied to each run, so there was no difference in the number of volumes analyzed.

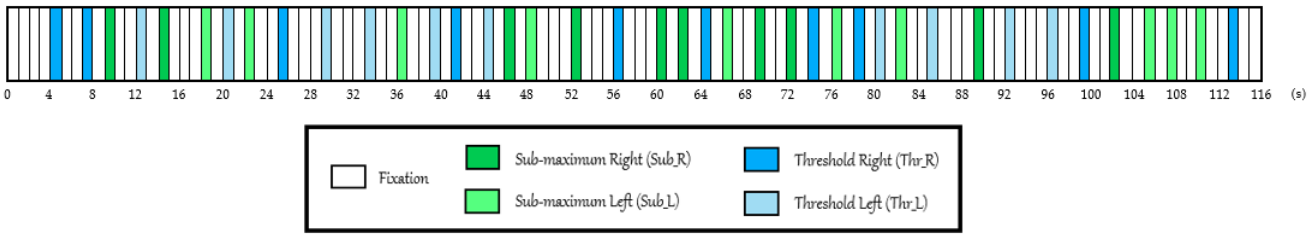

Figure 4.5: Event-related paradigm protocol implemented in a run.

After all experimental procedure runs were processed, a standard GLM analysis was performed in the block paradigm's runs, in which the contrast *stimulation conditions vs. baseline* was applied, thus obtaining a statistical map of the positive/negative signal changes, in order to find regions with overall participation in the task. Then, each region engaged in the block task underwent a deconvolution GLM analysis of the measured signal in the event-related paradigm's runs, in which the HRF of each participant from the study sample was estimated. Finally, in each region, the HRF parameters were deducted to investigate if they were significantly different between T2DM participants and controls.

4.2 Processing

Next, structural and functional data from each individual were processed using Brainvoyager 21.4 (Maastricht, The Netherlands) software running in Windows 10 Pro environment. A processing pipeline, illustrated in figure 4.6, was elaborated. It contains, in the first place, a preprocessing carried out at the functional and structural levels, a functional-structural co-registration and, finally, a structural and functional normalization. Note that functional processing was performed in both block and event-related paradigm volumes. In the following sections, I will address each of these steps, in particular, what they consist of, their advantages and disadvantages, as well as the options selected for them and the reasons underlying those choices.

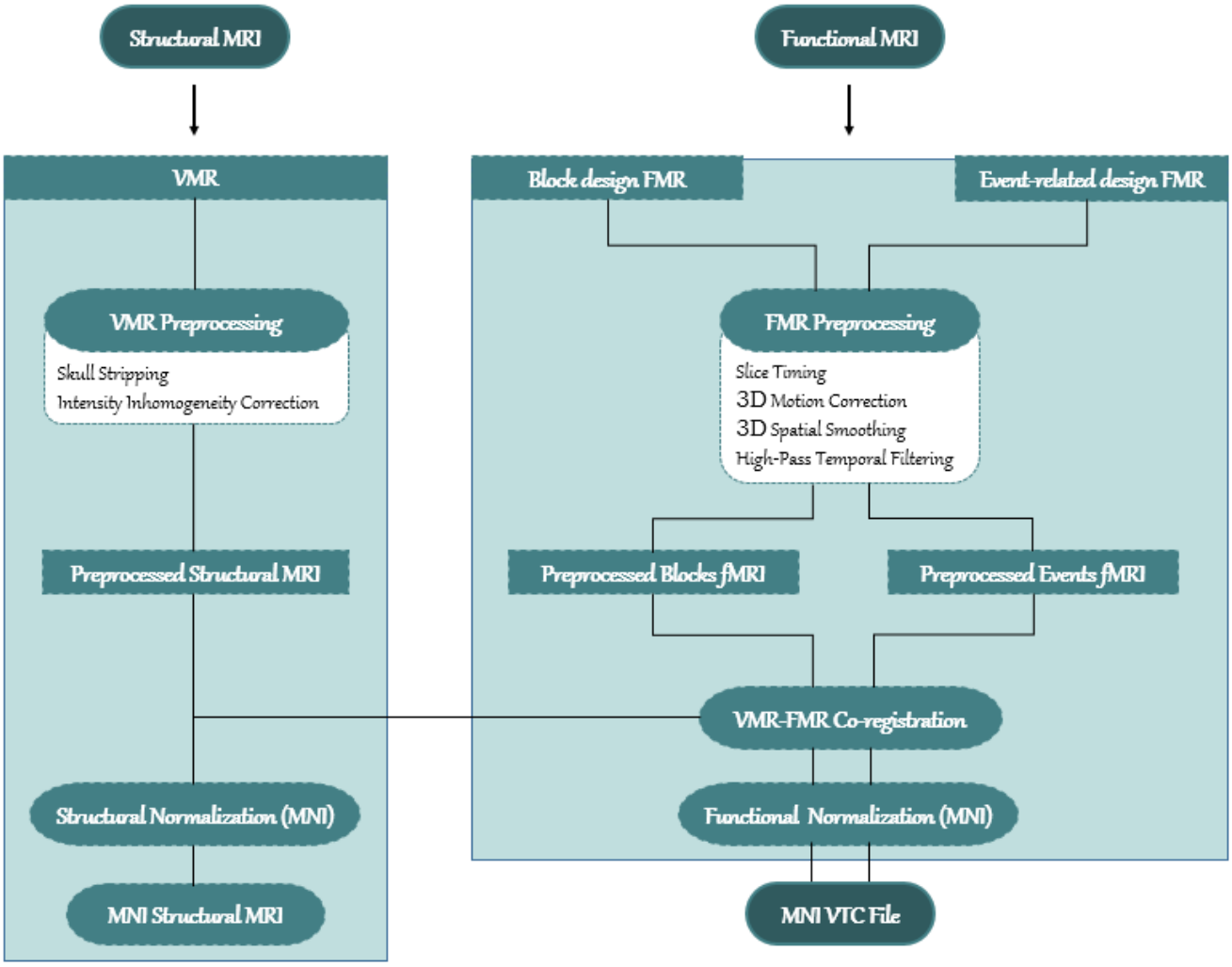

Figure 4.6: Processing pipeline implemented in this project's data.

Key: VMR - Volumetric Magnetic Resonance; FMR - Functional Magnetic Resonance; MNI - Montreal Neurological Institute space

4.2.1 Preprocessing

This stage aims to minimize the influence of data acquisition and physiological artifacts, to validate statistical assumptions and to standardize brain locations across individuals in order to reach greater validity and sensitivity in the group-level analysis [31].

4.2.1.1 FMR Preprocessing

4.2.1.1.1 Slice Timing Correction

EPI acquisition mode prevents a simultaneous visualization of the whole brain [94], yet, on the other hand, it enables a swift acquisition of single or multiple 2D slices, one at a time, and its stacking to create a 3D volume [95]. Although short and fixed TRs are used, an intrinsic delay between the actual and the expected acquisition times takes place, which may considerably decrease the ability to distinguish a certain effect [22], resulting in different slice scanning timings.

As a result, if time is imprecisely specified, a suboptimal statistical analysis may be produced, mainly in event-related paradigms [96].

In order to perform an accurate time series analysis on fMRI data, it is required to correct the time offsets between slices that come from the acquisition of individual slices [95]. Thus, Slice Timing Correction was applied, in which the time-course of the voxel data in each slice is adjusted through a time shift of each slice's time series to match the same point when the reference slice was scanned [96, 22]. Consequently, the data are changed as if the entire volume has been measured at the same time [96]. The time shift, in turn, depends on the order in which each volume slice was scanned, which could be ascending, descending, or interleaved, i.e., the slices were not acquired consecutively. However, this approach requires interpolation, which acts as a slice time-course resampling, in which the data from time points located halfway to the measured ones are resampled, estimating values from non-measured time points through measured datapoints located in the immediate vicinity [96].

With this step, the same predictors can be used all over the volume and can also be applied after transforming the slice-based representation of the functional data to a 3D data representation in an arbitrary space such as, for instance, MNI [96]. As a result, it is possible to correctly compare and integrate event-related responses from different brain regions at a common standardized time point [96, 31], concerning time parameters such as the onset latency, thus improving the statistical power of fMRI analysis [96].

In this preprocessing phase, the default settings presented by the software were maintained, i.e., cubic spline interpolation and interleaved slice scanning order determined from the header. Although it is not as fast, cubic spline interpolation was employed because it does not smooth the data as it uses more points in the neighborhood, resulting in a more accurate resampling. On the other hand, the applied slice scanning order accorded with the acquisition type produced by the MR (interleaved) and agreed with the overall assumption that the header information is usually the most accurate [96].

4.2.1.1.2 3D Motion Correction

Although participants are instructed to remain still during an MRI scan, that becomes practically impossible given the long duration of the examination, which makes head motion inevitable [97], especially in elderly and children [98]. Such a circumstance becomes a major source of error [31], creating severe problems at the most diverse levels. Firstly, in an MRI, the magnetic field is shimmed, i.e., fine-tuned for a certain head position before the functional scans are carried out, and with head motion, its homogeneity becomes diminished [96]. Secondly, an accurate spatial correspondence between voxels and anatomical areas over time becomes compromised [22], as the time-course of a single voxel would represent a signal derived from different brain parts, that is, local brain displacements mean that a voxel would have more than one location in the brain [97].

Even though head motion can be adjusted in the image space, if it is considerable, it can cause non-optimal shimming and motion artifacts which are not efficiently removed even after

a perfect realignment of successive functional volumes in the image space [96]. As a result, false but structured noise is generated, producing distance-dependent alterations in signal correlations [22]. In other words, the signal of neighboring voxels contaminates the intensity of a given voxel [31], therefore debilitating fMRI data quality and any sort of subsequent statistical analysis [96].

Given these reasons, it becomes imperative to realign each image in order to compensate motion [31]. This only becomes possible by applying 3D Motion Correction. First, the head is considered as a rigid body, whose motion is described by six parameters (three rotation and three translation parameters, on the X-, Y-, and Z-axis, respectively). However, this assumption is not entirely legitimate in fMRI data since the individual slices of a functional volume are not scanned in parallel, and these parameters are not enough to correctly capture within-the-volume motion and any abrupt head movements, which can arise at any time. Yet, as volume-to-volume head movements are typically small, the assumption of a moving rigid body becomes widely valid. Therefore, all functional volumes are aligned in space with a chosen reference volume, which consists of a functional volume from one run or another run of the same scanning session, by applying a rigid body transformation based on the previously mentioned parameters [96].

An iterative minimization algorithm based on a non-linear least-squares method predicts these parameters by analyzing how the source volume should be translated and rotated to better align with the reference volume [96], minimizing the sums of squared differences between the two volumes. When there are no further improvements, that is, when the best alignment is found, the algorithm stops [31]. After the final motion parameters have been detected, they can be implemented to the source volume, producing a new and corrected volume by replacing the original one in the motion-corrected dataset. This process therefore requires spatial interpolation, i.e., signal values need to be calculated at positions between measured datapoints [96].

The interpolation method employed as the default in head motion detection and correction was the Trilinear / Sinc Interpolation, i.e., a combination of Trilinear Interpolation for head motion detection and Sinc Interpolation for head motion correction. This approach turns out to have more quality, even though it is slower than just employing Trilinear Interpolation in both steps, since Sinc Interpolation results in corrected functional volumes that reflect the original data as close as possible, that is, without introducing spatial smoothing [96], while preserving a reasonable computation time [97].

Considering the presented software options, the chosen reference volume for motion correction was the first functional volume, and the align to run option was turned off. Regarding the first option, it aimed to align volumes within each session, that is, for each subject in each run, all the functional volumes were aligned to a reference one, in this case, the first that was acquired. As for the second option, motion correction itself corrects movements within each run to the reference volume. However, *in extremis*, there can be motion from one run to another, even if within a run it was vestigial, and this will affect the alignment since all runs will align with a different one. Therefore, this inter-run alignment was not carried out, and instead, in a further ahead step, both functional and anatomical volumes were aligned through co-registration. Hence, this approach ends up changing the data less and avoids errors arising

from the aforementioned circumstance. Thus, during motion correction, the volumes were only aligned to the first volume of each subject, for each run [96].

Note that, although there is no overall rule regarding the motion threshold to be used, datasets with head motion greater than the dimensions of one or two voxels or five or more millimeters are usually discarded from further analysis [96, 22].

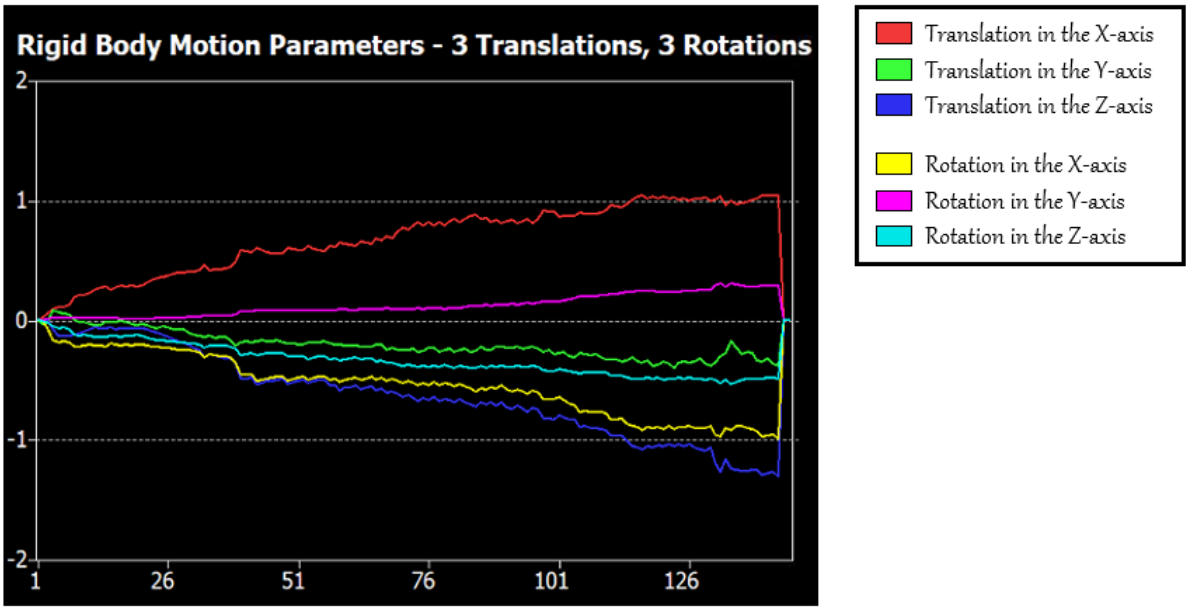

Figure 4.7: Representation of the results from the detection and correction of small head movements during a real-time 3D motion correction process.

Each of these six lines incrementally illustrated in this image is assigned to one of the six previously mentioned estimated parameters, which are indicated in the legend. The X, Y, and Z-axis respectively correspond to the left-to-right, top-to-bottom, and first-to-last (through the slices) directions [96].

4.2.1.1.3 3D Spatial Smoothing

During MR acquisition, images with random noise can be generated [99]. To reduce this effect and enhance the acquired signal, Spatial Smoothing was implemented, suppressing high-frequency signals while improving low-frequency ones, thus softening sharp edges. To this purpose, the fMRI signal is convolved with a Gaussian probability density function (kernel) [22], averaging part of the intensities from neighboring voxels together [100]. In other words, a voxel intensity is allocated to any of those voxels that fall within the smoothing kernel, thus changing their time series [95].

This process increases the SNR, both at single-subject and group levels. At the single-subject level, Gaussian noise, which is random and independent from voxel to voxel, and whose values approach zero, will have a zero-value average. On the other hand, the fMRI signal will tend to some non-zero value [101], thus eliminating intra-subject differences [31]. At the group level, anatomical and functional clusters existing in the same anatomy considerably vary between

subjects. Therefore, this process maximizes between-subject overlaps in a certain cluster, enhancing signal sensitivity, and consequently improving across-subject comparisons, by increasing the probability of detecting clusters at the group level [101]. As a result, the validity of future statistical tests also rises by providing a better fit to the expected assumptions while reducing anatomical and functional differences. However, Spatial Smoothing reduces the effective spatial resolution of each image, it can attenuate small yet significant local activations that depend on the filter parameters chosen [22], and it shifts activation peaks, or merges them, when they are less than twice the FWHM apart [100].

The function size, defined by the FWHM and usually expressed in millimeters, establishes the extent to which the smoothing will be implemented, depending on certain features regarding the performed study, such as type of paradigm and inference expected, or primary image resolution [22]. Acknowledging the advantages and disadvantages of this process, a compromise between the SNR and the functional volume's resolution must be reached [99]. Thus, the smoothing amount should always be the minimum required to accomplish the desired results, because the wider the kernel, the harder will be to detect small activation patterns [22], since both the signal and the noise will decrease [99], and if the width is set too small, the SNR becomes impaired while reducing spatial resolution [101]. There is no overall answer as to what is the best width to analyze the dataset. According to the Matched Filter Theorem, the SNR will be maximum when the size of the kernel corresponds to the size of the sought region, which in turn will depend on the experimental design and on the analyzed regions [101], although it is not known how large it will be *a priori* [100].

Considering the presented software options, the 3D Gaussian Spatial Smoothing option was selected. As the resolution of the functional volume voxels was 3 x 3 x 3 mm, by applying the Matched Filter Theorem, the best SNR is given to a kernel with the same size as the voxel, i.e., in this case, 3 mm. Therefore, a FWHM of 3 mm was employed.

4.2.1.1.4 High-Pass Temporal Filtering

The detection of MRI brain activation resulting from stimuli presentation causes small variations in signal intensity over time [102]. The signal contains both the pure signal itself and the noise. The latter is not white, comes from several sources (physical or physiological noise) and mostly exists at low frequencies [103] commonly as linear drifts in the time-course of fMRI data voxels. If they are not considered, they might reduce the power of the statistical analysis data [96]. Therefore, it becomes crucial to filter the signal over time in order to improve the ability to detect true and reject false activations, by separating the noise from the stimuli-associated signal. Hence the signal remains preserved, and the SNR increases, which consequently improves the outcome of subsequent statistical analyzes [102] by using *cleaner* data [96].

To this purpose, High-Pass Temporal Filtering was performed, a process in which frequencies below a certain cut-off value were removed, and frequencies higher than the mentioned cut-off passed [96, 103]. One of the easiest ways of doing so is to remove separately linear drifts in the same course of each voxel, as they have a low frequency [96, 102].

This method is particularly important in brain regions that weakly activate, as it moderately increases the percentage of activated voxels [102]. However, it is one of the most dangerous methods for several reasons [103]. Firstly, neighboring voxels can exhibit several different drifts [96], so it becomes difficult to predict the amount and direction of a drift [102]. Then, the exact choice of the period of interest turns out to be ambiguous because if there is a signal regarding the activation of a certain region with a frequency lower than the cut-off, the filter will remove it along with the noise, which ends up worsening the result. Therefore, the choice of the cut-off frequency becomes extremely important, and its value should be the double or the triple of the fundamental frequency of the experiment, i.e., the time between the beginning of one trial and its ending, so that it does not filter anything close to the fundamental frequency [103].

During data preprocessing, High-Pass Temporal Filtering was implemented by using Fourier analysis. The cut-off frequency was also specified, from which all frequencies below this value were removed. This frequency was expressed in cycles, with each cycle corresponding to a sine wave (from 0 to 2π) that spreads over the number of time points in the fMRI data [96].

However, as this method does not work well for purely linear trends, the software intrinsically applies a linear trend removal before the Fourier analysis, estimating a linear trend by fitting a line through the data, computing its slope and interception. Then, by applying a Fast Fourier Transform (FFT), the time-course of a voxel is transformed into the frequency domain, and it becomes represented by a sine and cosine curves. The Fourier analysis is then applied, estimating a frequency which can contribute to a drift. That frequency has two values: one for the sine curve and another for the cosine curve, and it can be used to determine the frequency intensity of the data. Consequently, the low frequencies are removed by setting their values to zero, and the data are then transformed back into the time domain, which will no longer owns the data corresponding to the removed low frequencies [96]. As a result, in the time domain, the time-course is straightened out when gradual bends or drifts occur and are flattened away after filtering. In the spatial domain, on the other hand, the edges of the image are shown [103].

This step was carried out on the functional volumes of both paradigms, considering the total length of the basic stimulation units of each run, which, according to the protocols implemented in this study, were two: stimulation and fixation. By adding these two units, doubling the result, and estimating the inverse of this value, the cut-off frequency was obtained.

Based on the implemented protocol [12], in the block paradigm, there were 29 alternating blocks: 14 visual stimulation and 15 basal fixation blocks, each one lasting 12.5 s. Therefore, the set of the two conditions was equivalent to 25 s, that doubled, made up the value of 50 s, which consequently corresponded to a 0.02 Hz cut-off frequency. However, the filtering was executed in cycles, so, in this paradigm, by converting this value into cycles, that frequency equaled to 6 cycles in the time-course from which temporal filtering was applied.

In the event-related paradigm, the two conditions were presented 20 times, with visual stimulation lasting 0.4 seconds and basal fixation randomly varying between 4.6, 7.1 or 9.6 seconds. Given these circumstances, the highest value was considered as the length of the fixation condition, as it results in a lower frequency, and because smaller time ranges (consequently,

higher frequencies) resist larger time range (lower frequency) high-pass. Therefore, the set of these two conditions was equivalent to 10 seconds, that doubled, made up the value of 20 seconds, which consequently corresponded to a 0.05 Hz cut-off frequency. This value equaled to 15 cycles in the time-course from which a temporal filtering was implemented.

However, although signal variations with stimulation frequencies above 0.05 Hz can pass through a 15-cycle filter, due to safety reasons, so that frequencies with the mentioned value could also pass through it, the number of cycles was reduced to a random value within an acceptable range. Thus, given that in the block paradigm, a 6 cycles filter was applied, for the event-related design, it was chosen a 12-cycle filter.

4.2.1.2 VMR Preprocessing

The structural volumes underwent the steps indicated in figure 4.6, which represents the processing pipeline. It should be noted that as these contained a spatial resolution of 1 mm x 1 mm x 1 mm, considered ideal, it was not required to interpolate the data set in order to rescale the resolution [96].

4.2.1.2.1 Skull Stripping

During an MRI scan, structural brain volumes contain more non-brain tissues (scalp, skull, dura-mater, eye sockets, or other peripheral tissues) than functional volumes [104, 105]. These tissues end up becoming major obstacles for cerebral tissue classification (cerebral segmentation), image co-registration, or volumetric analysis [106]. Therefore, it becomes essential to extract them in order to achieve more accurate results [104], despite the extremely complicated brain anatomy. To this purpose, Skull Stripping was implemented, a process in which the brain tissue (cortex and cerebellum) was isolated from the aforementioned tissues [107].

Given the imprecise nature of brain images, which are acquired on different machines and may have different contrast and quality, and since brain structures are heterogeneous and vary among individuals, Skull Stripping becomes a sophisticated and challenging method [104]. However, it does end up containing some dangers, as any accidental tissue removal cannot be reversed in later processing stages [106]. Thus, in this process, it becomes crucial to find the cerebral and cranial borders [107]. To do so, the brain is extracted using a binary representation of the data and morphological operations. First, the binary image is eroded so that it can split intensity connections between brain and non-brain tissues. Then, the largest connected component retained - which is usually the brain - is determined, while all the others are set to zero, and then a reduced version of the brain is extracted [96]. Finally, in order to re-add the tissue removed at the brain borders by the previously mentioned erosion, the latter is reversed, by performing a dilation restricted to voxels in the brain neighborhood [96, 108].

4.2.1.2.2 Intensity Inhomogeneity Correction

During MRI image acquisition, smooth shading artifacts have been frequently found, in which voxel spatial intensity values significantly vary within the same tissue and prominently overlap in different tissues [109]. In other words, white matter voxels located in one place may have the same intensity as gray matter voxels located elsewhere in the same image [96]. This effect is known as intensity inhomogeneity or *bias field*, and it is due to the instrumentation (non-uniformity of the RF coil, static field inhomogeneity, among others), or to the participant's motion [109]. As a result, it significantly deteriorates and compromises both the performance and the accuracy of any image processing algorithm that uses intensities as its main features - in particular, segmentation and image registration, as these profoundly rely on image quality [110] - and it also reduces the reliability of subsequent quantitative and qualitative measures [109].

Therefore, it becomes crucial to reduce the aforementioned inhomogeneities on structural volumes [96], improving their processing as well as their output. To this purpose, during the image preprocessing, it was performed the Intensity Inhomogeneity Correction (IIHC).

The method that the software implemented in this process allowed, by using the least-squares algorithm, to fit low-grade polynomials to a subset of voxels labeled as white matter voxels and to analyze low-frequency intensity variations, in order to estimate a bias field. The latter was estimated twice and after that, in order to increase the process efficiency, it was removed from the dataset. As a result, an image with much more homogeneous intensities that improve the visualization and are also better starting points for following segmentation tools was obtained [96].

It should be noted that before carrying out the process itself, it was required to clean the image background, extract the brain, and detect the white matter. To clean the image background, the intensity values of the background voxels are set to zero. However, as the intensities of the background voxels vary, the image becomes binarized, i.e., the intensity values greater than zero are set to the same integral value to optimize this cleaning and to avoid *salt and pepper* noise. Therefore, an intensity histogram is performed, allowing to detect the largest connected component (the head-brain complex), as well as the lower intensity voxels. The latter, which correspond to the background, are set to zero intensity and then removed. As for the brain extraction, mentioned earlier in section 4.2.1.2.1, it produces a more accurate estimate for the bias field, as it is only focused on brain tissue. Finally, concerning the white matter detection, due to the existing spatial inhomogeneities, it is not possible to select only the high-intensity value voxels that, theoretically, would reflect the white matter voxels, since gray matter voxels in bright image locations (high SNR) may have higher intensity values than white matter voxels in dark image locations (low SNR). Therefore, the image is analyzed from blocks with 125 voxels (5 x 5 x 5), selecting the highest intensity values and heuristically verifying if the intensity distribution within one block comes from one or two tissue types. Although this authentication does not guarantee a correct separation of white and gray matter voxels, there is a very high chance to include a large sub-part of white matter voxels in the remaining set of voxels. This step is repeated once more, which in turn improves the white matter classification

validity and, consequently, the resulting homogeneity, with the separation between white and gray matter displayed when the intensity histogram is plotted at each iteration. As a result, a segmented and homogeneous brain was determined, with a gain in gray and white matter separation and within-tissue homogeneity [96].

4.2.2 Co-registration

To more accurately detect and locate brain activation sites after exposing an individual to a stimulus [111], one must consider the head motion effects during image acquisition [112]. Therefore, it is important not only to correct the motion between slices from the same functional run (as mentioned in 4.2.1.1.2) but also to correct the movement between structural and functional scans [113].

Regarding the latter case, co-registration was implemented, aligning functional and structural volumes of the same subject [114], acquired at different times [112] in the same geometric space [115], by its overlap [114]. Co-registration can be intramodal, in which it is applied to the same imaging modality (for instance, fMRI-MRI), or intermodal, in which it is applied to different imaging modalities (for instance, PET-MRI) [115].

Therefore, co-registration enables one to correlate structural and functional data of the same participant, ensuring their correspondence [114] without changing the coordinated system of the structural volumes [96], as well as reducing partial volume effects in voxels that contain multiple tissue types with different signal features when the image is segmented, such as, for instance, gray and white matter [112].

First, the co-registration itself took place, in which a set of parameters describing the transformation that best matches the volumes was estimated [111]. As a rule, the first or the mean functional volume (usually connoted as source) is co-registered to a simple structural volume (usually connoted as target) [96, 31]. Then, the transformation took place, where one of the volumes was iteratively transformed according to the estimated parameters [111], in order to optimize them, minimizing the disparity degree between structural and functional data after each iteration [116], and consequently, improving transformation [111]. Based on the implemented transformation, co-registration can have two algorithm types: linear and non-linear co-registration. Linear co-registration is the most commonly used method and, to model the local deformation [114], it assumes that the image geometric proportions remain constant [117]. Therefore, it usually involves a rigid transformation of six parameters (rotation and translation in the three axes) or a affine of twelve parameters (rotation, translation, scaling and shearing in the three axes). Non-linear co-registration is a more precise and elastic [114, 111] but more complex method, in which a computed warp from a more detailed structural volume is applied to the functional volumes. As a rule, linear transformation methods are used, however, when fMRI images are usually distorted, it is preferable to use a non-linear method [111].

However, as each set of structural and functional datasets was acquired in the same session and came from the same individual, in this processing step, a linear intramodal co-registration was systematically applied to the sample of study participants, in each run of each paradigm. In

this process, two steps were implemented: Initial Alignment (IA) and Fine-Tuning Alignment (FA). IA was predefined by the used software as the minimum step required to carry out the co-registration, and it aims to bring the functional and structural datasets closer from a potentially disparate starting point. As the two datasets were acquired in the same session, and as the file format used to import the data - Digital Imaging and Communications in Medicine (DICOM) - contained the required positioning information in its header, a header-based mathematical coordinate alignment was carried out in this step. In this method, first it was checked if the header information associated with the slice positioning was available for both datasets and, if so, the software saved it in new FMR and VMR files. Afterward, the alignment was computed, but any transformation applied to the datasets after the project has been created was always considered in order to compute the correct mathematical spatial transformations [96].

On the other hand, FA assumes that the two datasets are already very close to each other, and it requires them to be sagittally oriented to improve co-registration by correcting small head movements that occurred between structural and functional acquisitions. Among the multiple options available on the software, Gradient-based Registration was chosen over Boundary-Based Registration (BBR). Although both appear to yield similar results, the latter is much more time consuming and takes up more computer memory since a segmentation of each structural VMR file is performed to obtain a white/gray matter cortex mesh [96]. The gradient-based registration method implemented was the Normalized Gradient Fields (NGF) registration, and it is based on the idea that intensity changes in an image [118] - which strongly rely on data inhomogeneities [96] - can define its structure, and consequently, characterize similarities, given that two images are considered similar if intensity changes occur in corresponding locations [118]. NGF assumes that image intensity change gradients, which represent tissue boundaries, may not have the same magnitude in different images. Therefore, the greater the similarity degree between intensity changes in corresponding positions in different images, the more similar the values of the corresponding gradients and the smaller the inner angle between them will be [119]. Thus, this method implements co-registration by minimizing the stated angle in the mentioned positions, to turn the alignment between gradients and, consequently, between images, as parallel or antiparallel as possible [120]. When this method was selected, the Anatomical Magnetic Resonance (AMR) file used to visualize the FMR data was specified as the functional source of the co-registration, since it allows to obtain results with greater resolution than using the first volume of the selected functional data itself [96].

Although NGF requires a gradient-dependent cost function [121], it does not depend of absolute intensity differences between corresponding areas in different image types [122], since gradient information assesses signal intensity changes concerning neighboring voxels [96], which turns out to be useful to co-register images acquired during different breathing phases [122].

Secondly, co-registration was assessed after its implementation. In this small step, the results from the reports the software created after the stated step took place were analyzed to identify subjects with weak or mediocre co-registration. For them, an extra step was then made: a manual co-registration for each subject at an individual level, to improve the results.

For each of these subjects, after the preprocessed AMR file was loaded, the corresponding preprocessed FMR file was paired to perform the manual co-registration. However, when the AMR file was not available or not able to be used in this step, it was replaced by the first volume of the functional data series. Both IA and FA were employed using the same methods as those referred in the systematic analysis, i.e., header-based mathematical coordinate alignment and gradient-based alignment, correspondingly. In FA, it should be noted that a full affine transformation of 12 parameters (rotation, translation, scaling, and shearing in the three axes) of the functional volumes was carried out, enabling real-time monitoring, and the parameter estimates were iteratively updated. After this process had reached its end, the co-registration results were shown in a window, overlapping edges resulting from overlaying the functional volume of reference with structural volumes to better assess its quality, and the estimated parameters were displayed in a menu [96]. Then, as the results were not yet ideal, to improve them even further, small adjustments were made by manually optimizing transformation (translations and rotations in X, Y and Z) values, so that the edges of the functional volume could better match the structural volume. Finally, the changes created in this new co-registration matrix were saved, replacing the old one resulting from the systematic analysis.

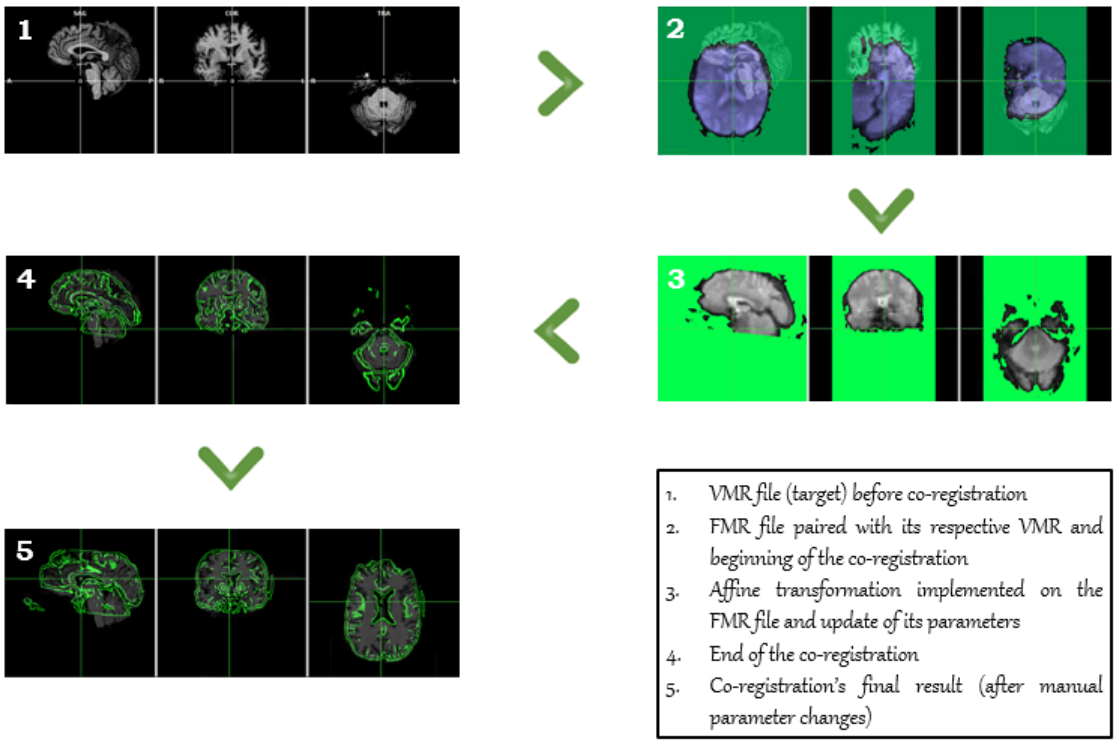

Figure 4.8: Representative scheme of the manual co-registration stages.

It should be noted that, as mentioned in 4.1.1, one participant was discarded from the database, which from now on included 141 participants, given that good results were not achieved even when the estimated parameters were manually adjusted after performing the manual co-registration at an individual level.

4.2.3 Normalization

In MRI there is a vast inter-subject variability since each individual's brain differs in shape and features [31], the positioning of individuals between locations may vary, and images from different scanners or different acquisition parameters can widely vary in intensity. Consequently, MRI processing performance and statistical group analysis become compromised, increasing the rate of false negatives and decreasing sensitivity. Thus, in order to correct such variations and to optimize processing [123] and the performance of group analyzes, improving the results, it becomes crucial to align homologous brain regions between individuals [22]. In other words, it is required that each voxel is in the same spatial location for all subjects [31].

To this purpose, it was implemented Normalization, a process in which spatial transformations such as translations, rotations, or scaling, were applied in several axes [22], minimizing differences between brain images of a subject [124] and a common reference space [116], by placing them in a similar position in similar sizes, thus allowing their alignment and subsequent comparison [125]. The commonly used reference space is a standard anatomical stereotaxic atlas [126], defined by a brain template in a specific coordinate system, which allows to locate certain anatomical features in the coordinated space, as well as to associate functional results with anatomical regions [22]. Therefore, when this operation is made for several subjects, the brain images of all subjects spatially correspond to the same reference and, consequently, to each other, in such a way that a point in the common space identified by its x, y and z coordinates is assumed to be in a similar region in any brain normalized according to the same procedure [96].

Thus, the processing of acquired MRI data included a normalization, in which, in the first place, a transformation matrix was computed from a structural volume, and later applied to both files (VMR and FMR Normalization) since they had previously been co-registered.

4.2.3.1 VMR Normalization

The structural volume normalization took place first. A transformation matrix was computed from the anatomical data to the MNI space, which is based on a T1-Weighted MRI scan average [22], and then applied to the structural volumes.

4.2.3.2 FMR Normalization

Then, functional volume normalization took place. The transformation matrix, computed from the spatial normalization of anatomical data to MNI space, was applied to each functional volume, which was previously co-registered with the corresponding anatomical data in the native space. Functional volumes over time were then compiled into Volume Time Course (VTC) data in the MNI space, and the spatial resolution of this 3D functional series was adjusted according to the structural data resolution. Since the functional volume resolution was 3 x 3 x 3 mm, and the structural volume resolution was 1 x 1 x 1 mm (as seen in table 4.2), it was set that 1 VTC voxel corresponded to 3x3x3 VMR voxels. In order to perform this data resampling, it was required a spatial interpolation, and therefore, a Sinc Interpolation was employed. Finally, after creating the VTC data, the latter and the anatomical data were used for a statistical analysis.

4.3 Data Analysis

4.3.1 The General Linear Model

After processing all the experimental data to correct potential artifacts introduced in its acquisition, a statistical analysis was performed on the fMRI time series using the GLM. Before explaining how it was performed, I will give a brief introduction to this statistical model.

The GLM allows to model the perceived signal in one or more explanatory variables, the regressors, by a linear combination [127], to better explain or estimate, and to what extent, how each regressor contributes to the variability of the data [128]. The matrix equation for this model is given by the following formula [127]:

$$Y = X\beta + \epsilon \tag{4.1}$$

where, in the current situation, Y is the column vector that contains the dependent variables, representing the BOLD signal time-courses associated with each voxel [128]. On the other hand, X is the design model or matrix, whose rows correspond to the number of observations (in this case, volumes) [129], and whose columns are the independent variables, also known as predictors, regressors, or covariates [127]. Predictors of interest, which are determined according to the task taking place during data acquisition, aim to explain the signal variation across time. As it is expected that the BOLD signal will fluctuate per ROIs at least according to neuronal activation due to the performed task, predictors associated with one or more periods of interest are built from a convolution of a box-car time-course condition (representing active neuronal populations at a specific time point) with an HRF [128]. These predictors represent the effects expected to be found in the measured signal [127] due to the coupling of the hemodynamic response with neuronal activation.

From Y and X, the model estimates a set of weights for each predictor, which mark the magnitude and direction of the univocal correspondence between each predictor and Y, thus describing the voxels' preference for one or more experimental conditions [128], to better explain or allow data prediction. Therefore, one has the column vector β, which contains these values, known as beta weights, individual effect or scaling parameters [96]. As a rule, a high positive (negative) beta weight implies that the voxel exhibits a significant positive (negative) signal change during a certain experimental condition modeled against the baseline, where no activation (deactivation) is expected to take place [128].

Furthermore, the multiplication between β and X allows to get the time-course values of the fMRI responses predicted by the model in different conditions of the experimental paradigm. The closer these values are to those existing in Y, the better the model fit, and consequently, the smaller the difference between them is [96], with this value being represented in the column vector ϵ, which is called noise, residual error or residues [127].

As brain scans are represented by thousands of voxels, in each one there is a BOLD signal time series. Therefore, GLM is performed voxelwise, i.e., separately on each voxel, and in each separate analysis, the dependent variable is a set of data values for each voxel - in which each estimated β will differ - with the best fit depending on the set of the existing data values [127].

As mentioned in section 4.1.3, two types of GLM analyzes were performed. Next, I will further explain how each one of them was implemented.

4.3.1.1 Standard GLM Analysis

This analysis was performed in two levels. First, the beta weights from each experimental condition were individually estimated for each subject. In a second step, the beta weights of all subjects were provided as an input for a second-level group analysis, in which group effects were estimated, considering the beta weights themselves and their inter-subject variability. Hereupon, after obtaining the VTC files for each subject through functional normalization, the first and the second-level statistical analysis were simultaneously performed, using a Multi-Study Multi-subject GLM, in which brain regions with greater positive (and negative) signal change for the experimental conditions were detected for the study sample.

Firstly, it was required to create an individual predictor matrix according to the acquisition protocol. To this purpose, given their greater statistical power, only block paradigm protocols were considered in this analysis. As they were four different protocols in this paradigm (as described in 4.1.3), four different predictor matrices were created.

It should be noted that when all experimental conditions are modeled as predictors in the design matrix, including the baseline condition (fixation/control), we find ourselves in a situation known as of statistical multicollinearity, in which the design matrix predictors are highly correlated. Multicollinearity can be avoided by not including the baseline condition in the GLM, and thus, beta weights can be more easily interpreted, as they will correspond to an increase or a decrease in the relative activity regarding the baseline signal level modeled by the constant term [96]. Therefore, as the first condition of each protocol concerned the baseline or resting condition, known here as Fixation, to avoid this problem when creating the predictors' individual matrix, it was determined that the first condition would be excluded from the individual design matrix.

Then, the VTC files for each run of each subject, in all subjects, were paired with the respective single design matrix. Also, as there is a large number of study subjects [129], which are considered as a representative population sample, a random-effects analysis (RFX) was combined with the GLM, using percent signal change transforms, as these reflect the size differences of the effects better than z-transforms [96]. This analysis verifies whether the magnitude of a group effect is significant concerning inter-subject variability [128]. If so, the results from a subject sample can be generalized to the population from which they have been selected [96].

During GLM, autocorrelation may occur in fMRI data, that is, high values are more likely to be followed by high than by low values, and vice versa. Autocorrelation analysis, however, is

carried out in the residue time-course since this effect is expected to a certain extent from slow fluctuations regarding the task. Although the β values estimated by the GLM are unbiased even with this phenomenon, their standard errors are not, causing an inflation of the test statistics, i.e., the t- or F-values are higher than expected. Thus, it becomes crucial to correct these correlations, which was done when the RFX-GLM analysis was performed, using the software's default approach. The latter allowed to estimate and remove the data and model autocorrelation, and to refit the GLM, assuming that the errors followed a second-order autoregression process (AR(2)) [96], instead of a first-order autoregression process (AR(1)), optimizing the results [130].

The GLM allows one to ask questions of interest regarding the analyzed conditions, which can only be done by using contrasts. These are mathematical inequalities formed by a linear combination of the different effects and their size [127]. In this case, it was intended to locate the ROIs with overall engagement in the stimulation task implemented in the block paradigm. Thus, a *stimulation conditions vs. baseline* contrast was studied, which, even though a bit rough, allowed to obtain a block task group map. This map aimed to understand which brain regions contained significantly activated (deactivated) voxels that responded to any of the stimulation conditions against the baseline, to then be further investigated with a subsequent GLM analysis.

However, when a statistical test is performed, a statistical threshold is used to control the probability of false positives [131]. In this case, in a voxel, assuming the standard critical value of 0.05 as a probability threshold, and a null hypothesis which is always true [96], when the p-value is less than the mentioned value [132], there is at most a 5% likelihood of rejecting it even if it is actually true [96]. As a result, due to chance [132], a voxel could be labeled as significant, when it is not. Nevertheless, when the number of voxels (samples) to which a statistical test is simultaneously carried out is increased, as in this case, which is statistically equivalent to executing several statistical tests in a single voxel, a multiple comparisons problem arises [96]. That is, and considering the previous threshold, if the null hypothesis is always true [132], about 5% of all analyzed voxels would be labeled as significant, even though they were not, which would, therefore, result in about 5% false-positives [96]. Hence, the greater the number of voxels tested, the greater the number of false-positive voxels [131]. To balance this problem, methods which adjust the probability thresholds are used [96]. Regarding that, in this case, the probability threshold must be more rigorous to reduce the number of voxels (and hence, brain regions) wrongly considered as significant (false-positives) [131] and thus globally achieve the original level of significance [133], a Bonferroni correction method was applied for a 0.05 p-value. Bearing in mind the equation 4.2, the original p-value was diminished 141 times [131], resulting in a quite robust block task group map (figure 4.9), considering the high number of participants.

$$Bonferroni\ adjusted\ p-value\ = \frac{a}{N} \tag{4.2}$$

With:

a: original threshold (0.05)

N: number of independent tests / group samples (141)

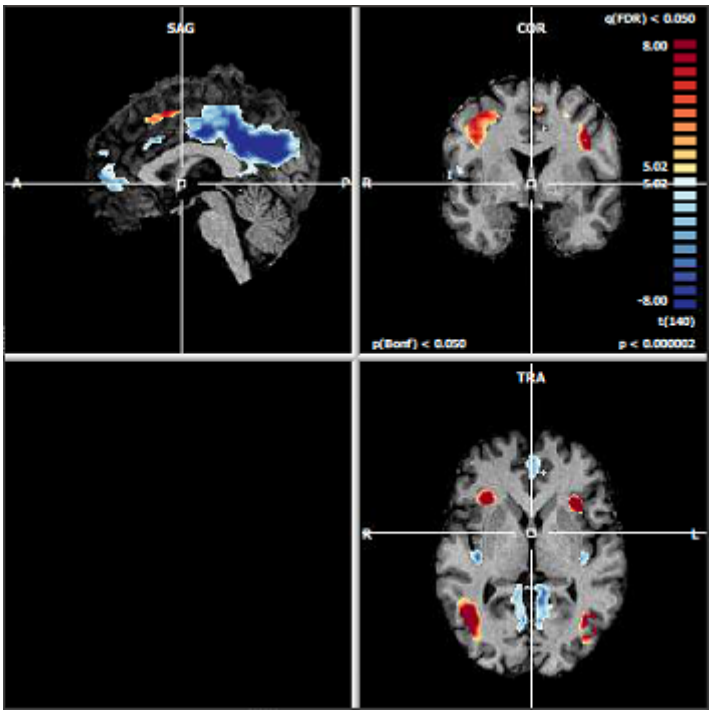

Figure 4.9: Block task group map with positive and negative signal change clusters resulting from the GLM.

Based on the previous map, in which the Bonferroni correction was applied, as mentioned in 4.3.1, from the most significant positive (in red) and negative (in blue) signal change clusters, as shown in figure 4.9, as well as the MNI coordinates of each cluster, using two atlases [134, 135], the following ROIs and consequent Brodmann areas (BA) were defined for further analysis:

Table 4.3: Descriptive information regarding each of the positive signal change clusters selected from the block task group map.

Positive signal change clusters				
Anatomical Brain Region	**Cluster Code**	**MNI coordinates at the cluster's peak**		
		X	**Y**	**Z**
Left Inferior Parietal Lobule, Brodmann area 40	L_IPL_BA40	-30	-46	40
Left Insula, Brodmann area 13	L_Insula_BA13	-30	23	4
Left Precuneus, Brodmann area 7	L_Precuneus_BA7	-24	-52	44
Right Inferior Frontal Gyrus, Brodmann area 9	R_IFG_BA9	45	11	25
Right Middle Frontal Gyrus, Brodmann area 8	R_MFG_BA8	6	17	46
Right Middle Frontal Gyrus, Brodmann area 46	R_MFG_BA46	48	26	25
Right Superior Frontal Gyrus, Brodmann area 6	R_SFG_BA6	6	8	53
Right Superior Parietal Lobule, Brodmann area 7	R_SPL_BA7	30	-57	46
Right V2 area, Brodmann area 18	R_V2_BA18	29	-73	22
Right V5/MT area, Brodmann area 19	R_MT_BA19	46	-64	9

Table 4.4: Descriptive information regarding each of the negative signal change clusters selected from the block task group map.

Negative signal change clusters				
Anatomical Brain Region	**Cluster Code**	**MNI coordinates at the cluster's peak**		
		X	**Y**	**Z**
Left Anterior Cingulate, Brodmann area 32	L_AC_BA32	0	44	1
Left Cingulate Gyrus, Brodmann area 31	L_CG_BA31	-3	-46	32
Right Cingulate Gyrus, Brodmann area 24	R_CG_BA24	-3	-10	43
Right Insula, Brodmann area 13	R_Insula_BA13	37	-19	4
Left Posterior Cingulate, Brodmann area 30	L_PC_BA30	-6	-55	13
Right Posterior Cingulate, Brodmann area 23	R_PC_BA23	-3	-45	28
Left Paracentral Lobule, Brodmann area 5	L_PrcL_BA5	-12	-37	49
Left Parahippocampal Gyrus, Brodmann area 36	L_PrhG_BA36	-30	-31	-17
Right Precentral Gyrus, Brodmann area 4	R_PrecG_BA4	36	-19	40
Right Precentral Gyrus, Brodmann area 43	R_PrecG_BA43	54	-7	11
Right Primary Sensorial area, Brodmann area 1	R_PrimSens_BA1	39	-16	19
Right Superior Temporal Gyrus, Brodmann area 39	R_STG_BA39	52	-55	19

4.3.1.2 GLM Deconvolution Analysis

Since the fMRI signal consists of a stimuli function convolved with the HRF, it is possible to estimate the latter by reversing the convolution process, i.e., by performing a deconvolution [136]. Therefore, in each of the ROIs identified by responding to the block paradigm stimulation task, a GLM deconvolution was implemented to estimate the HRF through the response to the presented stimuli. To this purpose, event-related runs were used in this analysis, since, contrarily to block paradigms, they own an increased sensitivity for estimating responses to short stimulation events, which allow them to separate contributions from different stimuli [137].

Deconvolution GLM is an alternative GLM analysis, in which each protocol condition encodes a set of *stick* predictors, each of them separately estimating the HRF amplitude at a datapoint regarding the onset of that condition. In the end, the series of amplitude estimates describes the current HRF shape in each condition. To enable this, it is assumed that the HRF, which is not fixed, is linear and has a finite number of datapoints. As a consequence, the model has a more flexible fitting, allowing one to compare conditions on a single point data basis. However, by providing a higher number of degrees of freedom, this analysis has a larger sensitivity to noise and a possible specificity loss when it is performed voxel-by-voxel [138].

In order to perform this analysis, carried out similarly as in 4.3.1, it was also required, first, to define an individual predictor matrix. Therefore, as this is a deconvolution analysis, an individual deconvolution matrix was defined, but instead it used the event-related paradigm protocol due to aforementioned reasons.

As in the individual predictor matrix in the standard GLM (4.3.1), the first condition of the protocol, which concerns the baseline (Fixation), was excluded from the individual deconvolution matrix to avoid multicollinearity problems. Furthermore, it was also considered that, given a 2.5-second acquisition TR, as only the first 20 seconds of the HRF curve were intended, then, as each datapoint in the design matrix corresponds to a TR, it was considered that, only eight datapoints (8 x 2.5 s = 20 s) would be needed for this same matrix. Then, the multi-study deconvolution matrix was produced, and, just as before, the event-related paradigm VTC files

of each subject, resulting from functional normalization, were associated with the produced single design matrix, for all subjects.

Finally, the GLM deconvolution analysis was estimated for each pre-defined ROI. In order to perform this step, all the defined ROIs were loaded, and the group deconvolution matrix created was linked. Next, in all subjects, for each ROI, and in each condition, the beta weights and statistics were calculated, and corrections of series correlations were made, assuming that they followed a first-order autoregression model.

4.3.2 HRF Analysis

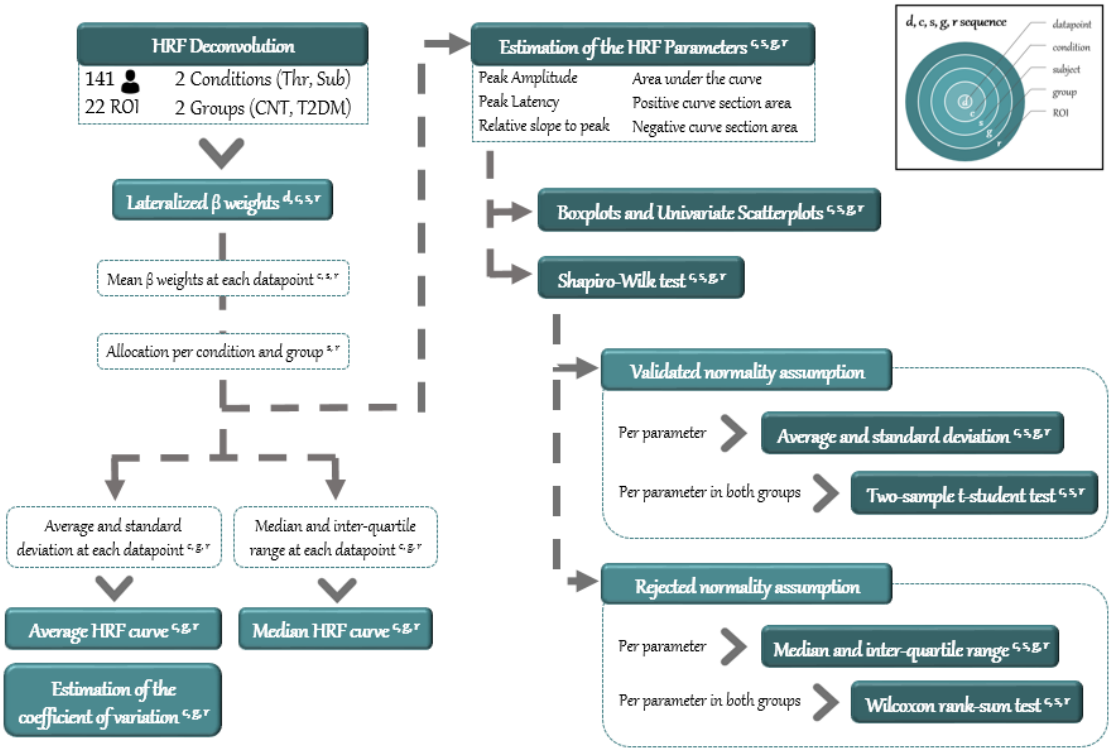

Figure 4.10: The HRF analysis pipeline implemented in this project.

From all the data stemming from the GLM deconvolution analysis, the series of beta weights which describe the estimated HRF in the corresponding lateralized stimulation conditions for each subject and in each ROI were selected in order to carry out the subsequent analyzes that I will address further on.

4.3.2.1 Estimation of the Average and Median HRF curves

From the aforementioned beta weights, whose conditions were differenced according to the sides (Left and Right), the mean beta value in each condition (Threshold and Submaximum) was first calculated for each datapoint, in each subject, and for each ROI, according to the following equation:

$$\overline{\beta} = \frac{\beta_{\text{Left Threshold/Submaximum}} + \beta_{\text{Right Threshold/Submaximum}}}{2} \tag{4.3}$$

After all these values had been allocated and organized according to the condition and to the group (CNT or T2DM) to which they belonged, in each subject and for each ROI, the average and the standard deviation of all beta weights regarding the CNT and T2DM populations were calculated in each datapoint of each condition for each ROI. Furthermore, in those same circumstances, the median and its interquartile range were also estimated, as it is a more robust measure and it gives an enhanced sense of a typical value, with less influence from outliers.

Finally, based on the calculated parameters, the HRF average and median curves were plotted in each condition and subject group, for each ROI.

4.3.2.2 Estimation of the Coefficient of Variation

Then, the peak amplitude and latency of the average HRF curves were determined per condition and per group, for each ROI. In order to ascertain how reliable and/or robust these two parameters were, their coefficient of variation (CV) was calculated in the same circumstances. This measure displays the variability of each of these parameters concerning the population's average, and it is given by the ratio between the standard deviation of the HRF parameter (peak amplitude or latency) and its corresponding absolute value in the average curve (Equation 4.4).

$$Coefficient\ of\ Variation\ (CV) = \frac{\sigma_{HRF\ peak\ amplitude}}{\mu_{HRF\ peak\ amplitude}}\ or\ \frac{\sigma_{HRF\ peak\ latency}}{\mu_{HRF\ peak\ latency}} \tag{4.4}$$

4.3.2.3 Estimation of the HRF Parameters

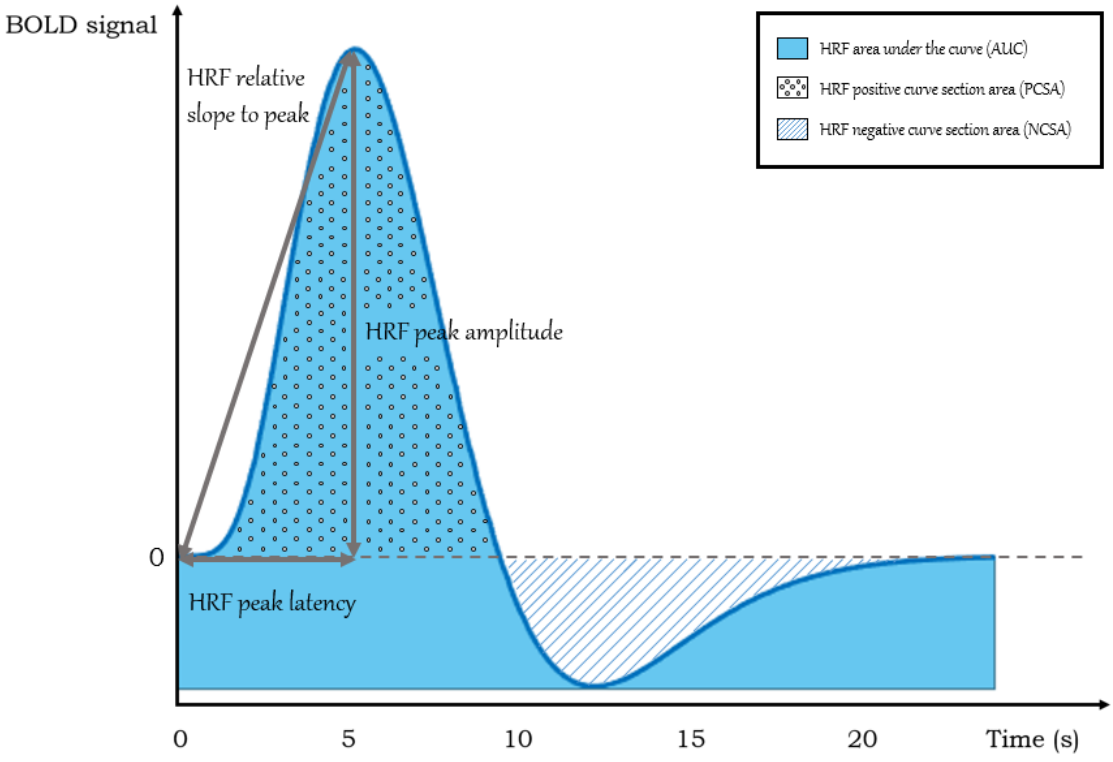

Figure 4.11: The HRF parameters of interest in this project.

Ensuingly, several HRF shape features were compared per ROI between the T2DM and CNT populations to assess whether there were any differences, and, if so, if they revealed any information regarding underlying neurovascular damage. Furthermore, the greater the amount of information regarding the HRF, that is, the larger the number of parameters, the more details about neuronal substrates of cognitive tasks can be obtained [139]. Thus, using the average beta weights in all datapoints, according to the condition and to the group, in each subject for each ROI, the following HRF parameters, which are portrayed in figure 4.11, were calculated: peak amplitude, peak latency, relative slope to peak, area under the curve (AUC), positive curve section area (PCSA) and negative curve section area (NCSA).

The HRF peak amplitude was estimated by determining the HRF curve maximum for the range of datapoints that corresponds to the period between 5 to 17.5 seconds, which is the time interval in which the HRF peak usually takes place [140]. In this estimation, it was also determined the datapoint where the peak looms, which, when multiplied by the TR (in seconds), according to equation 4.5, allowed the estimation of the HRF peak latency.

$$HRF\ peak\ latency\ (s) = HRF\ peak\ datapoint \times TR \tag{4.5}$$

The HRF relative slope to peak, in turn, was given by the ratio between the HRF amplitude variation between its peak onset and the initial instant (t = 0 s) and the time interval to the peak onset (HRF peak latency), as evidenced in the following expression:

$$HRF\ relative\ slope\ to\ peak\ = \frac{HRF\ peak\ amplitude - HRF\ initial\ amplitude}{HRF\ peak\ latency} \tag{4.6}$$

The HRF AUC was determined by applying the trapezoidal rule between the onset and the end of each HRF, as this is a numerical method which more accurately approximates this measure [141]. However, before implementing this procedure, the values of each HRF were rewrought in order to set its minimum value as the zero of the function.

Regarding the HRF PCSA, the trapezoidal rule was implemented between the positive HRF values and the values where the function was equal to zero. Likewise, for the HRF NCSA, the same happened, but with the negative HRF values.

4.3.2.4 Univariate Scatterplots and Boxplots

In order to find patterns in the values of each parameter from each subject, in each condition and group, for each ROI, thus showing relationships between them from the analysis of their distribution and dispersion [142], categorical univariate scatterplots were made [143]. In these, there is only one variable, which was divided into discrete groups (categories). Hence, all the points which belonged to a specific category were along with its corresponding axis, and its position would vary based on the values they owned [144].

Then, boxplots were plotted for each parameter in each condition and group, for each ROI, in order to more easily understand how the values of each parameter in these circumstances were dispersed and if and how they were skewed, to consequently compare the distributions of their values.

4.3.2.5 Statistical Analyses of the HRF Parameters

Assuming that the test samples were randomly selected from the two populations and that, for each parameter, the values of the same parameter in the same condition but in different groups per ROI were independent, it was intended to ascertain whether there were differences between the two groups (CNT and T2DM) in each condition for each ROI, and how statistically significant they were [145]. To do so, first, it was required to carry out a decision-maker test in order to understand whether the sets of values of each HRF parameter in the two study groups were normally distributed or not, and hence choose to implement a two-sample parametric or non-parametric test, respectively. Thus, a Shapiro-Wilk test was performed in each set of values from each parameter regarding each condition and group, for each ROI [146]. One opted to implement this test instead of the Kolmogorov-Smirnov test because it owns greater statistical power for the size of the analyzed samples (n = 64 and n = 77) [147].

In each condition, if the null hypothesis of the Shapiro-Wilk test was not rejected in a set of values regarding the same parameter in both groups within a 95% confidence range, then their normality assumption was validated, and a two-sample t-test would be later performed. If the null hypothesis was rejected, which implied that the data did not verify the mentioned assumption, then a Wilcoxon rank-sum test would be performed.

Bearing in mind that, in these analyzes, several statistical tests were simultaneously carried out on parameters which were not entirely independent, such as HRF peak latency and HRF relative slope to peak (see Equation 4.6), the multiple comparisons problem was again faced. This problem was corrected in all parameters but not at a ROIs' level, as it was expected that the results would reflect effect replications. The same assumption was considered for the two studied stimulation conditions (Threshold and Submaximum). However, as a less restrictive correction was desired, the p-value was corrected by implementing the Benjamini-Hochberg approach with a 0.1 false discovery rate (FDR) (equation 4.7) instead of the Bonferroni correction method, as seen in the subsection 4.3.1.

$$Benjamini\text{-}Hochberg\ adjusted\ p\text{-}value\ = p\text{-}value_{raw} \times \frac{m}{i} \tag{4.7}$$

With:

m: total number of tested hypothesis (6)

i: rank of the p-value (from 1 to 6)

4.3.2.6 Average and Median values of the HRF Parameters

In order to better understand the dispersion of the parameters and to ease their interpretation and comparison, the average and respective standard deviation or the median and respective interquartile range of each parameter, in each condition and group per ROI, were calculated according to the results obtained in the Shapiro-Wilk test. When the null hypothesis was rejected by a set of values of a parameter, and therefore they were not normally distributed, their median and corresponding interquartile range were calculated. On the other hand, when the null hypothesis was not rejected, that is, when the values of a parameter were normally distributed, their average and corresponding standard deviation were calculated.

4.3.2.7 Grand Average and Grand Median analysis

Finally, as a supplementary analysis, in each set of signal change ROIs (positive or negative), the average of all the average HRF curves, as well as the average and standard deviation of the HRF parameters extracted from each average HRF curve in each ROI for each group and condition were calculated. Likewise, the same calculations were made with the median and, consequently, the interquartile range.

5

Results

5.1 Coefficient of Variation

5.1.1 HRF peak amplitude

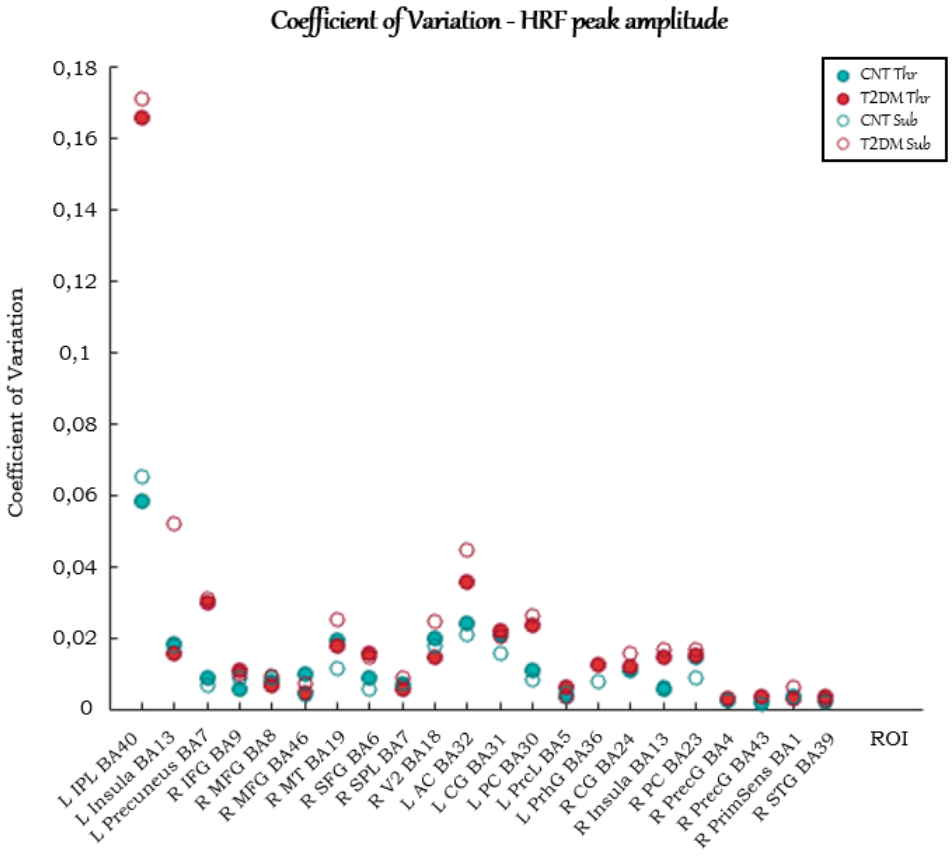

Figure 5.1: CV of the HRF peak amplitude per group and condition, in each ROI.

In figure 5.1, given the values in which the CV scoped (0 to 0.18), it was noticed that the HRF peak amplitudes presented a reduced variability in both groups and conditions. However, in both positive and negative signal change ROIs, it was found that the CV's absolute values were commonly higher in T2DM participants, which indicated a higher inconsistency in the HRF peak amplitude. Exceptions included R MFG BA8 - in both conditions; R MFG BA46, L PrcL BA5, R CG BA24 - Threshold condition; L Insula BA13, R MT BA19, R SPL BA7, R V2

BA18, L PrhG BA36 e R PC BA23 - Submaximum condition.

Furthermore, in both conditions of the positive signal change ROIs, it was seen that L IPL BA40 owned the highest CV amplitude differences between groups, as well as the highest and most dispersed absolute values of the CV - which indicated a higher peak amplitude variability in this ROI. Besides, in the negative signal change ROIs, it was found that the highest amplitude differences between groups took place in L PC BA30 (Threshold condition) and L AC BA32 (Submaximum condition).

5.1.2 HRF peak latency

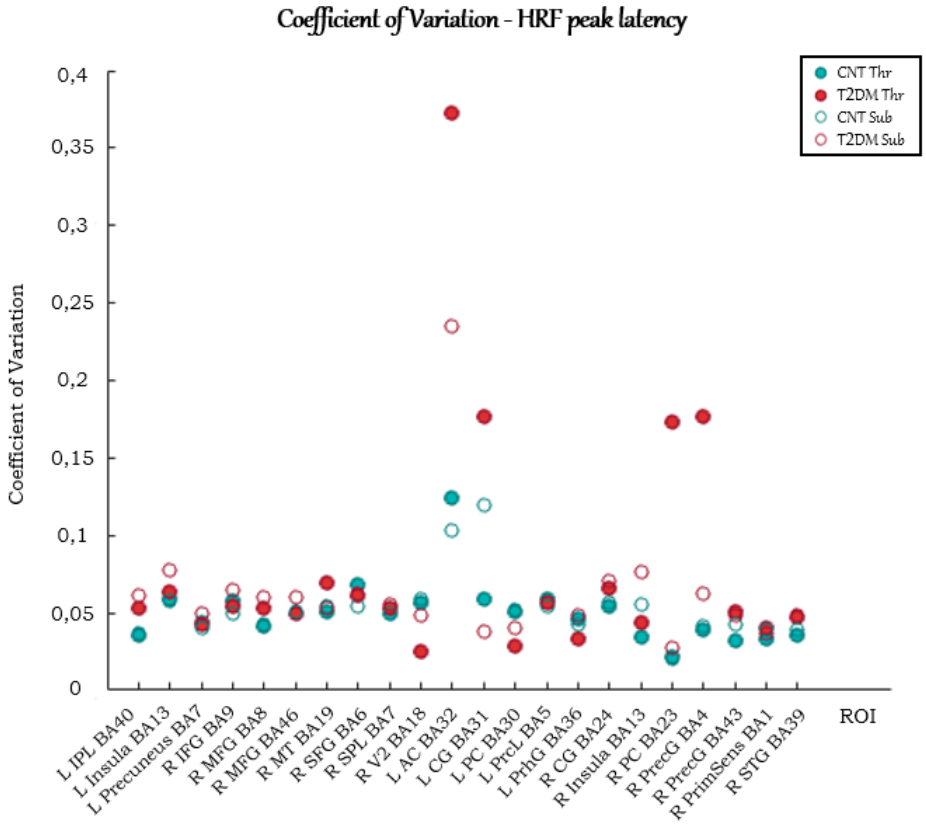

Figure 5.2: CV of the HRF peak latency per group and condition, in each ROI.

In figure 5.2, it was found that the distribution of the values was a bit less uniform than that seen in the peak amplitude (figure 5.1). Additionally, considering again the values in which the CV ranged (0 to 0.4), it was noticed that the HRF peak latencies presented a reduced variability in both groups and conditions. However, similarly to what was previously mentioned, overall, in both conditions of both signal change ROIs, the absolute values of the CV were higher in T2DM participants, also demonstrating a higher inconsistency of the peak latency in these subjects. Nevertheless, some exceptions were observed in MT BA19 and L PC BA30 - in both conditions; in L IPL BA40, L Insula BA13, R MFG BA8, R SPL BA7, L PrcL BA5, and L PrhG BA36 - Threshold condition; and in R V2 BA18, L PC BA30, and R PrimSens BA1 - Submaximum condition.

In the positive signal change ROIs, the highest amplitude differences between groups in the CV were discernible in R V2 BA18 (Threshold condition) and L IPL BA40 (Submaximum condition). In the negative signal change ROIs, these arose in L AC BA32, L CG BA31, R PC BA23, and R PrecG BA4 - Threshold condition; and in L AC BA32 and L CG BA31 - Submaximum condition.

Moreover, when comparing positive and negative signal change ROIs, the latter owned a less trivial interpretation since large CV variations, nor large absolute value dispersions were noticed, excluding two cases (L AC BA32 and L CG BA31).

5.2 Average HRFs

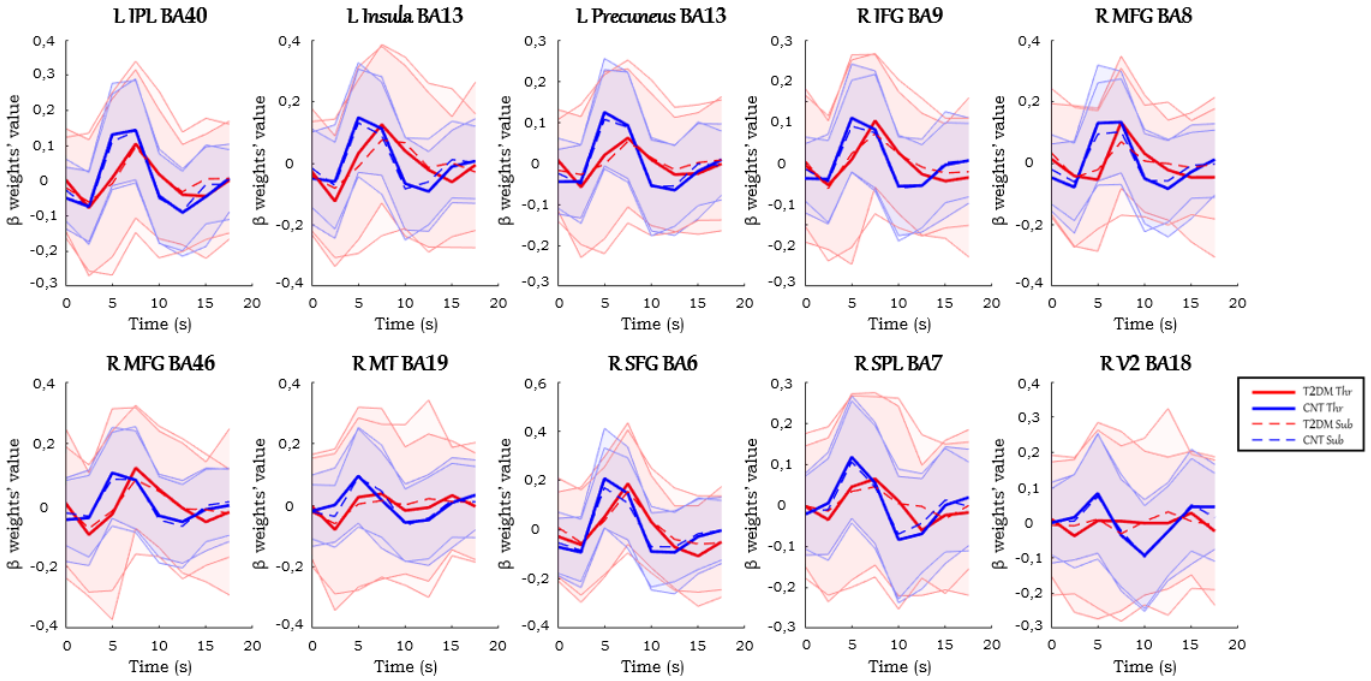

Figure 5.3: Average HRFs: positive signal change ROIs.

From figure 5.3, it was seen that, overall, in both conditions, the HRF shapes were relatively similar in each group in all ROIs, except for two of them - R MT BA19 and R V2 BA18. It was also found that the HRF shape in the controls was usually more resembling the canon, unlike the HRF of the T2DM participants. The latter was more sluggish and depicted a more substantial standard deviation, which denoted a higher variability. Additionally, the amplitude variation of the HRF was roughly the same in all ROIs, mainly in the controls.

Besides, in both conditions of the HRFs of the controls and T2DM participants, a peak was mostly noticed at 5 s and 7.5 s, respectively, except in three ROIs - L IPL BA40, R MFG BA8, and R V2 BA18. It should also be noted that when the HRF peak was compared between the two groups, there was a *biphasic variation* effect seen in the controls. First, a quick rise took place, then followed by a slower rise or fall, which was later succeeded by a rapid drop towards the baseline. Furthermore, in all ROIs, in both conditions, the PCSA was higher in the controls.

Overall, the same trend was seen in the peak amplitude and in the NCSA, whose exception was found in R MFG BA46, as well as in the relative slope to peak, whose exception was in the R V2 BA18. Most ROIs also confirmed the same premise regarding the AUC, although with a larger exception number (R MFG BA46, R MT BA19, and R SFG BA6 – both conditions; L Insula BA13 - Threshold condition).

Moreover, an initial dip was always noticeable on the HRFs of the patients with T2DM (in both conditions) and controls (in the Submaximum condition). Yet, there were some occasions where it was also seen in controls in the Threshold condition, as in L IPL BA40, L Insula BA13, R MFG BA8, and R SFG BA6. The initial dip was often more intense in the HRF of T2DM participants, and it commonly took place at 2.5 s, except in R MFG BA8 (T2DM participants in the Threshold condition), where it lasted 5 s. Besides, an undershoot in the HRFs of both groups and conditions was generally noticed, except in R V2 BA18 (T2DM participants). Comparing the HRF of both groups, the undershoot of the controls' HRF was more intense, in both conditions, with an onset of around 10 to 12.5 s and length roughly between 4 and 8 s. In the HRF of T2DM participants, the undershoot had its onset between 10 and 15 s. Bearing in mind the examined time window, in some ROIs, it was not possible to quantify the length of the undershoot in these subjects. Nevertheless, it could be stated that the return of the HRF to the baseline was, in some cases (R IFG BA9, R MFG BA8, R SPL BA7), slower than in controls, lasting between 5 to more than 8.5 s. Usually, the length was longer when there was a bigger delay between the peaks of the HRFs of controls and T2DM participants.

By analyzing figure A.1 and comparing it with figure 5.3, it was noticed that there was an attenuation of the HRF amplitude in both conditions and groups. It was found that only some ROIs, and not in all groups and/or conditions, exhibited an HRF with a relatively similar shape to those contemplated in figure 5.3: L PC BA30, L PrcL BA5, R CG BA24, R PrecG BA4, R PrecG BA43, R PrimSens BA1, and R STG BA39. It was also observed, as in figure 5.3, a more significant standard deviation in the HRFs of the T2DM participants, again demonstrating a higher variability of these curves.

Overall, given the inconsistency and randomness of the HRFs per ROIs, it was difficult to grasp a global trend in the HRF peak amplitude, peak latency, relative slope to peak and PCSA, and in the HRF's amplitude variation, undershoot, and initial dip. However, it was possible to refine a broad trend regarding AUC and NCSA, which were higher in the HRFs of the T2DM participants and controls, respectively. In the ROIs which exhibited HRFs more similar to those seen in figure 5.3, a peak latency between 7.5 and 10 s was observed in both conditions of the HRFs of controls and T2DM participants, respectively. In these ROIs, the peak amplitude, relative slope to peak, and PCSA were also considerably higher in the controls' HRFs.

In this restricted set of ROIs, the initial dip was observed between 5 and 7.5 s in the HRF of the T2DM participants. The undershoot on the controls' HRF was more intense, with an onset between 10 and 12.5 s and a length between 6 to 8.5 s. On the other hand, when it was witnessed in the HRF of the T2DM participants, its onset was between 12.5 and 15 s. For the same aforementioned reason, it could only be said that the undershoot lasted between 7.5 and

more than 10 s. However, it was not possible to understand in which group the HRF's return to the baseline was longer.

Furthermore, in figure 5.3, it was found that several HRFs of both conditions and groups started slightly deviated from zero. However, some exceptions were detected in both groups in ROI R V2 BA18 (in both conditions), and in the HRFs of T2DM participants in L IPL BA40 and L Precuneus BA7 (Threshold condition); R SFG BA6 (Submaximum condition); R IFG BA9, and R MFG BA46 (both conditions). In figure A.1, the same remark was made, except in the controls' HRFs in L PC BA30, L PrcL BA5, L PrhG BA36, R CG BA24, R PC BA23, R PrecG BA4, R PrimSens BA1, and R STG BA9 (in both conditions); and in the HRFs of the T2DM participants in L PrhG BA36, R PC BA23 and R STG BA39 (Submaximum condition). Additionally, in figure A.1, in some HRFs of patients with T2DM and controls in the Threshold condition (ROIs L AC BA32, R PrecG BA4, R PrimSens BA1, R PC BA23; L CG BA31, correspondingly), relative or absolute maximum values transpired at the first instant.

It is important to emphasize that some inconsistencies were found when the results gathered in figures 5.3 and A.1, in particular regarding the peak amplitude and relative slope to peak, were compared with those in the tables 5.2 and A.2. A possible explanation for these inconsistencies is addressed later on in chapter 6. Concerning the HRF peak amplitude, only in L PrhG BA36, R Insula BA13, and R STG BA39 (both conditions); R IFG BA9, R MFG BA46, R SFG BA6, R CG BA24, and R PrecG BA4 (Threshold condition); and R PrimSens BA1 (Submaximum condition) did not confirm this feature. In the HRF relative slope to peak, this result was seen in L Precuneus BA7, R IFG BA9, R MFG BA8, R SPL BA7, L AC BA32, R Insula BA13, R PrecG BA43, and R PrimSens BA1 (both conditions); L CG BA31, L PrhG BA36 and R STG BA39 (Submaximum condition).

5.3 Median HRFs

In figure 5.4, several trends similar to those described in figure 5.3 were found, although there were some exceptions, which I will explain. In the first place, each HRF curve had its interquartile range, which was higher on the HRFs of the T2DM participants. Then, even though several initial dips were also noticeable, its regularity was smaller. They generally appeared on the HRFs of the T2DM participants in both conditions, except in R IFG BA9, R SFG BA6, R SPL BA7, and R V2 BA18. On the other hand, sometimes they were also found on the controls' HRFs, except in L Insula BA13, R IFG BA9, R MT BA19, and R SPL BA7, with a higher prevalence in the Submaximum condition. Finally, another difference concerning figure 5.3 was related with the onset and length of the undershoots witnessed on the HRFs of both groups. In the controls, the undershoot lasted between 3.5 and 7 s and had its onset between 10 and 12.5 s; in T2DM participants, the undershoot transpired between 12.5 and 15 s. However, as in figure A.1, in some ROIs (R IFG BA9, R MFG BA8, R SFG BA9), the undershoot's length of the T2DM participants' HRFs in the Threshold condition was not able to be quantified. Therefore, it could only be stated that, again, due to the same aforementioned reason, the HRF's return to baseline in these cases was slower than in controls, lasting between 3 to more than 8.5 s.

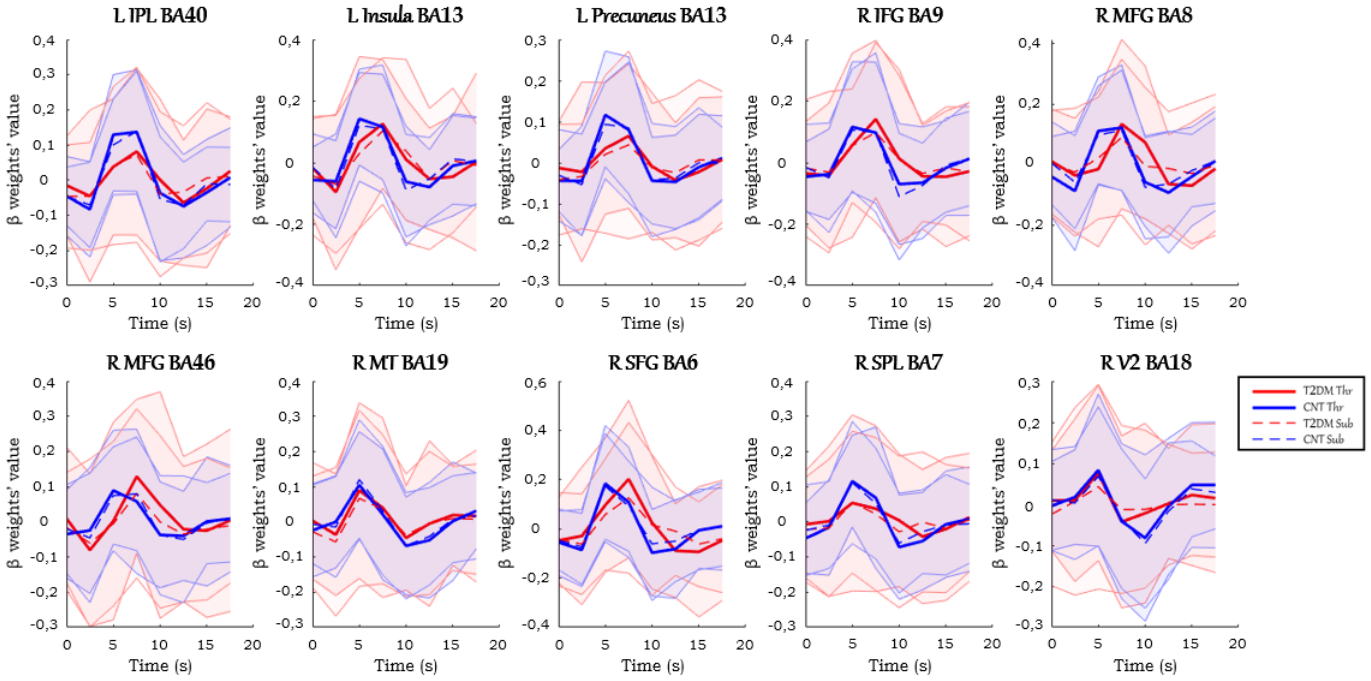

Figure 5.4: Median HRFs: positive signal change ROIs.

Likewise, similarities with figure A.1 were found in figure 5.4. However, there were again some differences, which I will now explain. First, given that this figure contained a set of median HRF curves as in figure A.2, it was detected the interquartile range of the HRF, which was higher on the HRFs of T2DM participants. Then, it was also harder to develop an overall trend for the same HRF parameters and segments mentioned during the analysis of figure A.1, due to the same reason. Although NCSA was also included in this set, the initial dip and PCSA were excluded, with PCSA increasing in the controls. On the other hand, the initial dip was commonly found on the HRFs of the T2DM participants, although it was observed once at 2.5 s in L PrhG BA36, on the controls' HRF in the Submaximum condition. Its onset was perceived between 2.5 and 7.5 s, although it also transpired at 7.5 s. Furthermore, in the same set of ROIs whose HRF shape was similar to those seen in figure 5.3, overall, and in both conditions, the peak latency transpired roughly between 5 and 7.5 s and between 2.5 and 10 s, on the HRFs of the controls and T2DM participants, correspondingly. Finally, in these ROIs, the onset and length of the HRF undershoot in each group varied. The onset was equal in both groups, taking place between 7.5 and 12.5 s. However, its length was roughly 6.5 to more than 10 s and 5 to more than 6.5 s in controls and T2DM participants, respectively. Once again, due to the same reason already manifested, it was not possible to quantify the complete length of these undershoots nor to understand in which group the HRF's return to the baseline was larger.

Again, the same observation regarding deviations from zero in the first instants of the HRFs in figures 5.4 and A.2 was made, but in different ROIs. In figure 5.4, this feature was not found in R MFG BA8 and R MT BA19 (both conditions), and R MFG BA46 (Threshold condition), on the HRFs of the T2DM participants; and in R MFG BA8 (Submaximum condition) and R V2 BA18 (Threshold condition), on the HRFs of the controls. In figure A.2, this feature was not

detected in L PrhG BA36, R Insula BA13, and R PrimSens BA1 (Submaximum condition); R PrecG BA43 (Threshold condition) on the HRFs of the controls. Moreover, it was also seen in CG BA24, R Insula BA13, R PrecG BA43 and R PrimSens BA1 (both conditions); L CG BA31, L AC BA32, L PrhG BA36, R PrecG BA4 and R STG BA9 (Threshold condition); and in L PC BA30 and R PC BA23 (Submaximum condition), on the HRFs of T2DM participants. Figure A.2 also showed the same note regarding relative or absolute maximums at the first instant. However, it only happened on the HRFs of T2DM participants in the Threshold condition in the following ROIs: L AC BA32, R PrecG BA4, and R PrecG BA43.

Furthermore, as in figures 5.3 and A.1, some inconsistencies were found when the results displayed in figures 5.4 and A.2, in particular regarding the HRF peak amplitude and relative slope to peak, were compared with those in the tables 5.2 and A.2. In the HRF peak amplitude, only L CG BA31, L PrhG BA36, and R STG BA39 (both conditions); R IFG BA9, R MFG BA46, R SFG BA6, R PC BA23, and R PrecG BA4 (Threshold condition); and R CG BA24 (Submaximum condition) did not exhibit this feature. In the HRF relative slope to peak, this feature was seen in L Precuneus BA7, R IFG BA9, R MFG BA8, R SPL BA7, L AC BA32, L PC BA30, L PrcL BA5, R CG BA24, and R PrecG BA43 (both conditions); R PC BA23 and R STG BA39 (Threshold condition); and in L IPL BA40 and L PrhG BA36 (Submaximum condition).

5.4 Grand Analysis

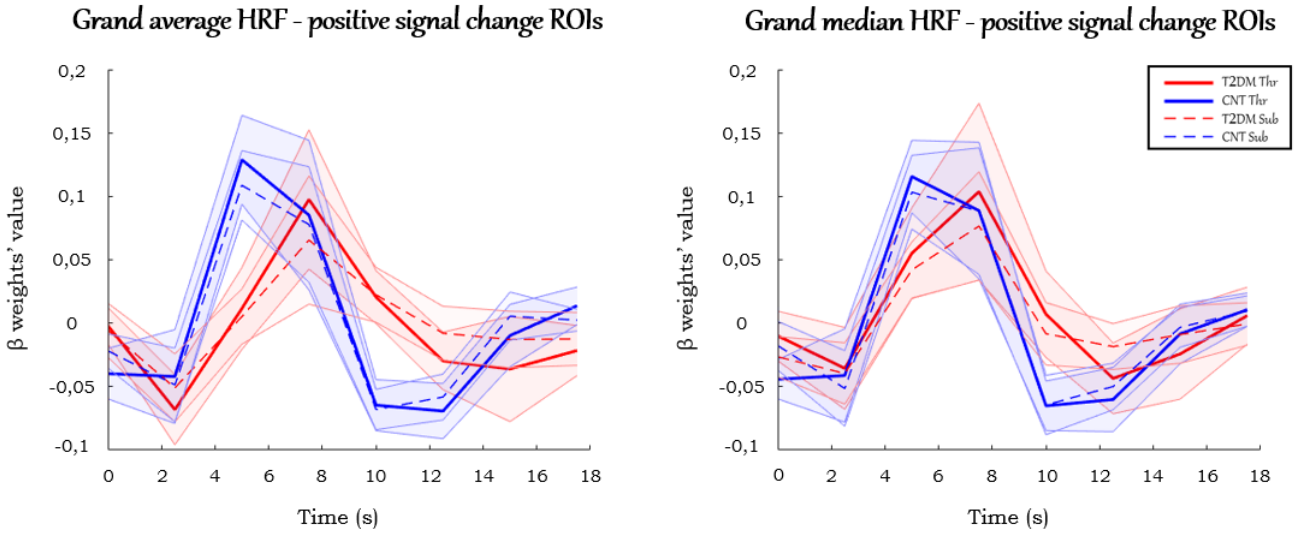

(a) Grand average HRFs.

(b) Grand median HRFs.

Figure 5.5: Grand average and grand median HRFs: positive signal change ROIs.

Table 5.1: Grand Analysis' statistical component - positive signal change ROIs.

		CNT		T2DM	
		Average ± Standard Deviation	*Median ± Interquartile Range*	*Average ± Standard Deviation*	*Median ± Interquartile Range*
HRF peak amplitude (beta weights)	**Threshold**	0,130 ± 0,035	0,116 ± 0,032	0,100 ± 0,051	0,107 ± 0,059
	Submaximum	0,113 ± 0,029	0,113 ± 0,028	0,072 ± 0,039	0,077 ± 0,043
HRF peak latency (s)	**Threshold**	8,000 ± 1,054	7,5 ± 0	10,750 ± 2,372	10,0 ± 2,5
	Submaximum	8,000 ± 1,054	7,5 ± 2,5	11,000 ± 2,108	10,0 ± 2,5
HRF relative slope to peak (beta weights/s)	**Threshold**	0,021 ± 0,020	0,007 ± 0,005	0,010 ± 0,006	0,012 ± 0,005
	Submaximum	0,017 ± 0,005	0,017 ± 0,007	0,008 ± 0,004	0,011 ± 0,004
HRF AUC (a.u.)	**Threshold**	1,413 ± 0,253	1,366 ± 0,278	1,297 ± 0,450	1,040 ± 0,655
	Submaximum	1,340 ± 0,218	1,306 ± 0,426	1,007 ± 0,354	0,761 ± 0,387
HRF PCSA (a.u.)	**Threshold**	0,492 ± 0,127	0,437 ± 0,162	0,324 ± 0,155	0,378 ± 0,198
	Submaximum	0,413 ± 0,090	0,391 ± 0,112	0,254 ± 0,127	0,237 ± 0,210
HRF NCSA (a.u.)	**Threshold**	0,454 ± 0,130	0,401 ± 0,210	0,364 ± 0,156	0,293 ± 0,249
	Submaximum	0,394 ± 0,088	0,370 ± 0,156	0,223 ± 0,101	0,225 ± 0,153

5.4.1 Grand Average

Based on figure 5.5a, and similarly to the results depicted in figures 5.3 and 5.4, an evident difference on the HRF shape of the two sets of curves was visible. Comparing the two sets of HRFs, the HRFs of the controls, again, were more resembling with the HRF canon shape and showed a peak latency around 5 s, as well as an undershoot with onset at 10 or 12.5 s, in the Submaximum or Threshold condition, respectively, lasting approximately 4 s. In addition, the HRFs of the T2DM participants were more sluggish and, overall, when they were compared with the controls' curves, depicted relatively less amplitude variation and a peak latency delayed 2.5 s. The peak latency in these curves occurred around 7.5 s, and the undershoot had an onset around 15 s. However, due to the same reason mentioned in figures 5.3 and 5.4, once again the duration of the undershoot was not able to be quantified, and it could only be said that the HRF's return to the baseline was slower in T2DM participants, lasting between 5 to more than 6.5 s. Finally, an initial dip at 2.5 s was also verified in all HRF curves, except for the controls in the Threshold condition. Moreover, the initial dip was more pronounced in T2DM participants.

Furthermore, there were no inconsistencies between the statistical and graphical components of this analysis. Thus, in both conditions, it was found that the HRF peak amplitude, the relative slope to peak, AUC, PCSA, and NCSA were higher in controls, while the HRF peak latency was higher in T2DM participants. By analyzing figure 5.5a, it was found that the standard deviation was relatively similar between groups and higher at the HRF's beginning (including in the initial dip), peak, and minimum (in the undershoot). In the statistical component, AUC, PCSA, and NCSA were the only HRF parameters to have a higher standard deviation in controls.

Based on figure A.3a, and similarly to the results obtained in figures A.1 and A.2, there were quite marked differences between the HRFs of each group and condition when they were compared with its corresponding ones in figure 5.5a. On the other hand, similarities were seen in some aspects. The HRF shape of the two sets of curves corresponding to each group also depicted a noticeable difference. Moreover, although not so evident, due to the reduced amplitude of the beta weights, when the two sets of HRFs were compared, the HRFs of the controls were fairly more similar to the HRF canon shape. The HRF of the controls showed a peak latency at 5 s or 7.5 s (Threshold or Submaximum condition, respectively), as well as an undershoot with an onset around 12.5 s, lasting approximately 8 or more than 9.5 s (Threshold or Submaximum

condition, respectively). As in figure 5.5a, a small initial dip was also perceived at 2.5 s, but only in the controls' HRFs in the Submaximum condition. Moreover, in both conditions, the HRFs of the T2DM participants were also more sluggish, even more than in figure 5.5a. Besides, they generally had a higher amplitude variation and exhibited an initial dip at around 5 s in both conditions. Additionally, on the HRFs of T2DM participants, the peak latency took place at 12.5 s and 10 s, in the Threshold and Submaximum conditions, respectively. The undershoot is non-existent in the Threshold condition since, after the peak onset, the HRF reaches the baseline without crossing it even once. However, in the Submaximum condition, even though it was barely noticeable, the undershoot loomed at 12.5 s, with a length of 5.5 s. Finally, it was found that the HRF peak amplitude was higher in controls and T2DM participants in the Threshold and Submaximum conditions, correspondingly.

Nevertheless, comparing the two components of this analysis, inconsistent results could be observed. Due to the singularity of the HRFs, it could only be stated that, in both conditions, the HRF peak amplitude, peak latency, AUC, and NCSA were higher in T2DM participants, whereas the PCSA was higher in controls. In the Submaximum condition, the relative slope to peak was higher in T2DM participants. However, in the Threshold condition, the opposite takes place due to the initial maximum on the HRF of T2DM participants. In the statistical component (table 5.1), it was found that all the previously mentioned parameters, as well as the PCSA, were higher in T2DM participants. Contrarily, it was found that, in the Submaximum condition, the peak latency was higher in T2DM participants. However, in the Threshold condition, the absolute value of this parameter was equal. Additionally, in the Threshold condition, the relative slope to peak was higher in controls, and, in the Submaximum condition, the opposite happened. Besides, the standard deviation of the HRFs was slightly higher in the negative signal change ROIs and somewhat similar between groups, increasing at the same segments stated in figure 5.5a, as well as in the peak rise. Statistically, in both conditions, only PCSA and NCSA exhibited a higher standard deviation in controls and T2DM participants, respectively. In the Submaximum condition, the HRF peak amplitude, relative slope to peak, and AUC were higher in T2DM participants, transpiring the opposite in the Threshold condition. However, the peak latency manifested a higher standard deviation in controls in the Submaximum condition and was, therefore, higher in T2DM participants in the Threshold condition.

Again, in figures 5.5a and A.3a, the same note regarding the deviations from zero at the first instants of the HRFs was made. In figure 5.5a, this feature was observed on the controls' HRF. In figure A.3a, it was discerned on the controls' HRF in the Submaximum condition and on the T2DM participants' HRF in the Threshold condition. Figure A.3a also shows the same note regarding the relative or absolute maximums at the first instant, but only on the T2DM participants' HRF in the Threshold condition.

5.4.2 Grand Median

In figure 5.5b, numerous similarities with figure 5.5a were detected, so I will only mention the differences between them. Although the initial dip was located on the same HRFs and at the same time (2.5 s) as in figure 5.5a, it was more intense in controls in the Submaximum

condition. On the other hand, small differences concerning the undershoot perceived in figure 5.5a were also observed. On the controls' HRFs, the undershoot had an onset at 10 s, lasting 4 and 4.5 s in the Submaximum and Threshold conditions, respectively. On the opposite, on the T2DM participants' HRFs, the undershoot was only seen in the Threshold condition, with an onset of 12 s and a length of 4 s.

There were also no inconsistencies between the statistical and graphical components of this analysis. In figure 5.5b, the interquartile range was higher in the same segments discerned in figure 5.5a. However, in the statistical component, in both conditions, only the peak amplitude and PCSA exhibited a higher interquartile range in patients with T2DM. The HRF relative slope to peak, the AUC, and NCSA presented higher values in T2DM participants in the Threshold condition and in controls in the Submaximum condition. On the other hand, the HRF peak latency was higher in the Threshold condition in T2DM participants. However, in the Submaximum condition, it had the same absolute value in both groups.

In figure A.3b, some similarities with what was seen in figure A.3a were also contemplated. Therefore, I am only going to highlight the differences. The initial dip was only noticed on the controls' HRFs. As for peak latencies, in the Submaximum condition, these occurred at the same time as its corresponding curves in figure A.3a; in the Threshold condition, the HRF peaks of T2DM participants and controls transpired at 7.5 s. It is important to stress that the HRF beginning in T2DM participants in the Submaximum condition transpired at a local minimum, after which there was a slight rise at 2.5 s, followed by the initial dip (at 5 s). On the other hand, the undershoot was unexistent in both conditions in T2DM participants since the HRFs returned to the baseline just after the peak onset. On the controls' HRFs, it was found that the onset of the undershoot took place at the same time point as in figure A.3a (12.5 s), and its length was approximately 6 s in both conditions.

Just as in the grand average analysis, inconsistent results between the two components of this analysis were also found. In figure A.3b, it was found that, in both conditions, the HRF peak amplitude peak, AUC, and NCSA were higher in T2DM participants, and that the relative slope to peak was higher in controls. On the other hand, PCSA was bigger in T2DM participants in the Threshold condition and smaller in the Submaximum condition. In the HRF peak latency, it was noted the opposite, also due to an initial maximum on the HRFs of the T2DM participants. Statistically, it was found that, in both conditions, the HRF peak amplitude and NCSA were higher in controls and T2DM participants, respectively. However, in the Threshold condition, both the AUC and PCSA were higher in T2DM participants, and the relative slope to peak was higher in controls. The opposite pattern was noticed in the Submaximum condition. Statistically, in both conditions, the HRF peak latency, AUC, and NCSA showed a higher interquartile range in T2DM participants, with the opposite taking place in the relative slope to peak and PCSA. Yet, the peak amplitude was higher in controls in the Threshold condition and higher in T2DM participants in the Submaximum condition.

Again, in figures 5.5b and A.3b, the same observation regarding the deviations from zero in the first moments of the HRFs was made. In figure 5.5b, all HRFs of both conditions witnessed

deviations from zero at the first instants. In figure A.3b, the same feature was always seen except on the controls' HRF in the Threshold condition. Also, in figure A.3b, on the T2DM participants' HRF in the Threshold condition, relative or absolute maximums at the first instant were seen.

5.5 Group Statistics

In each ROI, after all the parameters of each condition and group underwent the Shapiro-Wilk test, it was found that, of the 528 parameters tested, only 10 did not reject the null hypothesis, and therefore had a normal distribution. Of these ten, only two belonged to negative signal change ROIs, and they both concerned PCSA, in the same condition, but in different groups and ROIs (R PrecG BA43 PCSA CNT Threshold and R PrimSens BA1 PCSA T2DM Threshold). The remaining eight, from the positive signal change ROIs, concerned the HRF parameters in controls such as peak amplitude and NCSA in both conditions (R IFG BA9 peak amplitude CNT Threshold / Submaximum, R SPL BA7 peak amplitude CNT Threshold / Submaximum and R SPL BA7 NCSA CNT Threshold / Submaximum) and AUC in different conditions (L IPL BA40 AUC CNT Submaximum and R SPL BA7 AUC CNT Threshold).

It was never seen that, in an ROI, the same parameter owned a normal distribution in both groups simultaneously. Thus, one of the t-Student test's assumptions was revoked, and therefore, this test was never implemented. Consequently, the Wilcoxon rank-sum test was always implemented, and a p-value adjustment according to the approach mentioned in 4.3.2.5 was made. According to the results of this test, in the positive signal change ROIs, overall, it was found that the relative slope to peak and peak latency in the Threshold condition had slight differences between the two groups. In the negative signal change ROIs, the same results were overall found in the peak amplitude in the Threshold condition, in the NCSA in the Submaximum condition, and in the peak latency and relative slope to peak in both conditions.

Table 5.2: Shapiro-Wilk test's p-values ($\alpha = 0.05$) and the median and interquartile range of each HRF parameter of each condition per ROI - Positive signal change ROIs.

		HRF peak amplitude (beta weights)				**HRF peak latency (s)**			
		Threshold		**Submaximum**		**Threshold**		**Submaximum**	
		CNT	**T2DM**	**CNT**	**T2DM**	**CNT**	**T2DM**	**CNT**	**T2DM**
L IPL BA40	**p-value**	2,260E-06	2,569E-05	7,447E-04	3,612E-07	2,182E-08	3,731E-06	4,668E-07	1,072E-04
	Median ± Interquartile Range	0,183 ± 0,094	0,218 ± 0,187	0,167 ± 0,155	0,236 ± 0,211	5 ± 10	6,25 ± 10	5,0 ± 7,5	7,5 ± 5
L Insula BA13	**p-value**	1,346E-07	8,280E-09	6,605E-08	1,167E-05	2,544E-08	6,271E-05	4,906E-09	1,076E-04
	Median ± Interquartile Range	0,178 ± 0,167	0,195 ± 0,187	0,169 ± 0,131	0,198 ± 0,201	5,0 ± 7,5	10,0 ± 7,5	5,0 ± 7,5	7,5 ± 7,5
L Precuneus BA7	**p-value**	0,002	0,001	0,001	1,079E-04	4,630E-08	1,519E-05	2,015E-07	2,123E-06
	Median ± Interquartile Range	0,172 ± 0,162	0,266 ± 0,274	0,193 ± 0,152	0,241 ± 0,233	5 ± 10	7,5 ± 7,5	5,0 ± 7,5	5 ± 5
R IFG BA9	**p-value**	0,107	5,656E-06	0,060	2,778E-08	4,770E-09	2,932E-05	2,121E-09	1,364E-04
	Median ± Interquartile Range	0,161 ± 0,074*	0,227 ± 0,194	0,149 ± 0,065*	0,222 ± 0,218	5,000 ± 8,125	7,50 ± 6,25	5 ± 10	7,5 ± 7,5
R MFG BA8	**p-value**	6,413E-09	5,728E-07	4,230E-08	9,998E-09	2,167E-09	6,357E-06	1,387E-08	9,947E-05
	Median ± Interquartile Range	0,198 ± 0,136	0,192 ± 0,226	0,179 ± 0,142	0,180 ± 0,222	5 ± 10	5,0 ± 7,5	5,000 ± 5,625	7,5 ± 5
R MFG BA46	**p-value**	3,178E-08	1,947E-04	3,429E-06	1,297E-08	2,777E-08	2,794E-05	5,131E-08	7,848E-05
	Median ± Interquartile Range	0,174 ± 0,130	0,232 ± 0,240	0,179 ± 0,135	0,227 ± 0,221	5,0 ± 7,5	7,5 ± 7,5	5,0 ± 7,5	7,5 ± 7,5
R MT BA9	**p-value**	3,224E-08	1,664E-06	2,336E-07	2,678E-08	1,732E-08	1,791E-05	1,075E-08	2,652E-05
	Median ± Interquartile Range	0,181 ± 0,138	0,203 ± 0,223	0,207 ± 0,115	0,222 ± 0,246	5 ± 10	7,5 ± 7,5	5 ± 10	7,5 ± 7,5
R SFG BA6	**p-value**	2,274E-08	4,481E-04	4,523E-06	2,864E-08	2,478E-07	7,703E-05	1,310E-07	2,168E-05
	Median ± Interquartile Range	0,207 ± 0,196	0,243 ± 0,169	0,222 ± 0,171	0,204 ± 0,182	5,0 ± 7,5	7,50 ± 6,25	5 ± 10	7,5 ± 5
R SPL BA7	**p-value**	0,057	2,246E-11	0,445	4,785E-11	1,089E-04	3,724E-05	1,976E-05	3,058E-04
	Median ± Interquartile Range	0,173 ± 0,076*	0,243 ± 0,233	0,171 ± 0,077*	0,236 ± 0,231	7,5 ± 7,5	7,5 ± 7,5	7,5 ± 7,5	7,5 ± 5
R V2 BA18	**p-value**	7,928E-09	4,553E-08	4,364E-05	8,409E-10	3,186E-09	2,270E-04	1,312E-09	4,732E-04
	Median ± Interquartile Range	0,160 ± 0,126	0,177 ± 0,184	0,173 ± 0,178	0,206 ± 0,198	5,000 ± 5,625	10,0 ± 7,5	5 ± 5	7,5 ± 7,5

		HRF relative slope to peak (beta weights/s)				HRF AUC (a.u.)			
		Threshold		Submaximum		Threshold		Submaximum	
		CNT	T2DM	CNT	T2DM	CNT	T2DM	CNT	T2DM
L IPL BA40	**p-value**	1,788E-09	5,558E-05	7,076E-10	0,003	3,035E-05	2,333E-08	0,501	1,187E-06
	Median ± Interquartile Range	0,032 ± 0,072	0,030 ± 0,069	0,023 ± 0,048	0,039 ± 0,072	2,872 ± 1,698	4,590 ± 4,740	3,034 ± 1,169*	4,532 ± 4,525
L Insula BA13	**p-value**	2,544E-08	6,271E-05	4,906E-09	1,076E-04	7,839E-07	1,319E-07	2,775E-07	6,008E-06
	Median ± Interquartile Range	0,026 ± 0,090	0,016 ± 0,038	0,032 ± 0,054	0,021 ± 0,057	2,646 ± 2,060	3,708 ± 3,475	2,376 ± 2,233	3,801 ± 2,874
L Precuneus BA7	**p-value**	1,236E-09	8,815E-05	1,133E-09	0,015	1,428E-06	9,667E-05	2,333E-04	2,528E-07
	Median ± Interquartile Range	0,029 ± 0,049	0,038 ± 0,095	0,026 ± 0,043	0,050 ± 0,094	2,921 ± 2,896	4,233 ± 3,939	3,338 ± 3,737	4,335 ± 6,175
R IFG BA9	**p-value**	2,331E-04	5,018E-06	9,685E-06	2,841E-07	1,166E-05	2,846E-10	2,603E-05	9,762E-10
	Median ± Interquartile Range	0,028 ± 0,048	0,034 ± 0,059	0,021 ± 0,050	0,029 ± 0,051	2,460 ± 1,209	3,912 ± 3,385	2,462 ± 1,425	3,994 ± 2,715
R MFG BA8	**p-value**	1,384E-06	2,234E-03	1,919E-03	4,035E-06	1,148E-06	2,940E-07	2,059E-08	2,804E-09
	Median ± Interquartile Range	0,035 ± 0,084	0,038 ± 0,061	0,057 ± 0,077	0,024 ± 0,045	3,162 ± 2,516	3,889 ± 4,061	3,427 ± 2,120	3,475 ± 3,665
R MFG BA46	**p-value**	6,898E-09	4,998E-07	1,072E-07	2,041E-12	5,907E-07	1,107E-10	3,751E-05	3,071E-09
	Median ± Interquartile Range	0,036 ± 0,068	0,031 ± 0,065	0,036 ± 0,068	0,022 ± 0,056	3,168 ± 1,814	3,888 ± 3,296	3,219 ± 2,394	4,430 ± 3,746
R MT BA9	**p-value**	1,515E-05	4,577E-08	2,567E-06	2,652E-07	1,736E-07	2,109E-08	4,409E-06	1,331E-06
	Median ± Interquartile Range	0,043 ± 0,094	0,030 ± 0,058	0,044 ± 0,086	0,025 ± 0,065	3,114 ± 2,187	3,697 ± 3,191	3,370 ± 2,277	3,887 ± 3,708
R SFG BA6	**p-value**	1,791E-04	5,679E-13	5,175E-06	2,182E-09	1,231E-06	1,121E-08	3,564E-11	9,205E-07
	Median ± Interquartile Range	0,047 ± 0,074	0,034 ± 0,060	0,032 ± 0,053	0,032 ± 0,051	4,183 ± 2,826	4,149 ± 3,339	3,866 ± 3,371	4,348 ± 3,784
R SPL BA7	**p-value**	4,495E-08	4,776E-06	2,004E-07	2,776E-15	0,062	9,936E-14	4,142E-05	1,768E-12
	Median ± Interquartile Range	0,025 ± 0,034	0,032 ± 0,058	0,022 ± 0,031	0,042 ± 0,060	3,124 ± 1,185*	4,097 ± 3,951	2,809 ± 2,639	4,247 ± 3,290
R V2 BA18	**p-value**	1,899E-10	4,436E-05	1,310E-09	5,139E-11	4,466E-09	5,107E-10	3,377E-07	4,798E-10
	Median ± Interquartile Range	0,033 ± 0,061	0,026 ± 0,061	0,046 ± 0,066	0,034 ± 0,048	3,096 ± 2,069	3,620 ± 3,085	3,709 ± 2,697	3,687 ± 2,716

		HRF PCSA (a.u.)				HRF NCSA (a.u.)			
		Threshold		Submaximum		Threshold		Submaximum	
		CNT	T2DM	CNT	T2DM	CNT	T2DM	CNT	T2DM
L IPL BA40	**p-value**	7,878E-07	3,341E-07	0,024	9,016E-06	3,055E-05	2,636E-06	0,001	1,542E-10
	Median ± Interquartile Range	0,756 ± 0,646	1,050 ± 0,929	0,642 ± 0,530	1,200 ± 0,851	0,705 ± 0,525	0,898 ± 0,976	0,753 ± 0,516	1,011 ± 0,763
L Insula BA13	**p-value**	1,527E-06	1,086E-07	1,569E-05	1,029E-06	1,247E-08	1,104E-08	7,493E-09	1,222E-09
	Median ± Interquartile Range	0,668 ± 0,573	0,845 ± 0,784	0,668 ± 0,563	0,936 ± 0,913	0,656 ± 0,615	1,020 ± 0,838	0,574 ± 0,484	0,875 ± 0,910
L Precuneus BA7	**p-value**	1,323E-04	1,065E-03	1,069E-03	2,031E-05	5,576E-05	8,432E-05	1,498E-05	2,327E-06
	Median ± Interquartile Range	0,742 ± 0,626	1,226 ± 1,257	0,788 ± 0,772	1,081 ± 1,144	0,799 ± 0,699	1,052 ± 1,135	0,883 ± 0,981	0,958 ± 0,849
R IFG BA9	**p-value**	0,020	5,890E-07	0,014	5,685E-07	7,608E-04	1,352E-08	8,437E-03	1,411E-09
	Median ± Interquartile Range	0,659 ± 0,425	0,951 ± 0,804	0,650 ± 0,452	1,031 ± 0,828	0,632 ± 0,463	0,975 ± 1,213	0,620 ± 0,312	0,999 ± 0,919
R MFG BA8	**p-value**	3,232E-08	4,097E-07	1,371E-09	1,635E-08	1,004E-05	4,724E-07	8,913E-09	9,083E-09
	Median ± Interquartile Range	0,860 ± 0,556	0,968 ± 0,990	0,784 ± 0,573	0,919 ± 1,089	0,739 ± 0,496	0,827 ± 0,873	0,765 ± 0,441	0,803 ± 0,672
R MFG BA46	**p-value**	1,479E-06	4,128E-08	1,989E-04	1,416E-07	5,620E-08	1,506E-09	0,002	1,426E-09
	Median ± Interquartile Range	0,782 ± 0,577	0,916 ± 0,693	0,836 ± 0,607	1,040 ± 0,989	0,744 ± 0,552	0,988 ± 0,944	0,805 ± 0,494	1,028 ± 0,967
R MT BA9	**p-value**	2,959E-06	1,518E-06	2,254E-08	3,715E-08	8,653E-08	6,683E-07	2,352E-07	1,314E-06
	Median ± Interquartile Range	0,804 ± 0,674	1,014 ± 0,936	0,912 ± 0,512	0,983 ± 0,913	0,799 ± 0,612	0,834 ± 1,006	0,906 ± 0,458	0,904 ± 0,982
R SFG BA6	**p-value**	7,378E-05	2,900E-05	2,457E-07	2,696E-05	1,308E-06	2,931E-07	1,307E-07	1,179E-07
	Median ± Interquartile Range	0,896 ± 0,864	1,026 ± 0,829	0,895 ± 0,792	1,008 ± 0,864	0,961 ± 0,677	1,028 ± 0,890	0,872 ± 0,768	0,930 ± 0,926
R SPL BA7	**p-value**	0,027	1,191E-12	4,819E-04	2,493E-12	0,056	5,681E-12	0,334	4,029E-12
	Median ± Interquartile Range	0,723 ± 0,403	1,058 ± 1,299	0,710 ± 0,552	1,040 ± 0,865	0,739 ± 0,362*	0,992 ± 0,854	0,813 ± 0,374*	0,998 ± 0,926
R V2 BA18	**p-value**	2,325E-06	3,324E-09	1,537E-05	1,383E-09	1,715E-07	2,395E-09	1,578E-10	8,612E-10
	Median ± Interquartile Range	0,792 ± 0,646	0,883 ± 0,639	0,803 ± 0,861	0,893 ± 0,909	0,777 ± 0,689	0,938 ± 0,803	0,861 ± 0,724	0,935 ± 0,612

Key: * - represents the average and standard-deviation of the HRF parameters which did not reject the null hypothesis of the Shapiro-Wilk test, and therefore owned a normal distribution.

Table 5.3: Wilcoxon rank-sum test's adjusted p-values (FDR = 0.10) in each HRF parameter of each condition per ROI - Positive signal change ROIs.

		HRF peak amplitude (beta weights)		HRF peak latency (s)	
		Threshold	Submaximum	Threshold	Submaximum
L IPL BA40	**Adjusted p-value (FDR = 0,10)**	0,068	0,001	0,833	0,631
L Insula BA13	**Adjusted p-value (FDR = 0,10)**	0,180	0,096	0,001	0,018
L Precuneus BA7	**Adjusted p-value (FDR = 0,10)**	0,001	0,033	0,509	0,665
R IFG BA9	**Adjusted p-value (FDR = 0,10)**	0,001	3,673E-05	0,421	0,025
R MFG BA8	**Adjusted p-value (FDR = 0,10)**	0,532	0,827	0,472	0,022
R MFG BA46	**Adjusted p-value (FDR = 0,10)**	0,038	0,086	0,042	0,003
R MT BA19	**Adjusted p-value (FDR = 0,10)**	0,485	0,827	0,188	0,494
R SFG BA6	**Adjusted p-value (FDR = 0,10)**	0,666	2,005	0,340	1,107
R SPL BA7	**Adjusted p-value (FDR = 0,10)**	4,327E-04	0,001	0,995	0,218
R V2 BA18	**Adjusted p-value (FDR = 0,10)**	0,225	0,241	1,863E-04	2,559E-04

		HRF relative slope to peak (beta weights/s)		HRF AUC (a.u.)	
		Threshold	Submaximum	Threshold	Submaximum
L IPL BA40	**Adjusted p-value (FDR = 0,10)**	0,854	0,025	0,001	3,712E-05
L Insula BA13	**Adjusted p-value (FDR = 0,10)**	0,020	0,190	0,005	1,508E-04
L Precuneus BA7	**Adjusted p-value (FDR = 0,10)**	0,455	0,064	0,002	0,011
R IFG BA9	**Adjusted p-value (FDR = 0,10)**	0,408	0,447	7,670E-07	8,208E-07
R MFG BA8	**Adjusted p-value (FDR = 0,10)**	0,424	0,033	0,557	0,837
R MFG BA46	**Adjusted p-value (FDR = 0,10)**	0,472	0,062	0,017	0,009
R MT BA19	**Adjusted p-value (FDR = 0,10)**	0,861	0,720	0,230	0,799
R SFG BA6	**Adjusted p-value (FDR = 0,10)**	0,103	3,298	0,692	1,434
R SPL BA7	**Adjusted p-value (FDR = 0,10)**	0,313	0,006	0,007	0,002
R V2 BA18	**Adjusted p-value (FDR = 0,10)**	0,755	0,646	0,190	0,624

		HRF PCSA (a.u.)		HRF NCSA (a.u.)	
		Threshold	Submaximum	Threshold	Submaximum
L IPL BA40	**Adjusted p-value (FDR = 0,10)**	0,001	7,167E-07	0,076	0,001
L Insula BA13	**Adjusted p-value (FDR = 0,10)**	0,095	0,008	0,004	2,126E-04
L Precuneus BA7	**Adjusted p-value (FDR = 0,10)**	0,001	0,034	0,012	0,086
R IFG BA9	**Adjusted p-value (FDR = 0,10)**	0,001	3,315E-05	1,606E-04	2,169E-05
R MFG BA8	**Adjusted p-value (FDR = 0,10)**	0,846	0,576	0,558	0,793
R MFG BA46	**Adjusted p-value (FDR = 0,10)**	0,046	0,042	0,018	0,005
R MT BA19	**Adjusted p-value (FDR = 0,10)**	0,508	1,265	0,773	0,953
R SFG BA6	**Adjusted p-value (FDR = 0,10)**	0,693	0,917	0,910	0,809
R SPL BA7	**Adjusted p-value (FDR = 0,10)**	0,008	0,001	0,005	0,012
R V2 BA18	**Adjusted p-value (FDR = 0,10)**	0,617	0,971	0,149	0,751

5.6 Boxplots

In the positive signal change ROIs, it was found that, overall, in both conditions, the median (average*) relative slope to peak was higher in controls. On the opposite, the remaining HRF parameters (peak amplitude, peak latency, AUC, PCSA, and NCSA) were higher in T2DM participants. Besides, it was found that, mainly in both conditions, the interquartile ranges (standard deviation*) of the HRF peak amplitude, AUC, PCSA, and NCSA were higher in T2DM participants. On the other hand, the interquartile range of the peak latency was higher in controls. Furthermore, although the interquartile range of the relative slope to peak in the Threshold condition was overall higher in controls, in the Submaximum condition, this parameter did not exhibit an overall trend. That is, the relative slope to peak was higher in controls the same amount of times as in T2DM participants.

It was also seen that the dispersion of absolute values was always higher in the peak latency and shorter in the peak amplitude and relative slope to peak, in all conditions and groups. It was found that, generally, the parameters per group and condition followed an asymmetric distribution and were positively skewed, that is, their average was bigger than their median. It should also be noted that some of the HRF parameters with a normal distribution according to the Shapiro-Wilk test as R SPL BA7 AUC CNT Threshold and R IFG BA9 peak amplitude CNT Submaximum showed a slight asymmetry on the boxplot.

In the negative signal change ROIs, the same overall trend concerning the median values in the positive signal change ROIs was observed. Furthermore, the notes regarding the interquartile range in the peak amplitude, relative slope to peak, AUC, PCSA, and NCSA in both conditions, and the peak latency in the Threshold condition were overall in agreement with its corresponding ones in the positive signal change ROIs. However, it was found that the interquartile range in

the peak latency in the Submaximum condition was the same between the two groups.

The same trends regarding the dispersion of values and the distribution symmetry seen in the positive signal change ROIs were noticed. Also, in the positive signal change ROIs, some HRF parameters with a normal distribution according to the Shapiro-Wilk test, such as R PrimSens BA1 PCSA T2DM Threshold and R PrecG BA43 PCSA CNT Threshold showed a slight asymmetry on the boxplot.

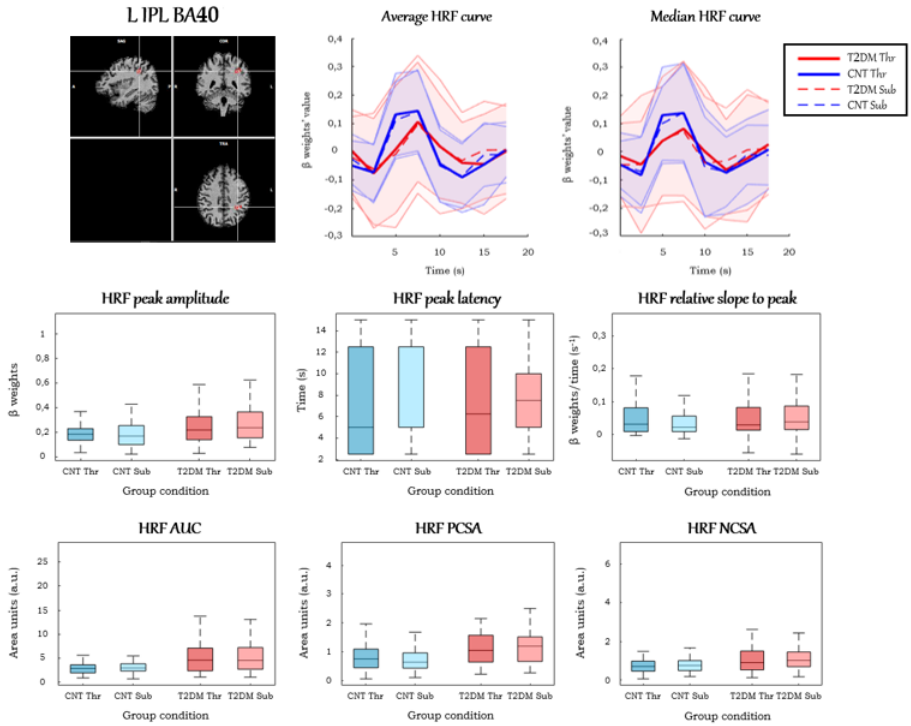

Figure 5.6: Average and median HRFs and HRF parameters: L IPL BA40.

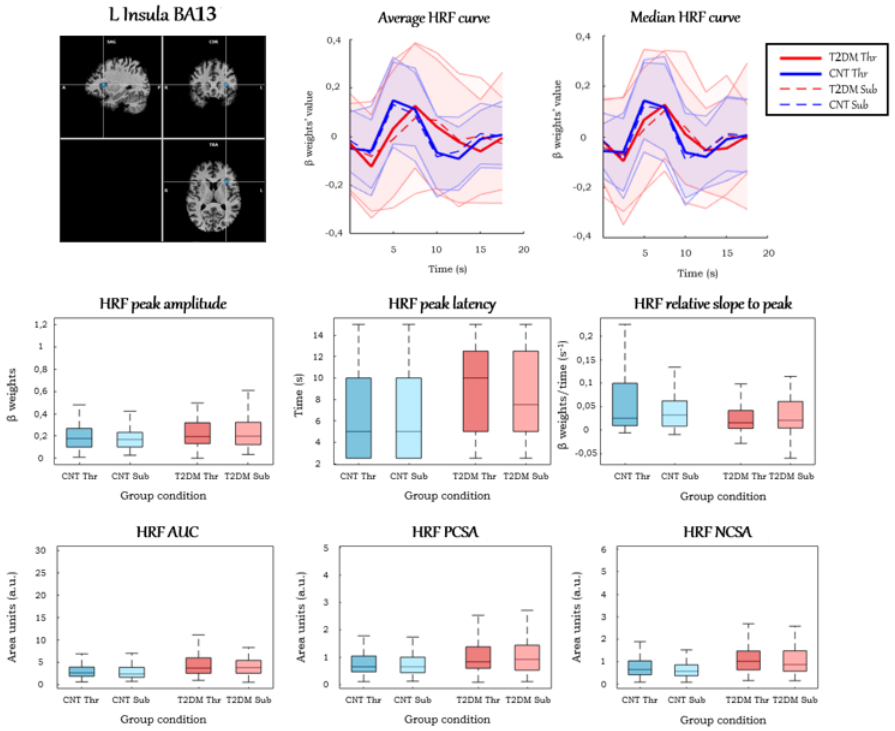

Figure 5.7: Average and median HRFs and HRF parameters: L Insula BA13.

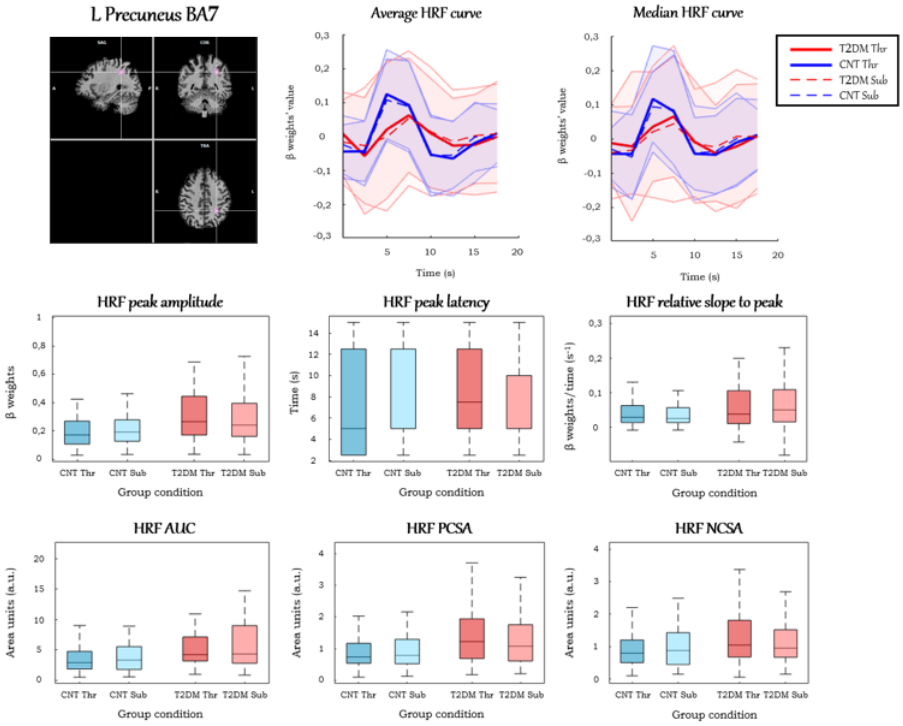

Figure 5.8: Average and median HRFs and HRF parameters: L Precuneus BA7.

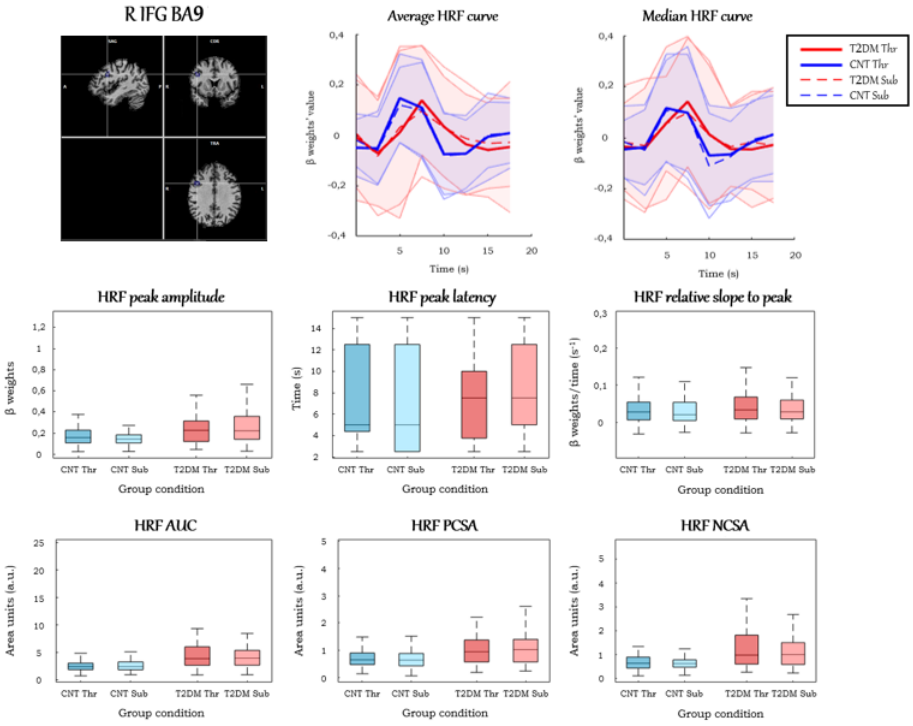

Figure 5.9: Average and median HRFs and HRF parameters: R IFG BA9.

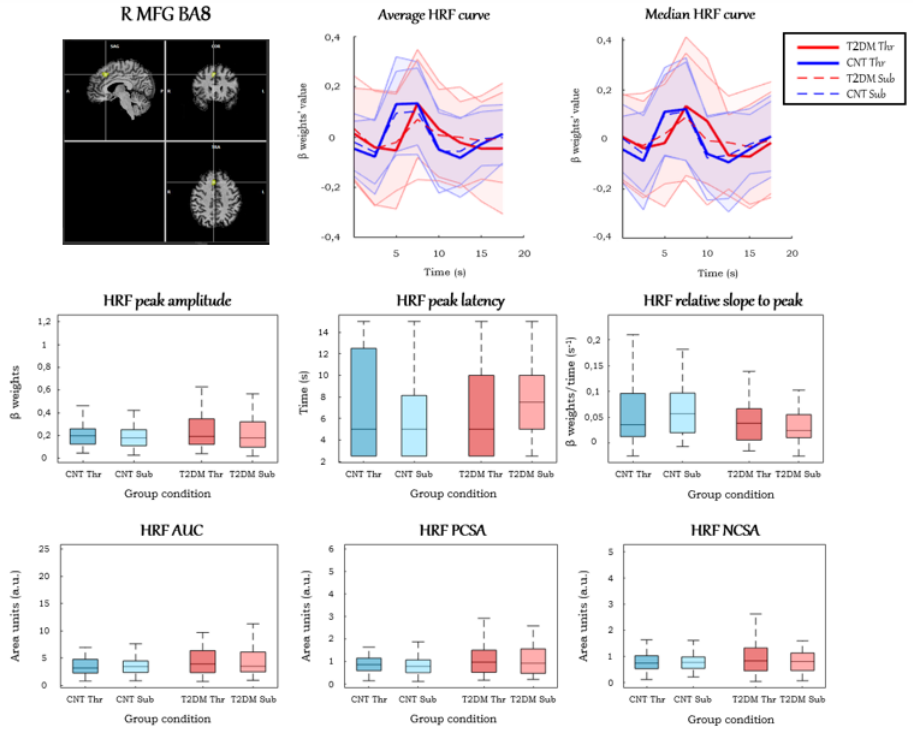

Figure 5.10: Average and median HRFs and HRF parameters: R MFG BA8.

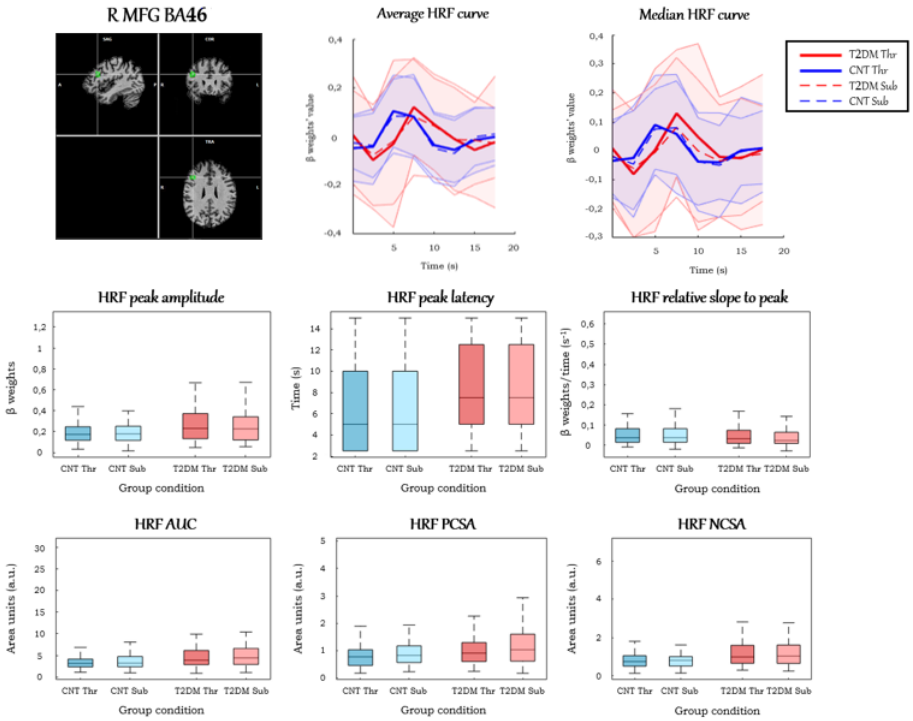

Figure 5.11: Average and median HRFs and HRF parameters: R MFG BA46.

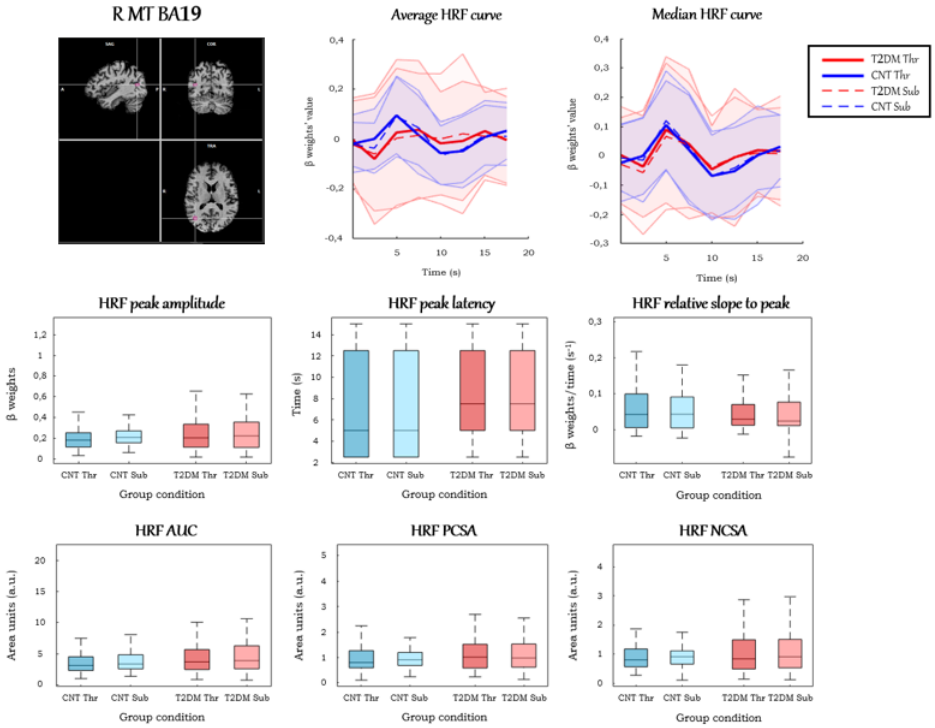

Figure 5.12: Average and median HRFs and HRF parameters: R MT BA19.

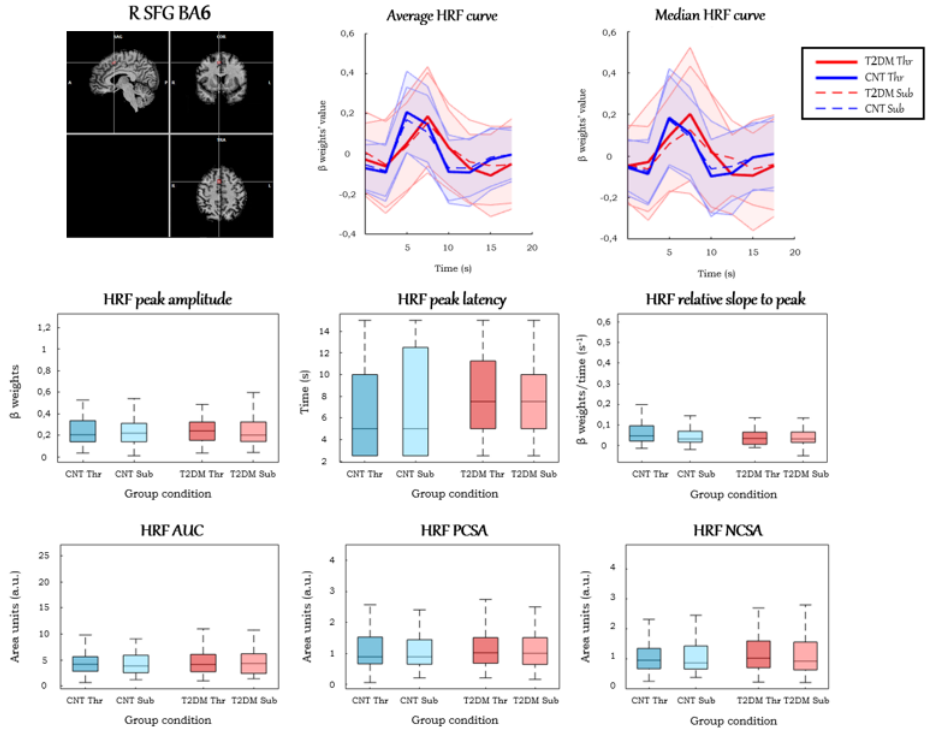

Figure 5.13: Average and median HRFs and HRF parameters: R SFG BA6.

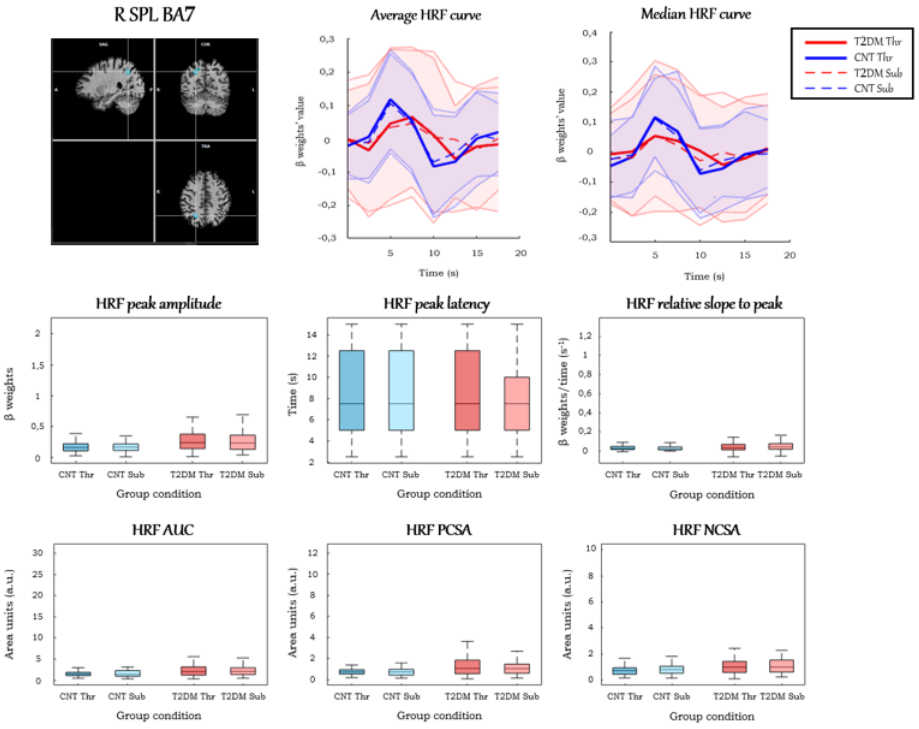

Figure 5.14: Average and median HRFs and HRF parameters: R SPL BA7.

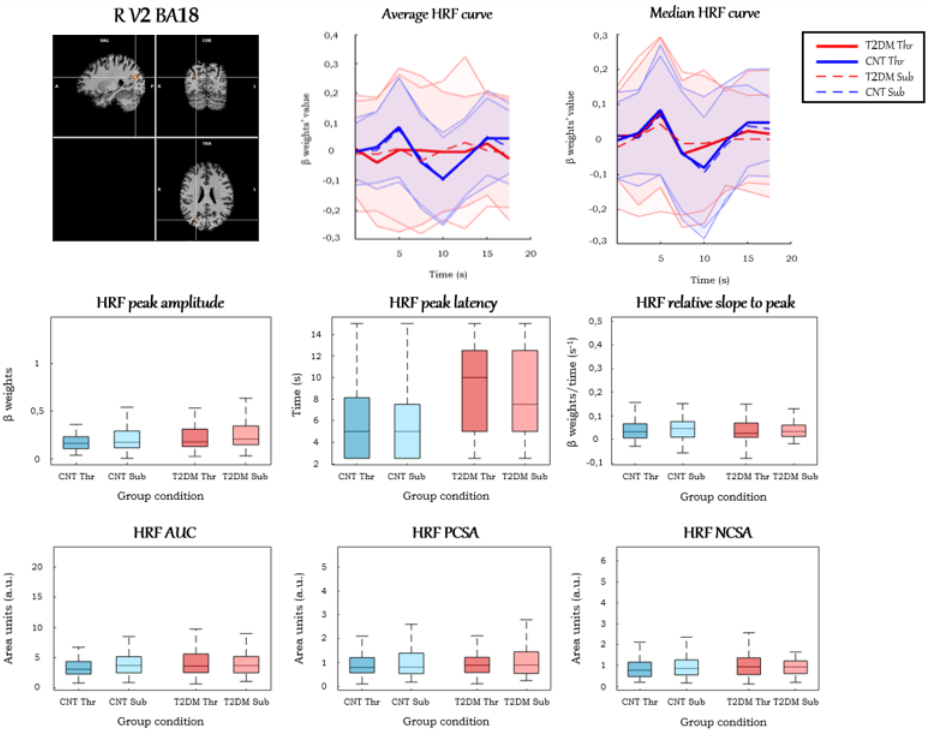

Figure 5.15: Average and median HRFs and HRF parameters: R V2 BA18.

5.7 Univariate Scatterplots

In the positive signal change ROIs (figures A.16 to A.37), it was found that almost all HRF parameters depicted higher absolute values and dispersion in T2DM participants, except for the HRF peak latency and relative slope to peak. The absolute values of the former did not exhibit any widespread trend between groups, although they manifested higher dispersion in controls. On the other hand, the absolute values of the latter, even though they presented higher dispersion in T2DM participants, they were higher in controls.

In reverse, in the negative signal change ROIs, the same trend was perceived even in parameters that did not validate this premise in the positive signal change ROIs. However, in this case, although the dispersion of the HRF peak latency data was higher in controls, its absolute values were higher in T2DM participants. Furthermore, although the absolute values of the HRF relative slope to peak were also higher in controls, its data dispersion did not show an overall trend.

6

Discussion

This study found that the HRF and, consequently, its parameters and morphology differed between groups and were profoundly altered in T2DM. Overall, in all ROIs, T2DM participants presented a more sluggish (time delayed) HRF - diverging from the canonical HRF - with a higher peak latency and an absent or a less intense, but lengthier undershoot (final deactivation), with a higher onset. Besides, their HRFs exhibited smaller peak amplitude and relative slope to peak. Although AUC, PCSA, and NCSA appear to be relatively similar between the two populations, they tended to be smaller in T2DM participants. Furthermore, the inter-HRF and inter-parameter variabilities were, on average, also higher in T2DM participants. Lastly, the HRFs of T2DM participants often included an initial dip (the classic initial reduction due to the mismatch between oxygen consumption and blood supply) - unlike what happens in controls - whose intensity did not have a general trend.

It is suggested that the underlying reason for the witnessed changes in the HRFs of T2DM participants may be compromised neurovascular coupling. Possible explanations for this outcome could include vascular damage (such as endothelial dysfunction), impairment of the vasodilation regulatory mechanisms, or limited O_2 transport. It is not likely that intrinsic neuronal activity alterations could have a significant effect on these curves because, as mentioned, during the task, the stimuli were individually-fitted so that the task difficulty was similar for all subjects. Furthermore, the task performance was identical between groups, revealing parallel perceptual discrimination ability. That is, regardless of the potential cell damage in T2DM participants, the neurons in the stimuli-activated regions theoretically will have the same integrity types between the two groups.

In T2DM participants, there is an imbalance between the relative O_2 consumption and blood supply. In fact, even if there were the same O_2 use under stimulation and neuronal activation conditions in both groups, due to the NVC changes, the oxygenated blood supply becomes smaller and thus, the O_2 decrease induced by neuronal activity will not be so swiftly offset - which justifies the overall HRF delay found. Consequently, the deoxyhemoglobin concentration will increase, hence decreasing the BOLD signal, which explains the initial dip seen in its average and median HRFs, and most often absent or less perceptible in the controls. When the blood supply finally starts to balance the O_2 consumption, the BOLD signal increases, but more gradually and slower than usual until the peak is reached - which elucidates, in turn, the higher peak latency and smaller amplitude peak and relative slope to peak overall seen in the average

and median HRFs of T2DM participants. On the opposite, the controls, with a more efficient NVC, will own a higher and faster BOLD signal increase, producing a higher peak amplitude, relative slope to peak, AUC, PCSA, and NCSA, but a lower peak latency, which matches with the overall results. It should also be noted that the *biphasic variation* effect witnessed at the HRF peak of the controls may be justified, on the other hand, by a mere curve artifact, considering its temporal resolution (2.5 s), and not as a physiological effect of the hemodynamic response. In T2DM participants, after reaching the peak, the return to the baseline, due to the aforementioned reasons, will have delays and will be slower than in controls, which is mainly in line with the achieved results. On the other hand, the undershoot may not be discerned, which may be due to a masking effect prompted by the lower efficiency of the first phase of the hemodynamic response.

Moreover, the components of the NVC own intraindividual, inter-region, and inter-condition variability [57], which it is required to be characterized in order to understand how the hemodynamic response is governed. In particular, T2DM does not affect each individual equivalently. The hemodynamic response, in fact, displayed a large inter-subject variability in T2DM, which is consistent with the damage differences in NVC, and will overall increase the HRF variability in T2DM participants. Conversely, the controls, as they overall own a more efficient NVC, and considering that the studied sample of individuals belongs to a specific age group (40-76 years old), then, the hemodynamic response will be more similar between them and will show less variability.

Furthermore, the results also demonstrate a predominant HRF replication effect between ROIs and between the type of stimuli. In other words, the HRFs are not significantly different between ROIs and between the type of stimuli. This consistency effect between ROIs and conditions suggest an overall effect of T2DM on the HRF which is similar between regions and conditions.

However, there were some limitations to this study. First, the HRFs of the negative signal change ROIs displayed less amplitude variation than the analogs in the positive signal change ROIs. Besides, they presented atypical responses, with distinct randomness and variability, so they did not always resemble the HRFs shown in the aforementioned ROIs, which made it difficult to obtain an overall trend for the several HRF parameters in all ROIs. Their values differed significantly between themselves and, in many cases, deviated from the values and trends previously described in the positive signal change ROIs, which is why a less thorough analysis of the remaining results was not performed as in the positive signal change ROIs. It should also be noted that only a few ROIs owned vague similarities to the positive signal change ROIs, but not in all conditions or groups (L PC BA30, L PrcL BA5, R CG BA24, R PrecG BA4, R PrecG BA43, R PrimSens BA1, and R STG BA39). It is based on these and on other results that it becomes crucial to justify the reason underlying the designation of these ROIs as negative signal change ROIs instead of *deactivation regions*. Furthermore, the HRFs of these ROIs were distinct from the classic deactivation, which was similar to those existing in the positive signal change ROIs, yet inverted. That is, there would be a large signal decrease against the baseline,

a peak (which would correspond to the minimum of the function) around 4-6 seconds, and a return to the baseline at 16-20 seconds. Similarly to the canonical HRF, there could also be an initial dip (positive) before the peak [148]. Overall, the HRF baseline of the T2DM participants in the Threshold condition was slightly greater than zero (no higher than 0.07), and the signal lowered (no lower than -0.07). Although it seems a small value at all, it turns out to be a high drop against the baseline, and it can be captured as a deactivation by the statistical model. However, by carefully observing these curves, it turns out that it may well not be it, given that the remaining HRFs in the same ROIs did not follow the same pattern. Therefore, what was witnessed in the HRFs of the T2DM participants in the Threshold condition can also be explained by a noise effect in the baseline or by a relatively normal activation with an initial dip, followed by a weakened rise, resulting in a relatively reduced slope to peak and peak amplitude - potentially a consequence of compromised NVC. As the term *deactivation* is commonly associated with a physiological meaning - a region which decreases its activity during a condition - and as the meaning of the HRFs of these ROIs is not understood, which is another reason why a more detailed analysis was not performed, it was considered wiser to designate them as *negative signal change* ROIs. In order to maintain the coherence, the remaining ROIs, in which the discussion was focused, were designated as *positive signal change* ROIs even though they resemble the typical *activation* ROIs.

Secondly, in each ROI, there were some discrepancies when the trends between the average/median parameters of the average/median HRFs from all subjects and the average/median of the individual HRF parameters were compared, possibly from higher outlier probability on T2DM due to higher variability. These were due to an *average of all subjects vs. average of the individual values* effect, which reveals a lesser value consistency over time in T2DM participants, with this effect being more sensitive to outliers. For instance, the results in figures 5.3 and 5.4 were obtained by estimating, correspondingly, the average and the median of the individual beta weights of a given group and condition at each data point for each positive signal change ROI. Analogously, the same estimate was implemented in each negative signal change ROIs in figures A.1 and A.2. However, in tables 5.2 and A.2, the average and the median of the individual HRF parameters were displayed in each group and condition for each positive and negative signal change ROIs, respectively. In order to simplify the explanation and to expand it to the remaining parameters, I will only regard the peak amplitude. When the average (median) of the peak amplitude of the individual HRFs is calculated, regardless of its occurrence, we will obtain a greater average (median) peak amplitude, since individually it is less likely to suppress the variability effect when outliers exist. However, in the average (median) HRFs, as the average (median) of each data point is calculated, the peak can be attenuated, given its variability per subject. Yet, if the peak befalls in more participants at a given datapoint, the value of the peak amplitude at that datapoint will resemble more the amplitude of the average (median) peak. Thus, it is believed that T2DM participants own a higher variability concerning the datapoint where the peak looms, prompting a lower peak amplitude in the average and median HRFs, which is far from the average (median) peak amplitude, increasing the disparity between the two parameters when group and individual averages were compared. The same effect happens

again and becomes clearer when the visual interpretation of the grand average (median) and the statistical results of the global average (median) parameters were compared. In each condition and group, the grand average (median) HRF was estimated by calculating the averages (medians) of all the average (median) HRFs in each type of signal change ROIs (positive/negative). On the other hand, the parameters displayed in tables 5.1 and A.1 were estimated by calculating the average (median) of all parameters of the mean (median) HRFs in each type of signal change ROIs.

Besides, in figures 5.3 and 5.4, it was found that R MT BA19 and R V2 BA18 owned average and median HRFs that diverged from the canonical HRF shape in T2DM participants, which may be due to an inability effect to produce robust activation.

Moreover, according to the GLM model, HRFs should start presumably at zero, which cannot happen when, for instance, there is noise in the signal. This would be the suggested cause for the deviations from zero seen in the first instant of several HRFs, and, although in a more amplified way, for the relative or absolute maximums existing in those same instants, in many of the HRFs of the negative signal change ROIs.

Additionally, the slight boxplot asymmetry found in some of the HRF parameters with a normal distribution according to the Shapiro-Wilk test may be due to its p-values slightly lower than the FDR (0.10). Thus, the null hypothesis ends up not being rejected, and these parameters turn out to own a barely normal distribution.

Nevertheless, it should be also stressed a very curious remark: the existence of two sub-regions of the same brain region (L Insula BA13 and R Insula BA13) with very distinct HRFs. It would be thought that it could indicate slightly different behaviors. However, as long as the negative signal change ROIs cannot be understood, it will be a too hasty statement to utter. Thus, as there are no typical deactivations, the most likely cause should be the SNR effect, since the negative signal changes can be caused by noise in the baseline. In other words, deep down, both regions would exhibit positive signal changes, but the GLM in one of the sub-regions captured the variation against the baseline as negative.

Finally, despite the strong statistical power of these results, besides T2DM, there are several other sources of NVC changes, which in turn can introduce variability. For instance, the BOLD signal, which measures indirectly and qualitatively the NVC, is also sensitive to other hemodynamic processes even from non-pathological sources (e.g. atypical brain physiology) [57, 149]. Thus, when the NVC is investigated, its interpretation and comparison between groups become more complicated [150], requiring a more sensible result evaluation in participants with altered hemodynamics. Therefore, one way to decrease variability and, consequently, improve the results, would be diminishing variance within populations. Although in this study the age effect on NVC was considered, given that all the subjects belonged to the same age group (40-76 years), it would be a good suggestion to perform an individual preliminary analysis, assessing, for instance, the neurovascular system state or the clinical history of each subject (other co-morbidities, medications, among others).

7

Conclusion and Future Work

This project proved that patients with T2DM have a compromised hemodynamic response function in all brain regions, regardless of the displayed type of stimulus. These damages were evidenced by the distinctive HRF shape and by the differences overall noticed in its parameters, in both conditions and in all ROIs: a more sluggish (time delayed) and smaller HRF, with an initial dip and a delayed or even absent undershoot, higher peak latency, and lower peak amplitude, relative slope to peak, AUC, PCSA, and NCSA.

It is suggested that the changes discerned between groups in the HRF and its parameters are due to early neurovascular uncoupling caused by T2DM. However, since the NVC is a rather complex system, whose components change between regions and conditions, conditioning how the coupling takes place [59], it is not possible to state precisely which mechanism or component has been affected and how or to what extent. Further research should be done on this topic to understand and, in the future, potentially halt the brain functional damage progression in T2DM. A suggestion would be the implementation of other imaging techniques such as Arterial Spin Labeling (ASL) and/or Positron Emission Tomography (PET) - even though the latter owns reduced spatial resolution - in order to estimate more direct and independent measures on vascular perfusion and/or metabolism, correspondingly. However, first and foremost, it should be expanded more knowledge about the NVC, its mechanisms, and how they regulate it.

This project also validated the fMRI as a tool to evaluate the HRF in T2DM. On the one hand, by implementing a stimulation task in a neurosensory event-related paradigm and then extracting the hemodynamic response to it by a deconvolution, as suggested in Duarte et al. (2015), it was possible to evaluate the BOLD signal differences in diabetic participants and thus identify the NVC disruption which they underwent. Thus, the relevance of this approach becomes strengthened, placing it at the forefront of further functional studies in T2DM. On the other hand, the evaluated HRF parameters not only optimize and expand the neurovascular function assessment - which may prompt further studies that may involve classification and/or its use as a biomarker - but also establish themselves as local determinants of altered HRF shape, and might reveal the clinical evolution of a patient, and consequently, play a preponderant role in the T2DM therapeutics - which complements the results from Duarte et al. (2015) [12].

Bearing in mind some of the BOLD signal limitations and its repercussions when the NVC is investigated, further research is required to enlighten the physiology underlying the BOLD

signal, eventually in animal models, as well as to develop or improve hemodynamic methods that describe it and take into consideration the multiple factors which affect it [57], in order to foster its use as a method to measure neuronal activity and map brain function in T2DM.

Although the reason underlying the between-group differences regarding the undershoot and the initial dip has already been conjectured, its physiological meaning and what defines their length and/or onset are still unclear, suggesting a need for further studies concerning the pathophysiology and NVC changes in T2DM.

Funding

This work was supported by Fundação para a Ciência e Tecnologia (DoIT – Diamarker: a consortium for the discovery of novel biomarkers in diabetes – QREN- COMPETE), INFARMED Research Fund for Health (FIS-FIS-2015-01_DIA - DiaMarkData), and the European Foundation for the Study of Diabetes (EFSD) 2019 - Innovative Measurement of Diabetes Outcomes 2019.

Bibliography

[1] X. Y. Yuan and X. G. Wang, "Mild cognitive impairment in type 2 diabetes mellitus and related risk factors: A review," *Reviews in the Neurosciences*, vol. 28, no. 7, pp. 715–723, 2017. doi: 10.1515/revneuro-2017-0016.

[2] S. Chatterjee, K. Khunti, and M. J. Davies, "Type 2 diabetes," *The Lancet*, vol. 389, pp. 2239–2251, jun 2017. doi: 10.1016/S0140-6736(17)30058-2.

[3] M. Stumvoll, B. J. Goldstein, and T. W. van Haeften, "Type 2 diabetes: principles of pathogenesis and therapy," *The Lancet*, vol. 365, pp. 1333–1346, apr 2005. doi: 10.1016/S0140-6736(05)61032-X.

[4] "World Health Organization - Diabetes," 2020. Accessed on: 2020-09-16. [Online]. Available: https://www.who.int/health-topics/diabetes#tab=tab_1.

[5] M. I. McCarthy, "Genomics, Type 2 Diabetes, and Obesity," *New England Journal of Medicine*, vol. 363, pp. 2339–2350, dec 2010. doi: 10.1056/NEJMra0906948.

[6] American Diabetes Association, "Classification and Diagnosis of Diabetes," *Diabetes Care*, vol. 40, pp. S11–S24, jan 2017. doi: 10.2337/dc17-S005.

[7] American Diabetes Association, "Diagnosis and Classification of Diabetes Mellitus," *Diabetes Care*, vol. 35, pp. S64–S71, jan 2012. doi: 10.2337/dc12-s064.

[8] A. Sapra and P. Bhandari, *Diabetes Mellitus*. StatPearls Publishing, jun 2020. PMID: 10.2337/dc12-s064.

[9] A. Hussain, B. Claussen, A. Ramachandran, and R. Williams, "Prevention of type 2 diabetes: A review," *Diabetes Research and Clinical Practice*, vol. 76, pp. 317–326, jun 2007. doi: 10.1016/j.diabres.2006.09.020.

[10] A. Artasensi, A. Pedretti, G. Vistoli, and L. Fumagalli, "Type 2 Diabetes Mellitus: A Review of Multi-Target Drugs," *Molecules*, vol. 25, p. 1987, apr 2020. doi: 10.3390/molecules25081987.

[11] G. J. Biessels and Y. D. Reijmer, "Brain Changes Underlying Cognitive Dysfunction in Diabetes: What Can We Learn From MRI?," *Diabetes*, vol. 63, pp. 2244–2252, jul 2014. doi: 10.2337/db14-0348.

[12] J. V. Duarte, J. M. Pereira, B. Quendera, M. Raimundo, C. Moreno, L. Gomes, F. Carrilho, and M. Castelo-Branco, "Early Disrupted Neurovascular Coupling and Changed Event Level Hemodynamic Response Function in Type 2 Diabetes: An fMRI Study," *Journal of Cerebral Blood Flow & Metabolism*, vol. 35, pp. 1671–1680, oct 2015. doi: 10.1038/jcbfm.2015.106.

[13] D. N. Kennedy, N. Makris, M. R. Herbert, T. Takahashi, and V. S. Caviness, "Basic principles of MRI and morphometry studies of human brain development," *Developmental Science*, vol. 5, pp. 268–278, August 2002. doi: 10.1111/1467-7687.00366.

[14] A. R. Kherlopian, T. Song, Q. Duan, M. A. Neimark, M. J. Po, J. K. Gohagan, and A. F. Laine, "A review of imaging techniques for systems biology," *BMC Systems Biology*, vol. 2, no. 1, p. 74, 2008. doi: 10.1186/1752-0509-2-74.

[15] A. Berger, "How does it work?: Magnetic resonance imaging," *BMJ*, vol. 324, pp. 35–35, jan 2002. doi: 10.1136/bmj.324.7328.35.

[16] M. A. Brown and R. C. Semelka, "MR Imaging Abbreviations, Definitions, and Descriptions: A Review," *Radiology*, vol. 213, pp. 647–662, December 1999. doi: 10.1148/radiology.213.3.r99dc18647.

[17] S. Currie, N. Hoggard, I. J. Craven, M. Hadjivassiliou, and I. D. Wilkinson, "Understanding MRI: basic MR physics for physicians," *Postgraduate Medical Journal*, vol. 89, pp. 209–223, apr 2013. doi: 10.1136/postgradmedj-2012-131342.

[18] D. J. Bell and J. Jones, "Net magnetization vector," 2020. Accessed on: 2020-03-01. [Online]. Available: https://radiopaedia.org/articles/net-magnetisation-vector.

[19] W. Mangrum, Q. B. Hoang, T. J. Amrhein, S. M. Duncan, C. M. Maxfield, E. Merkle, and A. W. Song, *Duke Review of MRI Principles: Case Review Series*. Elsevier Health Sciences, 2 ed., 2019. ISBN: 978-0-323-53038-5. Accessed on: 2020-01-06.

[20] H. Devlin, "What is Functional Magnetic Resonance Imaging (fMRI)?," 2018. Accessed on: 2020-03-15. [Online]. Available: https://psychcentral.com/lib/what-is-functional-magnetic-resonance-imaging-fmri.

[21] B. R. Rosen, R. L. Buckner, and A. M. Dale, "Event-related functional MRI: Past, present, and future," *Proceedings of the National Academy of Sciences of the United States of America*, vol. 95, pp. 773–780, feb 1998. doi: 10.1073/pnas.95.3.773.

[22] J. M. Soares, R. Magalhães, P. S. Moreira, A. Sousa, E. Ganz, A. Sampaio, V. Alves, P. Marques, and N. Sousa, "A Hitchhiker's Guide to Functional Magnetic Resonance Imaging," *Frontiers in Neuroscience*, vol. 10, pp. 1–35, 2016. doi: 10.3389/fnins.2016.00515.

[23] S. Ogawa and Y.-W. Sung, "Functional magnetic resonance imaging," *Scholarpedia*, vol. 2, p. 3105, oct 2007. Accessed on: 2020-03-15. [Online]. Available: http://www.scholarpedia.org/article/Functional_magnetic_resonance_imaging.

[24] S. S. Dutta, "What is fMRI?," 2020. Accessed on: 2020-03-16. [Online]. Available: https://www.news-medical.net/health/What-is-fMRI.

[25] G. H. Glover, "Overview of Functional Magnetic Resonance Imaging," *Neurosurgery Clinics of North America*, vol. 22, no. 2, pp. 133–139, 2011. doi: 10.1016/j.nec.2010.11.001.

[26] K. Uludağ, D. J. Dubowitz, and R. B. Buxton, "Basic principles of Functional MRI," in *Clinical magnetic resonance imaging* (R. Edelman, J. Hesselink, and M. Zlatkin, eds.), ch. 9, pp. 249–287, Elsevier, 2005. ISBN: 978-9996019494. Accessed on: 2020-02-18.

[27] B. R. Buchbinder, "Functional magnetic resonance imaging," in *Handbook of Clinical Neurology*, vol. 135, pp. 61–92, Elsevier B.V., jan 2016. doi: 10.1016/B978-0-444-53485-9.00004-0.

[28] C. N. Hall, C. Howarth, Z. Kurth-Nelson, and A. Mishra, "Interpreting BOLD: towards a dialogue between cognitive and cellular neuroscience," *Philosophical Transactions of the Royal Society B: Biological Sciences*, vol. 371, pp. 1–12, oct 2016. doi: 10.1098/rstb.2015.0348.

[29] M. D'Esposito, E. Zarahn, G. K. Aguirre, and B. Rypma, "The Effect of Normal Aging on the Coupling of Neural Activity to the Bold Hemodynamic Response," *NeuroImage*, vol. 10, pp. 6–14, jul 1999. doi: 10.1006/nimg.1999.0444.

[30] N. K. Logothetis and B. A. Wandell, "Interpreting the BOLD Signal," *Annual Review of Physiology*, vol. 66, pp. 735–769, mar 2004. doi: 10.1146/annurev.physiol.66.082602.092845.

[31] M. Lindquist and T. D. Wager, "Principles of functional Magnetic Resonance Imaging," in *Handbook of neuroimaging data analysis*, ch. 1, pp. 3–48, Chapman and Hall/CRC, nov 2016. ISBN: 9781315373652. Accessed on: 2020-02-28.

[32] The Round Table Foundation, "Functional Imaging," 2017. Accessed on: 2020-03-25. [Online]. Available: https://www.magnetic-resonance.org/ch/11-03.html.

[33] R. B. Buxton, K. Uludağ, D. J. Dubowitz, and T. T. Liu, "Modeling the hemodynamic response to brain activation," *NeuroImage*, vol. 23, pp. S220–S233, jan 2004. doi: 10.1016/j.neuroimage.2004.07.013.

[34] G. Aguirre, E. Zarahn, and M. D'Esposito, "The Variability of Human, BOLD Hemodynamic Responses," *NeuroImage*, vol. 8, pp. 360–369, nov 1998. doi: 10.1006/nimg.1998.0369.

[35] D. Rangaprakash, G.-R. Wu, D. Marinazzo, X. Hu, and G. Deshpande, "Hemodynamic response function (HRF) variability confounds resting-state fMRI functional connectivity," *Magnetic Resonance in Medicine*, vol. 80, pp. 1697–1713, oct 2018. doi: 10.1002/mrm.27146.

[36] D. A. Handwerker, J. Gonzalez-Castillo, M. D'Esposito, and P. A. Bandettini, "The continuing challenge of understanding and modeling hemodynamic variation in fMRI," *NeuroImage*, vol. 62, pp. 1017–1023, aug 2012. doi: 10.1016/j.neuroimage.2012.02.015.

[37] G. H. Glover, "Deconvolution of Impulse Response in Event-Related BOLD fMRI," *NeuroImage*, vol. 9, pp. 416–429, apr 1999. doi: 10.1006/nimg.1998.0419.

[38] P. N. Rosa, P. Figueiredo, and C. J. Silvestre, "On the distinguishability of HRF models in fMRI," *Frontiers in Computational Neuroscience*, vol. 9, may 2015. doi: 10.3389/fncom.2015.00054.

[39] A. Jahn, "Chapter 3: The Hemodynamic Response Function (HRF)," 2019. Accessed on: 2020-04-06. [Online]. Available: https://andysbrainbook.readthedocs.io/en/latest/fMRI_Short_Course/Statistics/03_Stats_HRF_Overview.html.

[40] E. Y. Liu, F. Haist, D. J. Dubowitz, and R. B. Buxton, "Cerebral blood volume changes during the BOLD post-stimulus undershoot measured with a combined normoxia/hyperoxia method," *NeuroImage*, vol. 185, pp. 154–163, jan 2019. doi: 10.1016/j.neuroimage.2018.10.032.

[41] K. J. Worsley and C. Liao, "A general statistical analysis for fMRI data," 2001. Accessed on: 2020-08-23. [Online]. Available: https://www.math.mcgill.ca/keith/BICstat/.

[42] A. Elster, "fMRI Paradigm Design," 2019. Accessed on: 2020-01-04. [Online]. Available: http://mriquestions.com/fmri-paradigm-design.html.

[43] P. Wallisch, "Functional Magnetic Resonance Imaging," in *MATLAB for Neuroscientists*, pp. 361–379, Elsevier, jan 2014. doi: 10.1016/B978-0-12-383836-0.00024-2.

[44] R. L. Buckner, "Event-related fMRI and the hemodynamic response," *Human Brain Mapping*, vol. 6, no. 5-6, pp. 373–377, 1998. doi: 10.1002/(SICI)1097-0193(1998)6:5/6<373::AID-HBM8>3.0.CO;2-P.

[45] A. J. Taylor, J. H. Kim, and D. Ress, "Characterization of the hemodynamic response function across the majority of human cerebral cortex," *NeuroImage*, vol. 173, pp. 322–331, jun 2018. doi: 10.1016/j.neuroimage.2018.02.061.

[46] J. Steffener, M. Tabert, A. Reuben, and Y. Stern, "Investigating hemodynamic response variability at the group level using basis functions," *NeuroImage*, vol. 49, pp. 2113–2122, feb 2010. doi: 10.1016/j.neuroimage.2009.11.014.

[47] D. A. Handwerker, J. M. Ollinger, and M. D'Esposito, "Variation of BOLD hemodynamic responses across subjects and brain regions and their effects on statistical analyses," *NeuroImage*, vol. 21, pp. 1639–1651, apr 2004. doi: 10.1016/j.neuroimage.2003.11.029.

[48] M. Coucha, M. Abdelsaid, R. Ward, Y. Abdul, and A. Ergul, "Impact of Metabolic Diseases on Cerebral Circulation: Structural and Functional Consequences," *Comprehensive Physiology*, vol. 8, pp. 773–799, mar 2018. doi: 10.1002/cphy.c170019.

[49] D. Attwell, A. M. Buchan, S. Charpak, M. Lauritzen, B. A. MacVicar, and E. A. Newman, "Glial and neuronal control of brain blood flow," *Nature*, vol. 468, pp. 232–243, nov 2010. doi: 10.1038/nature09613.

[50] A. A. Phillips, F. H. Chan, M. M. Z. Zheng, A. V. Krassioukov, and P. N. Ainslie, "Neurovascular coupling in humans: Physiology, methodological advances and clinical implications," *Journal of Cerebral Blood Flow & Metabolism*, vol. 36, pp. 647–664, apr 2016. doi: 10.1177/0271678X15617954.

[51] S. Cinciute, "Translating the hemodynamic response: why focused interdisciplinary integration should matter for the future of functional neuroimaging," *PeerJ*, vol. 7, p. e6621, mar 2019. doi: 10.7717/peerj.6621.

[52] C. Iadecola, "The Neurovascular Unit Coming of Age: A Journey through Neurovascular Coupling in Health and Disease," *Neuron*, vol. 96, pp. 17–42, sep 2017. doi: 10.1016/j.neuron.2017.07.030.

[53] D. Abdelkarim, Y. Zhao, M. P. Turner, D. K. Sivakolundu, H. Lu, and B. Rypma, "A neural-vascular complex of age-related changes in the human brain: Anatomy, physiology, and implications for neurocognitive aging.," *Neuroscience and biobehavioral reviews*, vol. 107, pp. 927–944, sep 2019. doi: 10.1016/j.neubiorev.2019.09.005.

[54] C. Iadecola, "The Pathobiology of Vascular Dementia," *Neuron*, vol. 80, pp. 844–866, nov 2013. doi: 10.1016/j.neuron.2013.10.008.

[55] K. L. West, M. D. Zuppichini, M. P. Turner, D. K. Sivakolundu, Y. Zhao, D. Abdelkarim, J. S. Spence, and B. Rypma, "BOLD hemodynamic response function changes significantly with healthy aging," *NeuroImage*, vol. 188, pp. 198–207, dec 2019. doi: 10.1016/j.neuroimage.2018.12.012.

[56] B. Cauli and E. Hamel, "Revisiting the role of neurons in neurovascular coupling," *Frontiers in Neuroenergetics*, vol. 2, 2010. doi: 10.3389/fnene.2010.00009.

[57] I. G. Elbau, B. Brücklmeier, M. Uhr, J. Arloth, D. Czamara, V. I. Spoormaker, M. Czisch, K. E. Stephan, E. B. Binder, and P. G. Sämann, "The brain's hemodynamic response function rapidly changes under acute psychosocial stress in association with genetic and endocrine stress response markers," *Proceedings of the National Academy of Sciences*, vol. 115, pp. E10206–E10215, oct 2018. doi: 10.1073/pnas.1804340115.

[58] P. Kowiański, G. Lietzau, A. Steliga, M. Waśkow, and J. Moryś, "The astrocytic contribution to neurovascular coupling–still more questions than answers?," *Neuroscience research*, vol. 75, pp. 171–83, mar 2013. doi : 10.1016/j.neures.2013.01.014.

[59] P. J. Drew, "Vascular and neural basis of the BOLD signal," *Current Opinion in Neurobiology*, vol. 58, pp. 61–69, oct 2019. doi: 10.1016/j.conb.2019.06.004.

[60] A. Battisti-Charbonney, J. Fisher, and J. Duffin, "The cerebrovascular response to carbon dioxide in humans.," *The Journal of physiology*, vol. 589, pp. 3039–48, jun 2011. doi: 10.1113/jphysiol.2011.206052.

[61] K. A. Tsvetanov, R. N. A. Henson, and J. B. Rowe, "Separating vascular and neuronal effects of age on fMRI BOLD signals." doi: 10.1101/836619, 2019.

[62] H. Angleys, S. N. Jespersen, and L. Østergaard, "The effects of capillary transit time heterogeneity on the BOLD signal.," *Human brain mapping*, vol. 39, pp. 2329–2352, jun 2018. doi: 10.1002/hbm.23991.

[63] K. Uludağ and P. Blinder, "Linking brain vascular physiology to hemodynamic response in ultra-high field MRI.," *NeuroImage*, vol. 168, pp. 279–295, mar 2018. doi: 10.1016/j.neuroimage.2017.02.063.

[64] C. Huneau, H. Benali, and H. Chabriat, "Investigating Human Neurovascular Coupling Using Functional Neuroimaging: A Critical Review of Dynamic Models," *Frontiers in Neuroscience*, vol. 9, dec 2015. doi: 10.3389/fnins.2015.00467.

[65] E. Amaro and G. J. Barker, "Study design in fMRI: Basic principles," *Brain and Cognition*, vol. 60, pp. 220–232, apr 2006. doi: 10.1016/j.bandc.2005.11.009.

[66] O. Josephs and R. N. A. Henson, "Event-related functional magnetic resonance imaging: modelling, inference and optimization," *Philosophical Transactions of the Royal Society of London. Series B: Biological Sciences*, vol. 354, pp. 1215–1228, jul 1999. doi: 10.1098/rstb.1999.0475.

[67] K. P. Miyapuram, *Introduction to fMRI: experimental design and data analysis*. PhD thesis, University of Cambridge, 2008. Accessed on: 2020-06-30. [Online]. Available: http://cogprints.org/6193/.

[68] C. Pernet, "fMRI designs," 2013. Accessed on: 2020-06-29. [Online]. Available: http://www.sbirc.ed.ac.uk/cyril/fMRI3.html.

[69] Y. Tie, R. O. Suarez, S. Whalen, A. Radmanesh, I. H. Norton, and A. J. Golby, "Comparison of blocked and event-related fMRI designs for pre-surgical language mapping," *NeuroImage*, vol. 47, pp. T107–T115, 2009. doi: 10.1016/j.neuroimage.2008.11.020.

[70] M. W. Chee, V. Venkatraman, C. Westphal, and S. C. Siong, "Comparison of block and event-related fMRI designs in evaluating the word-frequency effect," *Human Brain Mapping*, vol. 18, pp. 186–193, mar 2003. doi: 10.1002/hbm.10092.

[71] S. Bishop, K. Watkins, H. Johansen-Berg, and J. Devlin, "Experimental Design," 2019. Accessed on: 2020-06-29. [Online]. Available: https://fsl.fmrib.ox.ac.uk/fslcourse/physics+apps/experimentaldesign-2014augSJB.pdf.

[72] R. L. Buckner, P. A. Bandettini, K. M. O'Craven, R. L. Savoy, S. E. Petersen, M. E. Raichle, and B. R. Rosen, "Detection of cortical activation during averaged single trials of

a cognitive task using functional magnetic resonance imaging," *Proceedings of the National Academy of Sciences*, vol. 93, pp. 14878–14883, dec 1996. doi: 10.1073/pnas.93.25.14878.

[73] A. M. Dale and R. L. Buckner, "Selective averaging of rapidly presented individual trials using fMRI," *Human Brain Mapping*, vol. 5, no. 5, pp. 329–340, 1997. doi: 10.1002/(SICI)1097-0193(1997)5:5<329::AID-HBM1.

[74] S. A. Huettel, "Event-related fMRI in cognition," *NeuroImage*, vol. 62, pp. 1152–1156, aug 2012. doi: 10.1016/j.neuroimage.2011.08.113.

[75] A. M. Dale, "Optimal experimental design for event-related fMRI," *Human Brain Mapping*, vol. 8, pp. 109–114, jan 1999. doi: 10.1002/(SICI)1097-0193(1999)8:2/3<109::AID-HBM7>3.0.CO;2-W.

[76] D. I. Donaldson, "Parsing brain activity with fMRI and mixed designs: what kind of a state is neuroimaging in?," *Trends in Neurosciences*, vol. 27, pp. 442–444, aug 2004. doi: 10.1016/j.tins.2004.06.001.

[77] K. M. Visscher, F. M. Miezin, J. E. Kelly, R. L. Buckner, D. I. Donaldson, M. P. McAvoy, V. M. Bhalodia, and S. E. Petersen, "Mixed blocked/event-related designs separate transient and sustained activity in fMRI," *NeuroImage*, vol. 19, pp. 1694–1708, aug 2003. doi: 10.1016/S1053-8119(03)00178-2.

[78] S. E. Petersen and J. W. Dubis, "The mixed block/event-related design," *NeuroImage*, vol. 62, pp. 1177–1184, aug 2012. doi: 10.1016/j.neuroimage.2011.09.084.

[79] T. T. Liu, "The development of event-related fMRI designs," *NeuroImage*, vol. 62, pp. 1157–1162, aug 2012. doi: 10.1016/j.neuroimage.2011.10.008.

[80] M. P. Turner, N. A. Hubbard, D. K. Sivakolundu, L. M. Himes, J. L. Hutchison, J. Hart, J. S. Spence, E. M. Frohman, T. C. Frohman, D. T. Okuda, and B. Rypma, "Preserved canonicality of the BOLD hemodynamic response reflects healthy cognition: Insights into the healthy brain through the window of Multiple Sclerosis," *NeuroImage*, vol. 190, pp. 46–55, apr 2019. doi: 10.1016/j.neuroimage.2017.12.081.

[81] M. A. Lindquist, J. Meng Loh, L. Y. Atlas, and T. D. Wager, "Modeling the hemodynamic response function in fMRI: Efficiency, bias and mis-modeling," *NeuroImage*, vol. 45, pp. S187–S198, mar 2009. doi: 10.1016/j.neuroimage.2008.10.065.

[82] M. D'Esposito, L. Y. Deouell, and A. Gazzaley, "Alterations in the BOLD fMRI signal with ageing and disease: a challenge for neuroimaging," *Nature Reviews Neuroscience*, vol. 4, pp. 863–872, nov 2003. doi: 10.1038/nrn1246.

[83] A. C. Roc, J. Wang, B. M. Ances, D. S. Liebeskind, S. E. Kasner, and J. A. Detre, "Altered Hemodynamics and Regional Cerebral Blood Flow in Patients With Hemodynamically Significant Stenoses," *Stroke*, vol. 37, pp. 382–387, feb 2006. doi: 10.1161/01.STR.0000198807.31299.43.

[84] F. Miezin, L. Maccotta, J. Ollinger, S. Petersen, and R. Buckner, "Characterizing the Hemodynamic Response: Effects of Presentation Rate, Sampling Procedure, and the Possibility of Ordering Brain Activity Based on Relative Timing," *NeuroImage*, vol. 11, pp. 735–759, jun 2000. doi: 10.1006/nimg.2000.0568.

[85] M. A. Lindquist and T. D. Wager, "Validity and power in hemodynamic response modeling: A comparison study and a new approach," *Human Brain Mapping*, vol. 28, pp. 764–784, aug 2007. doi: 10.1002/hbm.20310.

[86] N. K. Logothetis, "The Underpinnings of the BOLD Functional Magnetic Resonance Imaging Signal," *The Journal of Neuroscience*, vol. 23, pp. 3963–3971, may 2003. doi: 10.1523/JNEUROSCI.23-10-03963.2003.

[87] K. K. Peck, A. B. Moore, B. A. Crosson, M. Gaiefsky, K. S. Gopinath, K. White, and R. W. Briggs, "Functional Magnetic Resonance Imaging Before and After Aphasia Therapy," *Stroke*, vol. 35, pp. 554–559, feb 2004. doi: 10.1161/01.STR.0000110983.50753.9D.

[88] B. Bonakdarpour, T. Parrish, and C. Thompson, "Hemodynamic response function in patients with stroke-induced aphasia: Implications for fMRI data analysis," *NeuroImage*, vol. 36, pp. 322–331, jun 2007. doi: 10.1016/j.neuroimage.2007.02.035.

[89] S. A. Hamed, "Brain injury with diabetes mellitus: evidence, mechanisms and treatment implications," *Expert Review of Clinical Pharmacology*, vol. 10, pp. 409–428, feb 2017. doi: 10.1080/17512433.2017.1293521.

[90] P. Riederer, A. D. Korczyn, S. S. Ali, O. Bajenaru, M. S. Choi, M. Chopp, V. Dermanovic-Dobrota, E. Grünblatt, K. A. Jellinger, M. A. Kamal, W. Kamal, J. Leszek, T. M. Sheldrick-Michel, G. Mushtaq, B. Meglic, R. Natovich, Z. Pirtosek, M. Rakusa, M. Salkovic-Petrisic, R. Schmidt, A. Schmitt, G. R. Sridhar, L. Vécsei, Z. B. Wojszel, H. Yaman, Z. G. Zhang, and T. Cukierman-Yaffe, "The diabetic brain and cognition," *Journal of Neural Transmission*, vol. 124, pp. 1431–1454, nov 2017. doi: 10.1007/s00702-017-1763-2.

[91] S. Prasad, R. K. Sajja, P. Naik, and L. Cucullo, "Diabetes Mellitus and Blood-Brain Barrier Dysfunction: An Overview," *Journal of Pharmacovigilance*, vol. 02, no. 02, p. 125, 2014. doi: 10.4172/2329-6887.1000125.

[92] A. I. Kelly-Cobbs, R. Prakash, M. Coucha, R. A. Knight, W. Li, S. N. Ogbi, M. Johnson, and A. Ergul, "Cerebral Myogenic Reactivity and Blood Flow in Type 2 Diabetic Rats: Role of Peroxynitrite in Hypoxia-Mediated Loss of Myogenic Tone," *Journal of Pharmacology and Experimental Therapeutics*, vol. 342, pp. 407–415, aug 2012. doi: 10.1124/jpet.111.191296.

[93] E. M. Hillman, "Coupling Mechanism and Significance of the BOLD Signal: A Status Report," *Annual Review of Neuroscience*, vol. 37, pp. 161–181, jul 2014. doi: 10.1146/annurev-neuro-071013-014111.

[94] University of South Carolina Board of Trustees, "Slice Time Correction," 2012. Accessed on: 2020-04-27. [Online]. Available: https://www.mccauslandcenter.sc.edu/crnl/tools/stc.

[95] D. B. Parker and Q. R. Razlighi, "The Benefit of Slice Timing Correction in Common fMRI Preprocessing Pipelines," *Frontiers in Neuroscience*, vol. 13, p. 821, aug 2019. doi: 10.3389/fnins.2019.00821.

[96] R. Goebel, "BrainVoyager Users Guide," 2017. Accessed on: 2020-04-26. [Online]. Available: https://www.brainvoyager.com/bv/doc/UsersGuide/BrainVoyagerUsersGuide.html.

[97] "Motion Correction," 2018. Accessed on: 2020-04-29. [Online]. Available: https://support.brainvoyager.com/brainvoyager/functional-analysis-preparation/29-pre-processing/85-motion-correction.

[98] F. Godenschweger, U. Kägebein, D. Stucht, U. Yarach, A. Sciarra, R. Yakupov, F. Lüsebrink, P. Schulze, and O. Speck, "Motion correction in MRI of the brain," *Physics in Medicine and Biology*, vol. 61, pp. R32–R56, mar 2016. doi: 10.1088/0031-9155/61/5/R32.

[99] S. Clare, *Functional MRI : Methods and Applications*. PhD thesis, University of Nottingham, 1997. Accessed on: 2020-05-06. [Online]. Available: https://users.fmrib.ox.ac.uk/ stuart/thesis/chapter_6/section6_2.html.

[100] "Smoothing FAQ," 2008. Accessed on: 2020-05-07. [Online]. Available: http://mindhive.mit.edu/node/112.

[101] "Spatial Smoothing," 2018. Accessed on: 2020-05-12. [Online]. Available: https://support.brainvoyager.com/brainvoyager/functional-analysis-preparation/29-pre-processing/86-spatial-smoothing.

[102] J. Tanabe, D. Miller, J. Tregellas, R. Freedman, and F. G. Meyer, "Comparison of detrending methods for optimal fMRI preprocessing," *NeuroImage*, vol. 15, pp. 902–907, apr 2002. doi: 10.1006/nimg.2002.1053.

[103] "Temporal Filtering FAQ," 2008. Accessed on: 2020-05-16. [Online]. Available: http://mindhive.mit.edu/node/116.

[104] P. Kalavathi and V. B. S. Prasath, "Methods on Skull Stripping of MRI Head Scan Images—a Review," *Journal of Digital Imaging*, vol. 29, pp. 365–379, jun 2016. doi: 10.1007/s10278-015-9847-8.

[105] S. Roy and P. Maji, "A simple skull stripping algorithm for brain MRI," in *2015 Eighth International Conference on Advances in Pattern Recognition (ICAPR)*, pp. 1–6, IEEE, jan 2015. doi: 10.1109/ICAPR.2015.7050671.

[106] D. Mahapatra, "Skull Stripping of Neonatal Brain MRI: Using Prior Shape Information with Graph Cuts," *Journal of Digital Imaging*, vol. 25, pp. 802–814, dec 2012. doi: 10.1007/s10278-012-9460-z.

[107] J. Swiebocka-Wiek, "Skull Stripping for MRI Images Using Morphological Operators," in *Lecture Notes in Computer Science (including subseries Lecture Notes in Artificial Intelligence and Lecture Notes in Bioinformatics)*, vol. 9842 LNCS, pp. 172–182, Springer Verlag, sep 2016. doi: 10.1007/978-3-319-45378-1_16.

[108] R. Goebel, F. Esposito, and E. Formisano, "Analysis of functional image analysis contest (FIAC) data with brainvoyager QX: From single-subject to cortically aligned group general linear model analysis and self-organizing group independent component analysis," *Human Brain Mapping*, vol. 27, pp. 392–401, may 2006. doi: 10.1002/hbm.20249.

[109] Z. Hou, "A Review on MR Image Intensity Inhomogeneity Correction," *International Journal of Biomedical Imaging*, vol. 2006, pp. 1–11, 2006. 10.1155/IJBI/2006/49515.

[110] S. Roy, A. Carass, P.-L. Bazin, and J. L. Prince, "Intensity inhomogeneity correction of magnetic resonance images using patches," in *Medical Imaging 2011: Image Processing* (B. M. Dawant and D. R. Haynor, eds.), vol. 7962, p. 79621F, SPIE, mar 2011. doi: 10.1117/12.877466.

[111] J. Ashburner and K. J. Friston, *Rigid Body Registration*. London: Academic Press Inc., 2 ed., 2004. ISBN: 9780080472959. Accessed on: 2020-05-23.

[112] B. Jupp and T. J. O'Brien, "Application of Coregistration for Imaging of Animal Models of Epilepsy," *Epilepsia*, vol. 48, pp. 82–89, sep 2007. doi: 10.1111/j.1528-1167.2007.01245.x.

[113] "Coregistration FAQ," 2008. Accessed on: 2020-05-24. [Online]. Available: http://mindhive.mit.edu/node/63.

[114] X. Zhang, Y. Feng, W. Chen, X. Li, A. V. Faria, Q. Feng, and S. Mori, "Linear Registration of Brain MRI Using Knowledge-Based Multiple Intermediator Libraries," *Frontiers in Neuroscience*, vol. 13, p. 909, sep 2019. doi: 10.3389/fnins.2019.00909.

[115] I. Bankman, *Handbook of Medical Imaging: Processing and Analysis Management*. Academic Press Inc., 2000. ISBN: 9780080559148. Accessed on: 2020-05-23.

[116] A. Elster, "Co-Registration/Normalization," 2020. Accessed on: 2020-05-23. [Online]. Available: http://mri-q.com/registrationnormalization.html.

[117] J. Huntenburg, *Evaluating nonlinear coregistration of BOLD EPI and T1w images*. PhD thesis, Max Planck Institute for Human Cognitive and Brain Sciences, 2014. Accessed on: 2020-05-25. [Online]. Available: https://pure.mpg.de/rest/items/item_2327525/component/file_2327523/content.

[118] E. Haber and J. Modersitzki, "Intensity Gradient Based Registration and Fusion of Multi-modal Images," in *Lecture Notes in Computer Science*, vol. 4191 LNCS, pp. 726–733, Springer Verlag, 2006. doi: 10.1007/11866763_89.

[119] D. Jiang, Y. Shi, D. Yao, Y. Fan, M. Wang, and Z. Song, "Multimodal image registration based on binary gradient angle descriptor," *International Journal of Computer Assisted Radiology and Surgery*, vol. 12, pp. 2157–2167, dec 2017. doi: 10.1007/s11548-017-1661-y.

[120] E. Montin, A. Belfatto, M. Bologna, S. Meroni, C. Cavatorta, E. Pecori, B. Diletto, M. Massimino, M. C. Oprandi, G. Poggi, F. Arrigoni, D. Peruzzo, E. Pignoli, L. Gandola, P. Cerveri, and L. Mainardi, "A multi-metric registration strategy for the alignment of longitudinal brain images in pediatric oncology," *Medical & Biological Engineering & Computing*, vol. 58, pp. 843–855, apr 2020. doi: 10.1007/s11517-019-02109-4.

[121] E. Hodneland, A. Lundervold, J. Rørvik, and A. Z. Munthe-Kaas, "Normalized gradient fields for nonlinear motion correction of DCE-MRI time series," *Computerized Medical Imaging and Graphics*, vol. 38, pp. 202–210, apr 2014. doi: 10.1016/j.compmedimag.2013.12.007.

[122] T. Polzin, J. Rühaak, R. Werner, J. Strehlow, S. Heldmann, H. Handels, and J. Modersitzki, "Combining Automatic Landmark Detection and Variational Methods for Lung CT Registration," in *Fifth International Workshop on Pulmonary Image Analysis*, 2013. Accessed on: 2020-06-21. [Online]. Available: https://www.researchgate.net/publication/256481991_Combining_Automatic_Landmark_Detection_and_Variational_Methods_for_Lung_CT_Registration.

[123] X. Sun, L. Shi, Y. Luo, W. Yang, H. Li, P. Liang, K. Li, V. C. T. Mok, W. C. W. Chu, and D. Wang, "Histogram-based normalization technique on human brain magnetic resonance images from different acquisitions," *BioMedical Engineering OnLine*, vol. 14, p. 73, dec 2015. doi: 10.1186/s12938-015-0064-y.

[124] F. Fischmeister, I. Höllinger, N. Klinger, A. Geissler, M. Wurnig, E. Matt, J. Rath, S. Robinson, S. Trattnig, and R. Beisteiner, "The benefits of skull stripping in the normalization of clinical fMRI data," *NeuroImage: Clinical*, vol. 3, pp. 369–380, jan 2013. doi: 10.1016/j.nicl.2013.09.007.

[125] C. M. Moore, "Image normalization," 2020. Accessed on: 2020-05-31. [Online]. Available: https://radiopaedia.org/articles/image-normalization.

[126] J. F. Smith, J. Hur, C. M. Kaplan, and A. J. Shackman, "The Impact of Spatial Normalization for Functional Magnetic Resonance Imaging Data Analyses Revisited," *bioRxiv*, p. 272302, feb 2018. doi: 10.1101/272302.

[127] M. Jenkinson and M. Chappell, *General Linear model for Neuroimaging*. Oxford University Press, 2017. ISBN: 978-0-19-881630-0.

[128] M. Monti, "Statistical Analysis of fMRI Time-Series: A Critical Review of the GLM Approach," *Frontiers in Human Neuroscience*, vol. 5, p. 28, mar 2011. doi: 10.3389/fnhum.2011.00028.

[129] R. S. Bapi, V. S. C. Pammi, and K. P. Miyapuram, "Methods and Approaches for Characterizing Learning Related Changes Observed in functional MRI Data-A Review," in *Proceedings of the International Conference on Theoretical Neurobiology*, pp. 221–229, 2003. Accessed on: 2020-06-03. [Online]. Available: http://cogprints.org/5145/.

[130] R. Goebel, "Statistical Analysis and Modeling of Functional MRI Data," in *MRI in Psychiatry* (C. Mulert and M. E. Shenton, eds.), ch. 1, Berlin, Heidelberg: Springer Berlin Heidelberg, 2014. doi: 10.1007/978-3-642-54542-9.

[131] W. Haynes, "Bonferroni Correction," in *Encyclopedia of Systems Biology* (Dubitzky W., Wolkenhauer O., Cho KH., and Yokota H., eds.), pp. 154–154, New York, NY: Springer New York, 2013. doi: 10.1007/978-1-4419-9863-7_1213.

[132] I. Kononenko and M. Kukar, "Machine Learning Basics," in *Machine Learning and Data Mining*, ch. 3, pp. 59–105, Elsevier, jan 2007. doi: 10.1533/9780857099440.59.

[133] J. H. McDonald, "Multiple comparisons," 2014. Accessed on: 2020-06-19. [Online]. Available: http://www.biostathandbook.com/multiplecomparisons.html.

[134] C. M. Lacadie, R. K. Fulbright, N. Rajeevan, R. T. Constable, and X. Papademetris, "More accurate Talairach coordinates for neuroimaging using non-linear registration," *NeuroImage*, vol. 42, pp. 717–725, aug 2008. doi: 10.1016/j.neuroimage.2008.04.240.

[135] J. L. Lancaster, M. G. Woldorff, L. M. Parsons, M. Liotti, C. S. Freitas, L. Rainey, P. V. Kochunov, D. Nickerson, S. A. Mikiten, and P. T. Fox, "Automated Talairach Atlas labels for functional brain mapping," *Human Brain Mapping*, vol. 10, pp. 120–131, jul 2000. doi: 10.1002/1097-0193(200007)10:3<120::aid-hbm30>3.0.CO;2-8.

[136] G. Boynton, "Event-Related fMRI and 'Deconvolution'," 2010. Accessed on: 2020-06-26. [Online]. Available: http://www.mbfys.ru.nl/ robvdw/DGCN22/PRACTICUM_2011/LABS_2011/ALTERNATIVE_LABS/Lesson_13.html.

[137] R. Goebel, "Deconvolution analysis of rapid event-related designs," 2000. Accessed on: 2020-06-26. [Online]. Available: http://www.brainvoyager.de/BV2000OnlineHelp/BrainVoyagerWebHelp/Deconvolution_analysis_of_rapid_event-related_designs.htm.

[138] "BrainVoyager Discussion Forum - Deconvolution analysis," 2006. Accessed on: 2020-06-26. [Online]. Available: http://www.brainvoyager.com/ubb/Forum4/HTML/000374.html.

[139] P. S. F. Bellgowan, Z. S. Saad, and P. A. Bandettini, "Understanding neural system dynamics through task modulation and measurement of functional MRI amplitude, latency, and width," *Proceedings of the National Academy of Sciences*, vol. 100, pp. 1415–1419, feb 2003. doi: 10.1073/pnas.0337747100.

[140] B. Bonakdarpour, P. Beeson, A. DeMarco, and S. Rapcsak, "Variability in blood oxygen level dependent (BOLD) signal in patients with stroke-induced and primary progressive aphasia," *NeuroImage: Clinical*, vol. 8, pp. 87–94, mar 2015. doi: 10.1016/j.nicl.2015.03.014.

[141] Southwest Licking Schools District, "The Trapezoidal Rule," tech. rep., Southwest Licking Schools District, Pataskala, Ohio, 2017. Accessed on: 2020-07-15. [Online]. Available: https://fliphtml5.com/sibd/jlun/basic.

[142] H. Achyuthuni, "Univariate analysis," 2018. Accessed on: 2020-07-15. [Online]. Available: https://www.rpubs.com/harshaash/Univariate_analysis.

[143] M. L. Ramírez, "UnivarScatter: A univariate scatter plot for matlab," 2020. Accessed on: 2020-07-15. [Online]. Available: https://github.com/manulera/UnivarScatter.

[144] M. Waskom, "Plotting with categorical data," 2020. Accessed on: 2020-07-15. [Online]. Available: https://seaborn.pydata.org/tutorial/categorical.html.

[145] Del Siegle, "t Test," 2020. Accessed on: 2020-07-15. [Online]. Available: https://researchbasics.education.uconn.edu/t-test/#.

[146] A. BenSaïda, "Shapiro-Wilk and Shapiro-Francia normality tests," 2020. Accessed on: 2020-09-28. [Online]. Available: https://www.mathworks.com/matlabcentral/fileexchange/13964-shapiro-wilk-and-shapiro-francia-normality-tests.

[147] M. Saculinggan and E. A. Balase, "Empirical Power Comparison Of Goodness of Fit Tests for Normality In The Presence of Outliers," *Journal of Physics: Conference Series*, vol. 435, p. 012041, apr 2013. doi: 10.1088/1742-6596/435/1/012041.

[148] M. Havlicek, D. Ivanov, A. Roebroeck, and K. Uludağ, "Determining Excitatory and Inhibitory Neuronal Activity from Multimodal fMRI Data Using a Generative Hemodynamic Model," *Frontiers in Neuroscience*, vol. 11, p. 616, nov 2017. doi: 10.3389/fnins.2017.00616.

[149] P. M. Rossini, "Does cerebrovascular disease affect the coupling between neuronal activity and local haemodynamics?," *Brain*, vol. 127, pp. 99–110, jan 2004. doi: 10.1093/brain/awh012.

[150] J. R. Whittaker, I. D. Driver, M. G. Bright, and K. Murphy, "The absolute CBF response to activation is preserved during elevated perfusion: Implications for neurovascular coupling measures," *NeuroImage*, vol. 125, pp. 198–207, jan 2016. doi: 10.1016/j.neuroimage.2015.10.023.

A

Appendices

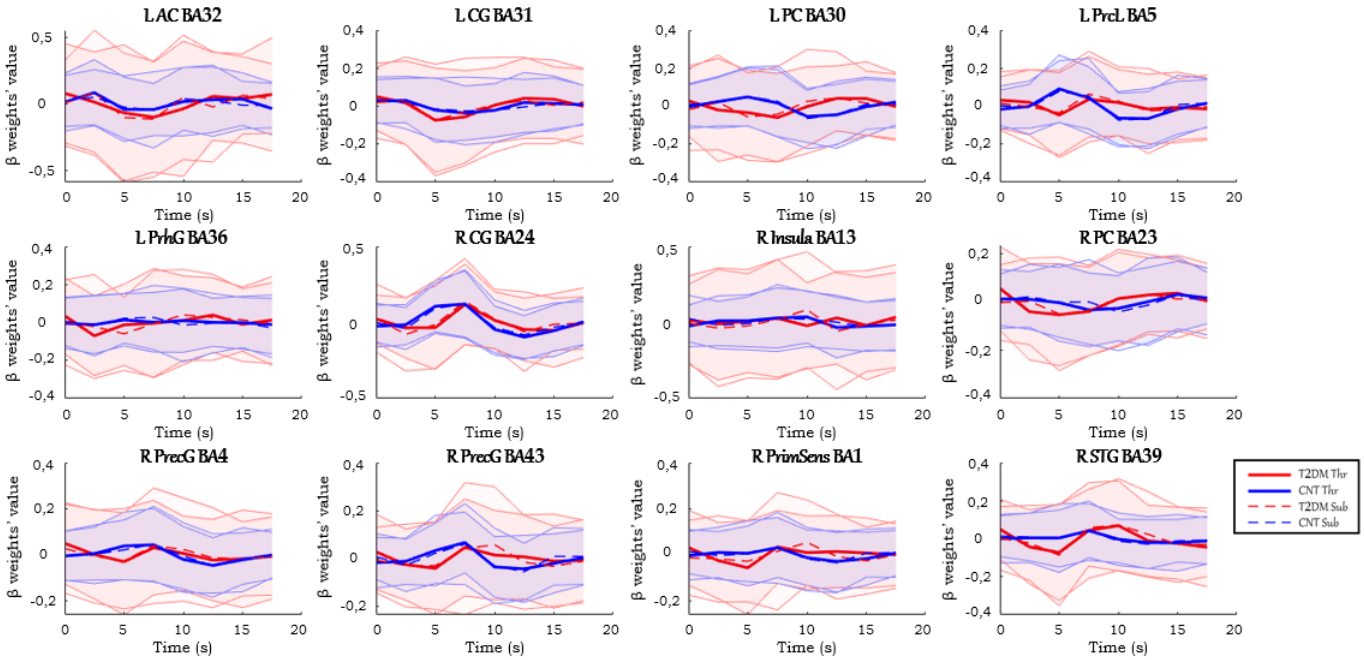

Figure A.1: Average HRFs: negative signal change ROIs.

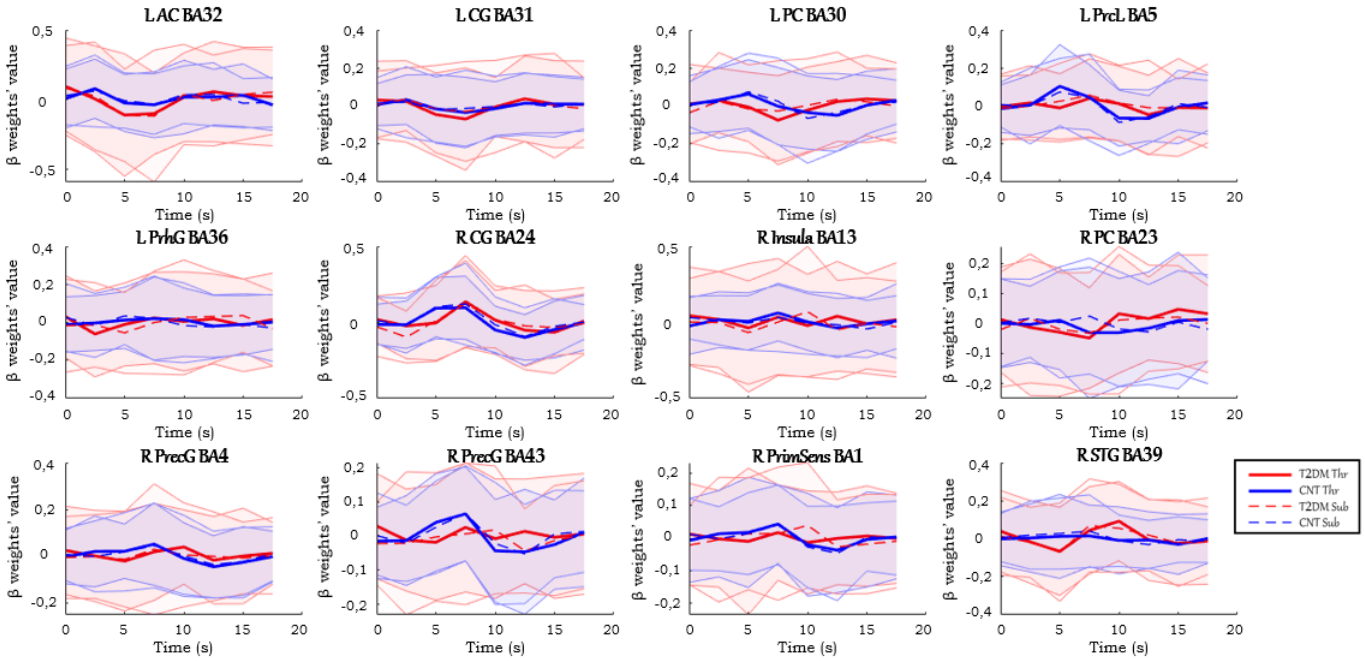

Figure A.2: Median HRFs: negative signal change ROIs.

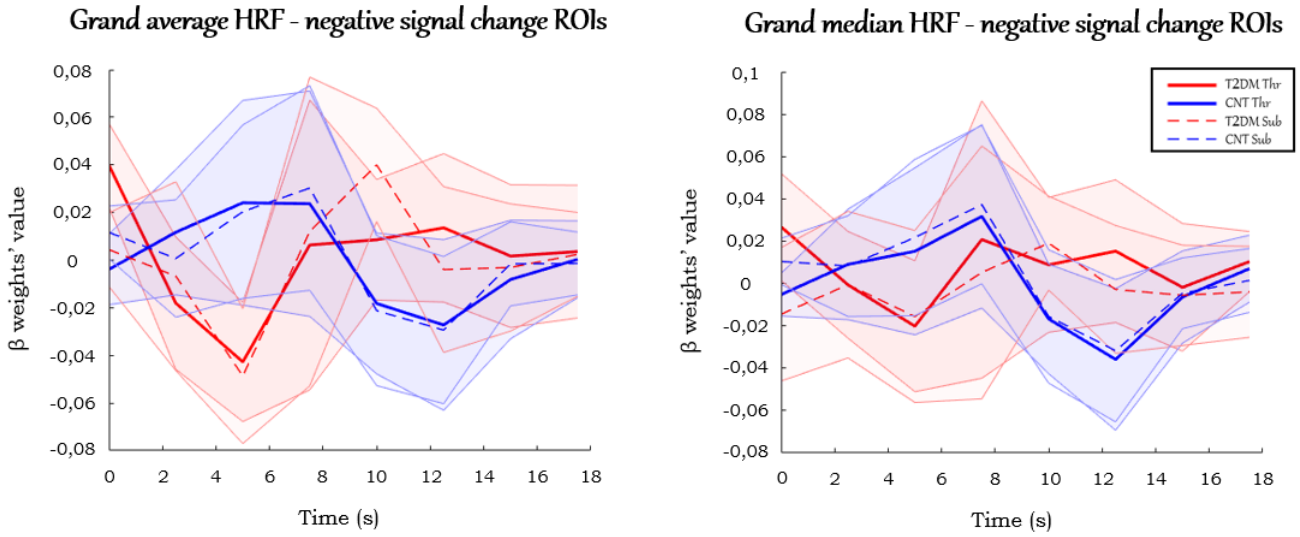

(a) Grand average HRFs. **(b)** Grand median HRFs.

Figure A.3: Grand average and grand median HRFs: negative signal change ROIs.

Table A.1: Grand Analysis' statistical component - negative signal change ROIs.

		CNT		T2DM	
		Average ± Standard Deviation	*Median ± Interquartile Range*	*Average ± Standard Deviation*	*Median ± Interquartile Range*
HRF peak amplitude (beta weights)	**Threshold**	0,053 ± 0,031	0,057 ± 0,046	0,055 ± 0,024	0,040 ± 0,036
	Submaximum	0,050 ± 0,027	0,043 ± 0,036	0,062 ± 0,031	0,040 ± 0,039
HRF peak latency (s)	**Threshold**	9,375 ± 3,392	10,0 ± 2,5	9,375 ± 5,851	10,00 ± 11,25
	Submaximum	9,167 ± 3,589	10,0 ± 2,5	11,875 ± 2,845	12,5 ± 5
HRF relative slope to peak (beta weights/s)	**Threshold**	0,007 ± 0,005	0,007 ± 0,006	0,001 ± 0,003	0,001 ± 0,003
	Submaximum	0,004 ± 0,004	0,004 ± 0,006	0,006 ± 0,004	0,004 ± 0,003
HRF AUC (a.u.)	**Threshold**	0,757 ± 0,389	0,745 ± 0,342	0,968 ± 0,345	0,975 ± 0,598
	Submaximum	0,818 ± 0,345	0,749 ± 0,547	1,002 ± 0,462	0,644 ± 0,653
HRF PCSA (a.u.)	**Threshold**	0,217 ± 0,126	0,218 ± 0,186	0,219 ± 0,085	0,227 ± 0,177
	Submaximum	0,197 ± 0,109	0,191 ± 0,166	0,231 ± 0,087	0,182 ± 0,126
HRF NCSA (a.u.)	**Threshold**	0,207 ± 0,116	0,150 ± 0,129	0,242 ± 0,122	0,174 ± 0,190
	Submaximum	0,187 ± 0,091	0,149 ± 0,087	0,249 ± 0,094	0,174 ± 0,141

Table A.2: Shapiro-Wilk test's p-values ($\alpha = 0.05$) and the median and interquartile range of each HRF parameter of each condition per ROI - Negative signal change ROIs.

		HRF peak amplitude (beta weights)				HRF peak latency (s)			
		Threshold		Submaximum		Threshold		Submaximum	
		CNT	T2DM	CNT	T2DM	CNT	T2DM	CNT	T2DM
L AC BA32	**p-value**	1,208E-03	7,662E-07	6,286E-04	2,448E-05	7,004E-07	3,301E-06	3,641E-06	5,547E-05
	Median ± Interquartile Range	0,188 ± 0,111	0,198 ± 0,148	0,154 ± 0,122	0,218 ± 0,226	7,5 ± 7,5	6,25 ± 7,5	7,5 ± 7,5	7,5 ± 7,5
L CG BA31	**p-value**	0,001	2,439E-05	1,050E-04	4,809E-09	8,181E-10	5,029E-06	3,296E-08	5,827E-05
	Median ± Interquartile Range	0,175 ± 0,172	0,202 ± 0,198	0,155 ± 0,141	0,201 ± 0,149	5,000 ± 8,125	7,5 ± 10	5 ± 10	7,50 ± 6,25
L PC BA30	**p-value**	2,254E-09	4,477E-07	3,189E-09	1,114E-09	6,039E-09	2,566E-05	1,018E-08	1,621E-05
	Median ± Interquartile Range	0,156 ± 0,142	0,202 ± 0,181	0,134 ± 0,122	0,187 ± 0,215	5,0 ± 7,5	7,5 ± 7,5	5,0 ± 7,5	7,50 ± 6,25
L PrcL BA5	**p-value**	2,237E-05	1,577E-08	0,001	1,031E-09	2,182E-07	2,838E-05	7,906E-07	1,970E-04
	Median ± Interquartile Range	0,184 ± 0,158	0,182 ± 0,211	0,207 ± 0,173	0,178 ± 0,197	5 ± 10	7,5 ± 7,5	7,5 ± 7,5	10 ± 7,5
L PrhG BA36	**p-value**	2,496E-05	3,031E-09	2,711E-06	7,025E-09	1,208E-08	3,253E-05	1,958E-09	1,600E-04
	Median ± Interquartile Range	0,121 ± 0,130	0,233 ± 0,190	0,116 ± 0,103	0,230 ± 0,223	5 ± 10	7,5 ± 7,5	5,0 ± 7,5	7,5 ± 7,5
R CG BA24	**p-value**	0,001	1,260E-06	1,572E-07	5,703E-08	1,338E-08	1,849E-04	7,918E-09	1,581E-04
	Median ± Interquartile Range	0,219 ± 0,125	0,218 ± 0,201	0,168 ± 0,133	0,190 ± 0,184	5,000 ± 8,125	7,5 ± 5	5 ± 10	7,5 ± 5
R Insula BA13	**p-value**	4,293E-09	6,824E-05	3,672E-07	0,001	8,719E-08	2,177E-05	1,044E-07	2,103E-05
	Median ± Interquartile Range	0,160 ± 0,151	0,210 ± 0,257	0,185 ± 0,160	0,250 ± 0,238	5,000 ± 8,125	7,5 ± 7,5	5,0 ± 7,5	7,5 ± 5
R PC BA23	**p-value**	1,580E-05	0,007	4,789E-06	5,533E-06	2,398E-08	2,641E-05	6,456E-09	7,406E-05
	Median ± Interquartile Range	0,185 ± 0,145	0,214 ± 0,147	0,197 ± 0,153	0,204 ± 0,162	5 ± 7,5	7,50 ± 6,25	5 ± 10	7,5 ± 5
R PrecG BA4	**p-value**	5,913E-04	5,940E-05	9,167E-05	3,022E-06	3,446E-06	7,859E-06	3,083E-07	6,568E-05
	Median ± Interquartile Range	0,242 ± 0,221	0,226 ± 0,220	0,207 ± 0,220	0,229 ± 0,266	7,5 ± 7,5	5 ± 7,5	7,5 ± 7,5	7,5 ± 7,5
R PrecG BA43	**p-value**	0,001	3,145E-06	0,023	4,607E-07	9,388E-06	1,951E-05	1,974E-05	3,145E-04
	Median ± Interquartile Range	0,149 ± 0,120	0,207 ± 0,223	0,141 ± 0,091	0,181 ± 0,194	10,0 ± 7,5	10,0 ± 7,5	10,0 ± 7,5	7,5 ± 7,5
R PrimSens BA1	**p-value**	1,833E-06	0,011	2,885E-04	5,048E-04	7,470E-10	1,207E-04	4,811E-10	1,635E-04
	Median ± Interquartile Range	0,183 ± 0,179	0,226 ± 0,231	0,184 ± 0,177	0,236 ± 0,270	5 ± 5	7,50 ± 6,25	5,000 ± 3,125	7,5 ± 5
R STG BA39	**p-value**	7,810E-05	1,285E-04	3,738E-07	1,707E-10	6,538E-07	3,322E-05	1,479E-05	2,156E-05
	Median ± Interquartile Range	0,199 ± 0,161	0,211 ± 0,146	0,183 ± 0,148	0,217 ± 0,140	5 ± 10	7,5 ± 7,5	7,5 ± 7,5	7,5 ± 7,5

		HRF relative slope to peak (beta weights/s)				HRF AUC (a.u.)			
		Threshold		Submaximum		Threshold		Submaximum	
		CNT	T2DM	CNT	T2DM	CNT	T2DM	CNT	T2DM
L AC BA32	**p-value**	9,326E-03	3,076E-05	3,949E-04	6,715E-05	1,018E-07	3,567E-07	1,021E-05	9,865E-06
	Median ± Interquartile Range	0,031 ± 0,052	0,037 ± 0,078	0,015 ± 0,026	0,027 ± 0,077	3,052 ± 2,143	3,503 ± 4,061	3,244 ± 2,338	3,603 ± 3,885
L CG BA31	**p-value**	4,954E-07	1,780E-07	1,496E-07	1,145E-08	0,002	2,257E-10	0,001	3,475E-12
	Median ± Interquartile Range	0,041 ± 0,075	0,016 ± 0,041	0,035 ± 0,051	0,035 ± 0,040	2,874 ± 1,323	3,624 ± 3,330	2,989 ± 1,546	3,823 ± 2,582
L PC BA30	**p-value**	3,060E-08	1,849E-09	2,356E-07	6,106E-08	3,354E-09	5,195E-07	1,059E-05	2,314E-06
	Median ± Interquartile Range	0,047 ± 0,083	0,025 ± 0,052	0,031 ± 0,080	0,030 ± 0,056	2,782 ± 1,824	3,899 ± 3,499	2,752 ± 1,997	3,490 ± 5,256
L PrcL BA5	**p-value**	1,198E-09	2,463E-12	1,058E-11	2,498E-14	2,106E-06	6,797E-12	5,053E-06	8,524E-11
	Median ± Interquartile Range	0,033 ± 0,074	0,020 ± 0,053	0,026 ± 0,031	0,023 ± 0,039	3,503 ± 3,079	3,817 ± 3,250	3,254 ± 2,583	4,166 ± 3,807
L PrhG BA36	**p-value**	3,619E-09	5,030E-09	1,472E-08	5,350E-07	1,296E-05	3,213E-07	7,052E-09	4,254E-07
	Median ± Interquartile Range	0,017 ± 0,052	0,027 ± 0,055	0,030 ± 0,054	0,038 ± 0,044	2,591 ± 1,777	4,267 ± 4,343	2,434 ± 1,725	3,709 ± 3,534
R CG BA24	**p-value**	9,198E-06	5,500E-05	4,250E-06	1,566E-06	8,897E-05	2,277E-08	1,107E-05	2,002E-09
	Median ± Interquartile Range	0,049 ± 0,091	0,031 ± 0,048	0,048 ± 0,065	0,022 ± 0,049	3,079 ± 2,755	4,323 ± 3,910	3,203 ± 2,715	3,410 ± 3,556
R Insula BA13	**p-value**	2,940E-11	1,225E-06	9,070E-08	2,871E-05	1,369E-08	4,462E-10	4,151E-04	1,453E-10
	Median ± Interquartile Range	0,035 ± 0,065	0,022 ± 0,051	0,040 ± 0,064	0,036 ± 0,056	2,776 ± 2,276	3,724 ± 4,275	3,224 ± 2,485	4,495 ± 4,041
R PC BA23	**p-value**	3,038E-05	9,607E-06	3,629E-07	1,116E-04	2,559E-06	5,735E-06	3,473E-03	3,117E-09
	Median ± Interquartile Range	0,042 ± 0,080	0,024 ± 0,050	0,046 ± 0,102	0,028 ± 0,052	3,237 ± 1,636	4,023 ± 2,925	3,633 ± 2,050	3,950 ± 2,622
R PrecG BA4	**p-value**	1,998E-06	1,336E-08	7,723E-05	2,791E-07	0,001	1,525E-04	1,050E-04	1,685E-07
	Median ± Interquartile Range	0,043 ± 0,076	0,024 ± 0,059	0,031 ± 0,051	0,022 ± 0,058	4,252 ± 3,930	3,851 ± 3,650	4,029 ± 3,737	3,875 ± 3,617
R PrecG BA43	**p-value**	2,257E-09	5,740E-09	1,168E-10	9,984E-08	0,004	5,132E-08	3,852E-04	5,369E-07
	Median ± Interquartile Range	0,018 ± 0,035	0,021 ± 0,046	0,017 ± 0,036	0,021 ± 0,031	2,996 ± 1,239	4,246 ± 3,675	2,635 ± 1,623	4,522 ± 3,850
R PrimSens BA1	**p-value**	9,102E-10	5,855E-07	2,727E-06	2,268E-04	9,945E-06	3,341E-04	4,198E-02	5,104E-05
	Median ± Interquartile Range	0,041 ± 0,052	0,027 ± 0,080	0,050 ± 0,074	0,045 ± 0,087	3,055 ± 2,342	3,966 ± 3,623	3,450 ± 2,785	4,206 ± 4,372
R STG BA39	**p-value**	2,129E-05	2,697E-05	1,754E-09	4,969E-07	3,998E-12	1,365E-08	1,492E-08	2,334E-09
	Median ± Interquartile Range	0,033 ± 0,070	0,029 ± 0,049	0,019 ± 0,036	0,032 ± 0,048	3,577 ± 2,453	4,168 ± 3,355	3,573 ± 2,435	3,748 ± 3,011

		HRF PCSA (a.u.)				HRF NCSA (a.u.)			
		Threshold		Submaximum		Threshold		Submaximum	
		CNT	T2DM	CNT	T2DM	CNT	T2DM	CNT	T2DM
L AC BA32	**p-value**	1,381E-07	1,050E-05	3,412E-07	2,530E-07	1,113E-07	1,114E-06	1,762E-08	1,373E-05
	Median ± Interquartile Range	0,890 ± 0,467	0,970 ± 0,776	0,711 ± 0,516	0,912 ± 0,816	0,821 ± 0,550	0,894 ± 0,695	0,702 ± 0,585	0,837 ± 0,745
L CG BA31	**p-value**	0,008	4,977E-08	0,003	7,775E-07	0,003	3,131E-08	0,004	6,082E-10
	Median ± Interquartile Range	0,814 ± 0,631	0,948 ± 0,732	0,687 ± 0,536	0,885 ± 0,581	0,764 ± 0,458	0,948 ± 0,886	0,826 ± 0,392	0,862 ± 0,820
L PC BA30	**p-value**	4,924E-09	4,959E-07	4,683E-08	1,374E-09	1,711E-09	8,606E-06	1,085E-07	8,903E-07
	Median ± Interquartile Range	0,739 ± 0,620	0,988 ± 0,728	0,622 ± 0,489	0,810 ± 0,986	0,661 ± 0,650	0,755 ± 0,976	0,569 ± 0,512	0,799 ± 1,043
L PrcL BA5	**p-value**	9,054E-07	5,470E-09	2,377E-05	4,188E-10	1,720E-06	5,003E-11	2,595E-06	6,564E-11
	Median ± Interquartile Range	0,815 ± 0,555	0,887 ± 0,764	0,776 ± 0,673	0,873 ± 0,841	0,837 ± 0,782	0,986 ± 0,794	0,792 ± 0,748	0,900 ± 0,782
L PrhG BA36	**p-value**	4,593E-06	1,689E-06	2,370E-08	7,351E-08	4,077E-06	5,797E-06	2,260E-09	1,602E-06
	Median ± Interquartile Range	0,623 ± 0,536	1,070 ± 1,006	0,550 ± 0,473	0,941 ± 0,870	0,675 ± 0,495	0,901 ± 1,025	0,537 ± 0,394	0,868 ± 0,965
R CG BA24	**p-value**	1,315E-05	1,262E-07	4,817E-08	8,795E-07	4,785E-06	2,750E-09	7,386E-08	3,710E-09
	Median ± Interquartile Range	0,873 ± 0,631	0,851 ± 0,899	0,773 ± 0,667	0,885 ± 0,894	0,743 ± 0,470	0,934 ± 0,859	0,727 ± 0,504	0,883 ± 0,781
R Insula BA13	**p-value**	1,231E-08	3,617E-05	2,687E-07	2,305E-08	5,113E-09	1,225E-07	1,180E-05	3,946E-06
	Median ± Interquartile Range	0,757 ± 0,537	1,123 ± 1,025	0,770 ± 0,628	1,061 ± 1,025	0,694 ± 0,654	0,998 ± 0,977	0,739 ± 0,598	0,963 ± 0,886
R PC BA23	**p-value**	3,098E-05	3,614E-06	4,519E-04	8,930E-04	3,416E-05	6,173E-05	3,063E-05	1,675E-06
	Median ± Interquartile Range	0,902 ± 0,639	0,974 ± 0,590	0,910 ± 0,704	0,967 ± 0,789	0,811 ± 0,656	0,964 ± 0,814	0,792 ± 0,687	0,959 ± 0,652
R PrecG BA4	**p-value**	3,529E-02	5,877E-06	3,798E-04	6,674E-07	0,019	1,842E-05	8,574E-07	2,211E-06
	Median ± Interquartile Range	1,098 ± 1,048	0,897 ± 1,302	0,986 ± 0,966	0,937 ± 0,918	1,149 ± 0,821	0,842 ± 1,104	0,931 ± 0,880	0,820 ± 0,935
R PrecG BA43	**p-value**	0,054	7,574E-08	0,024	5,114E-05	0,011	2,378E-07	0,049	5,292E-07
	Median ± Interquartile Range	0,786 ± 0,353*	0,904 ± 0,769	0,654 ± 0,282	1,018 ± 1,006	0,678 ± 0,469	1,076 ± 0,705	0,655 ± 0,511	0,931 ± 1,011
R PrimSens BA1	**p-value**	3,56E-06	0,072	0,003	0,009	0,001	9,259E-05	0,013	0,004
	Median ± Interquartile Range	0,715 ± 0,653	1,124 ± 0,637*	0,871 ± 0,736	1,096 ± 0,989	0,850 ± 0,749	0,861 ± 0,886	0,863 ± 0,718	1,031 ± 1,075
R STG BA39	**p-value**	3,143E-12	5,176E-06	2,107E-08	1,359E-06	7,676E-11	2,395E-08	1,709E-08	4,758E-10
	Median ± Interquartile Range	0,853 ± 0,671	1,007 ± 0,543	0,805 ± 0,521	1,018 ± 0,707	0,858 ± 0,717	0,931 ± 0,991	0,788 ± 0,533	0,863 ± 0,733

*: represents the average and standard-deviation of the HRF parameters which did not reject the null hypothesis of the Shapiro-Wilk test, and therefore owned a normal distribution.

Table A.3: Wilcoxon rank-sum test's adjusted p-values (FDR = 0.10) in each HRF parameter of each condition per ROI - Negative signal change ROIs.

		HRF peak amplitude (beta weights)		HRF peak latency (s)	
		Threshold	Submaximum	Threshold	Submaximum
L AC BA32	**Adjusted p-value (FDR = 0,10)**	0,570	0,021	0,893	0,963
L CG BA31	**Adjusted p-value (FDR = 0,10)**	0,303	0,196	4,410E-04	0,461
L PC BA30	**Adjusted p-value (FDR = 0,10)**	0,101	0,024	0,071	0,008
L PrcL BA5	**Adjusted p-value (FDR = 0,10)**	0,818	0,913	0,324	0,734
L PrhG BA36	**Adjusted p-value (FDR = 0,10)**	2,179E-06	9,446E-06	0,180	0,004
R CG BA24	**Adjusted p-value (FDR = 0,10)**	0,457	0,113	0,056	0,098
R Insula BA13	**Adjusted p-value (FDR = 0,10)**	0,143	0,078	0,106	0,091
R PC BA23	**Adjusted p-value (FDR = 0,10)**	0,498	0,699	0,099	0,588
R PrecG BA4	**Adjusted p-value (FDR = 0,10)**	0,841	1,478	0,954	2,077
R PrecG BA43	**Adjusted p-value (FDR = 0,10)**	0,005	0,004	0,942	0,453
R PrimSens BA1	**Adjusted p-value (FDR = 0,10)**	0,101	0,051	0,006	0,017
R STG BA39	**Adjusted p-value (FDR = 0,10)**	0,473	0,076	0,330	0,755

		HRF relative slope to peak (beta weights/s)		HRF AUC (a.u.)	
		Threshold	Submaximum	Threshold	Submaximum
L AC BA32	Adjusted p-value (FDR = 0,10)	0,474	0,010	0,346	0,145
L CG BA31	Adjusted p-value (FDR = 0,10)	0,001	0,540	0,004	0,029
L PC BA30	Adjusted p-value (FDR = 0,10)	0,094	0,780	0,052	0,009
L PrcL BA5	Adjusted p-value (FDR = 0,10)	0,158	0,608	0,277	0,416
L PrhG BA36	Adjusted p-value (FDR = 0,10)	0,153	0,179	6,697E-06	9,743E-05
R CG BA24	Adjusted p-value (FDR = 0,10)	0,042	0,052	0,034	0,101
R Insula BA13	Adjusted p-value (FDR = 0,10)	0,114	0,366	0,021	0,065
R PC BA23	Adjusted p-value (FDR = 0,10)	0,091	0,479	0,086	0,561
R PrecG BA4	Adjusted p-value (FDR = 0,10)	1,182	3,585	0,902	1,118
R PrecG BA43	Adjusted p-value (FDR = 0,10)	0,860	0,536	2,240E-04	3,784E-05
R PrimSens BA1	Adjusted p-value (FDR = 0,10)	0,525	0,952	0,072	0,041
R STG BA39	Adjusted p-value (FDR = 0,10)	0,473	0,066	0,376	0,269

		HRF PCSA (a.u.)		HRF NCSA (a.u.)	
		Threshold	Submaximum	Threshold	Submaximum
L AC BA32	Adjusted p-value (FDR = 0,10)	0,532	0,016	0,519	0,042
L CG BA31	Adjusted p-value (FDR = 0,10)	0,096	0,018	0,006	0,153
L PC BA30	Adjusted p-value (FDR = 0,10)	0,093	0,030	0,087	0,007
L PrcL BA5	Adjusted p-value (FDR = 0,10)	0,317	0,639	0,269	0,526
L PrhG BA36	Adjusted p-value (FDR = 0,10)	1,562E-05	5,121E-05	2,404E-04	2,436E-05
R CG BA24	Adjusted p-value (FDR = 0,10)	0,256	0,072	0,038	0,112
R Insula BA13	Adjusted p-value (FDR = 0,10)	0,027	0,078	0,021	0,047
R PC BA23	Adjusted p-value (FDR = 0,10)	0,546	0,671	0,108	0,604
R PrecG BA4	Adjusted p-value (FDR = 0,10)	0,962	0,922	1,013	1,028
R PrecG BA43	Adjusted p-value (FDR = 0,10)	0,017	2,240E-04	3,639E-05	0,004
R PrimSens BA1	Adjusted p-value (FDR = 0,10)	0,099	0,041	0,533	0,092
R STG BA39	Adjusted p-value (FDR = 0,10)	0,421	0,063	0,361	0,195

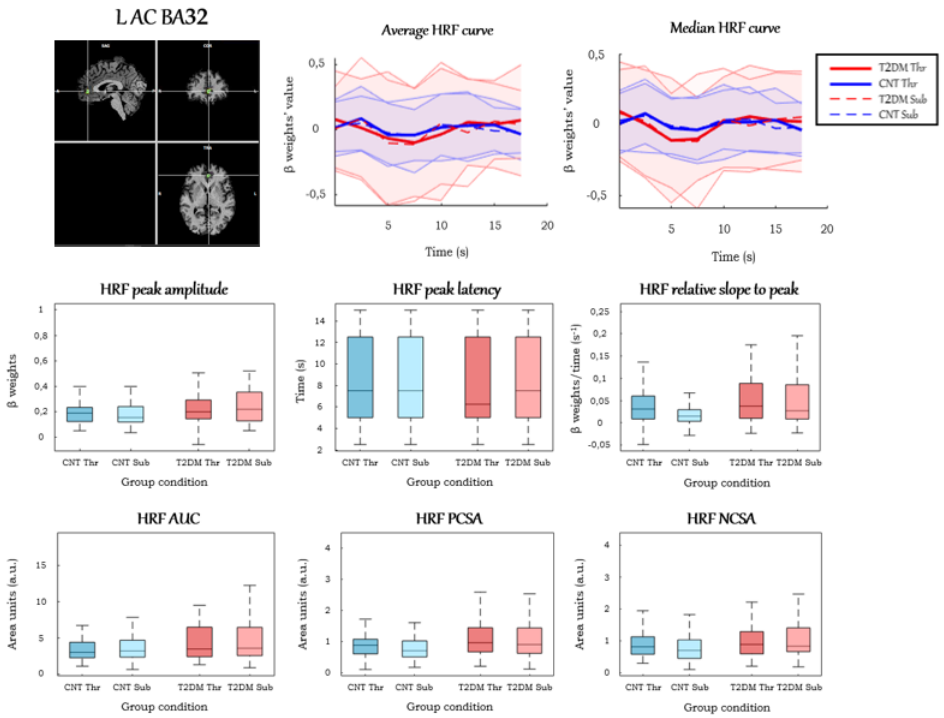

Figure A.4: Average and median HRFs and HRF parameters: L AC BA32.

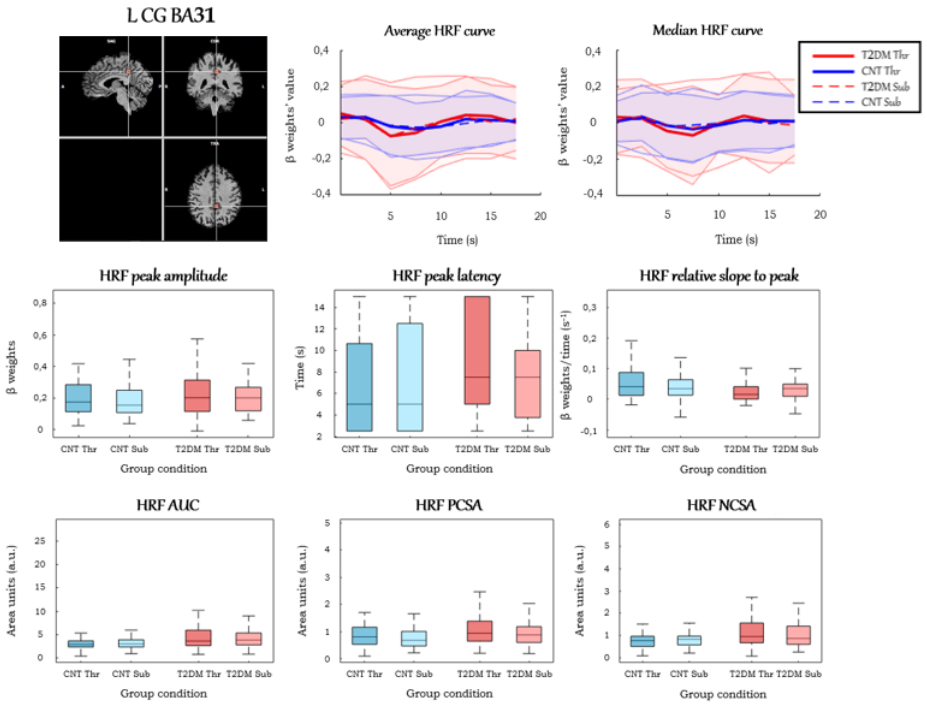

Figure A.5: Average and median HRFs and HRF parameters: L CG BA31.

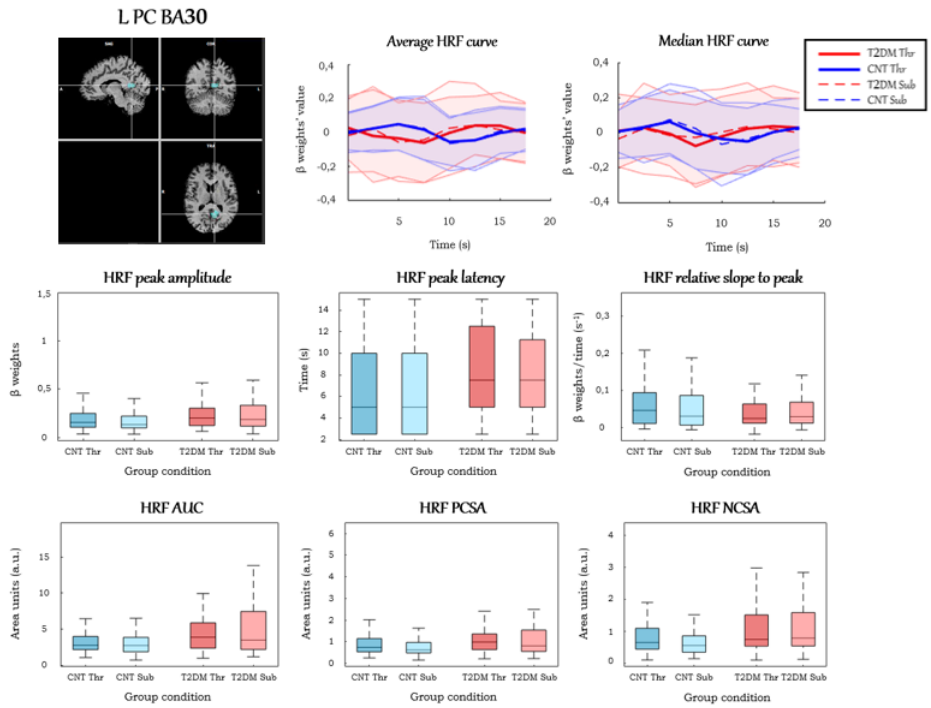

Figure A.6: Average and median HRFs and HRF parameters: L PC BA30.

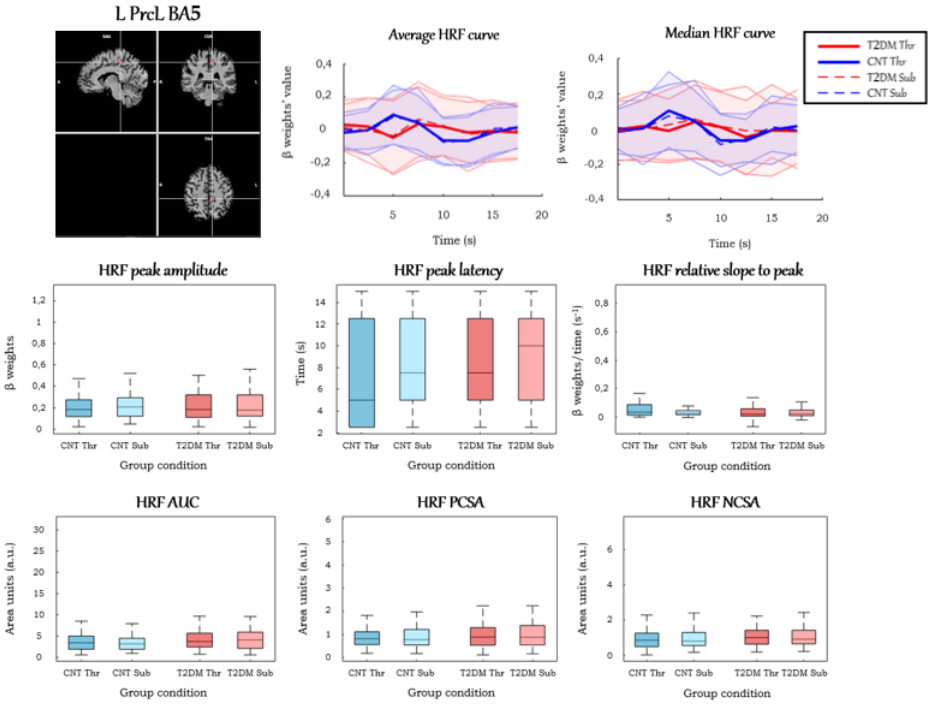

Figure A.7: Average and median HRFs and HRF parameters: L PrcL BA5.

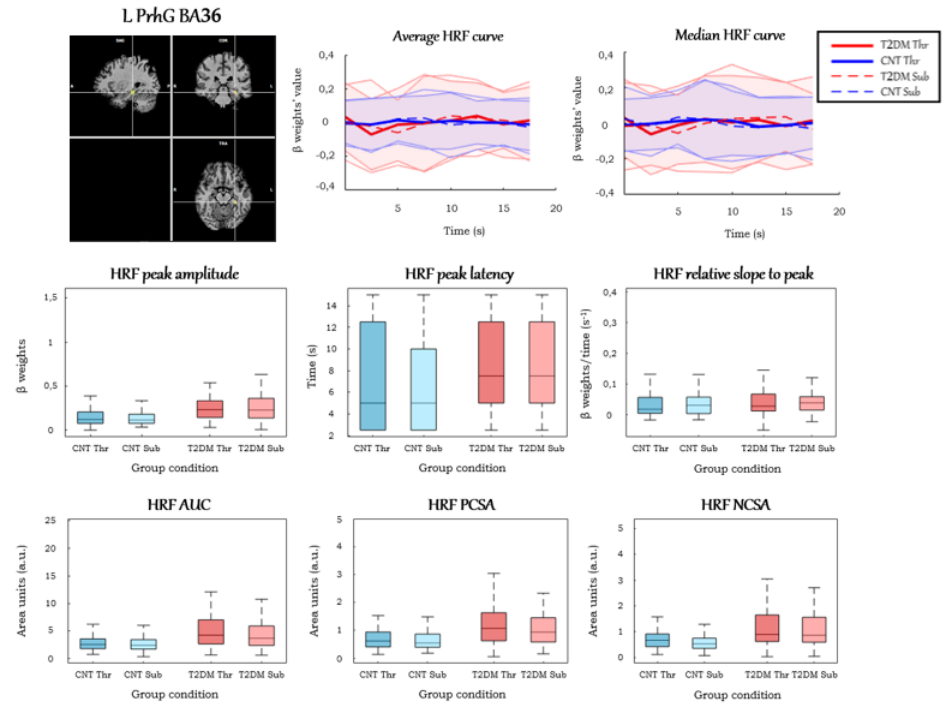

Figure A.8: Average and median HRFs and HRF parameters: L PrhG BA36.

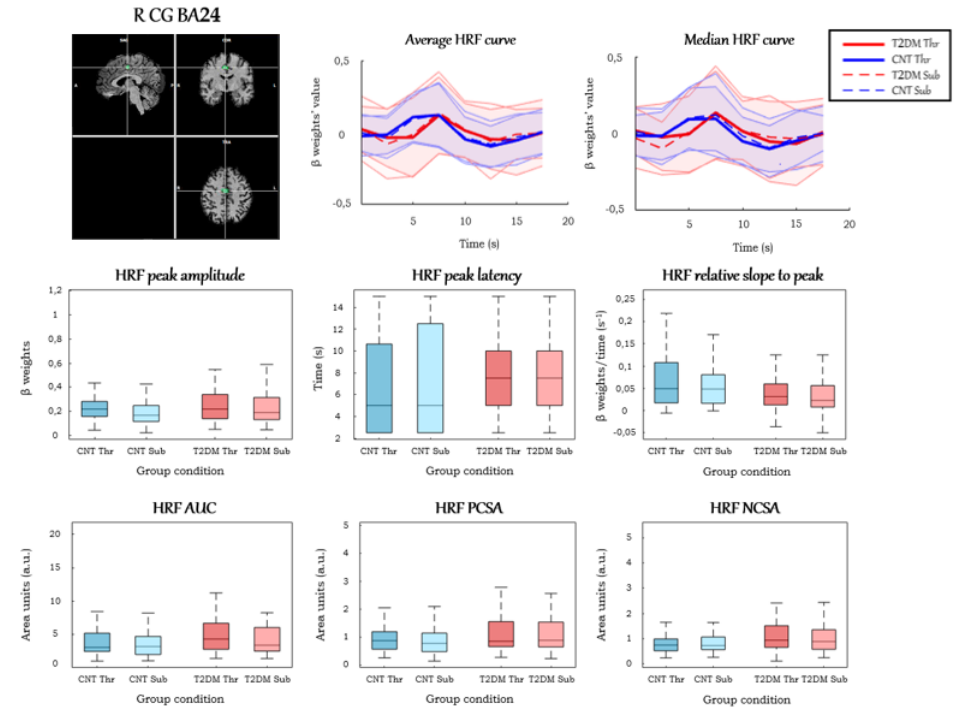

Figure A.9: Average and median HRFs and HRF parameters: R CG BA24.

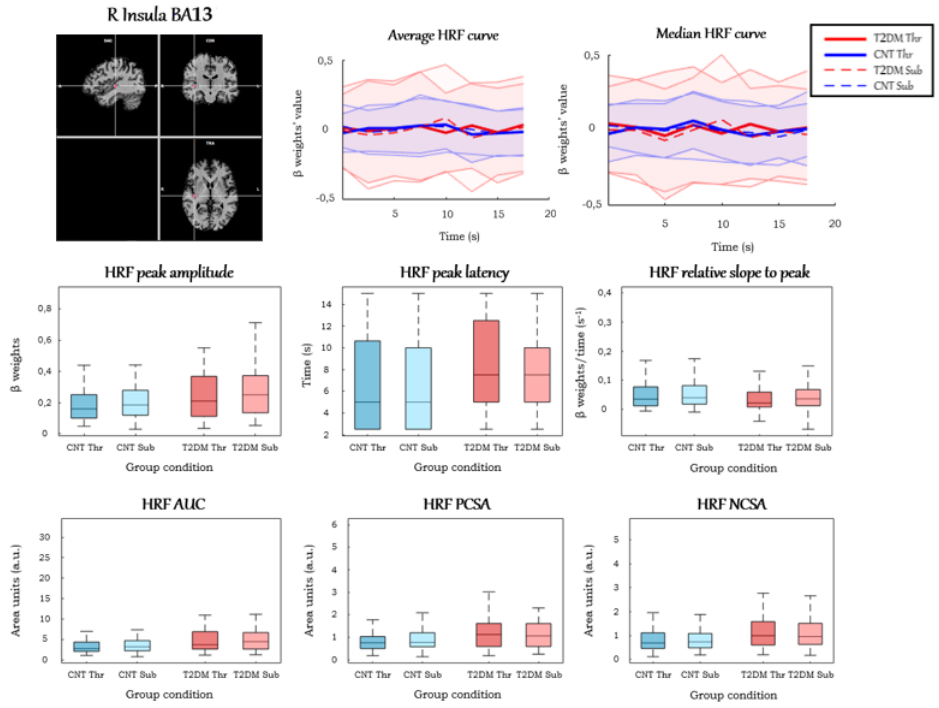

Figure A.10: Average and median HRFs and HRF parameters: R Insula BA13.

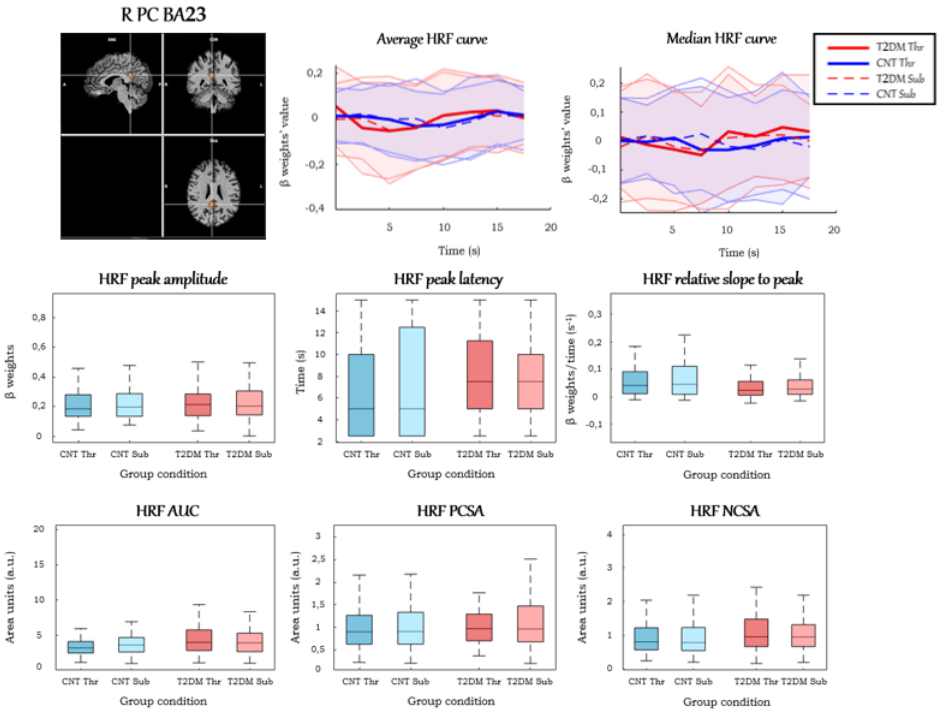

Figure A.11: Average and median HRFs and HRF parameters: R PC BA23.

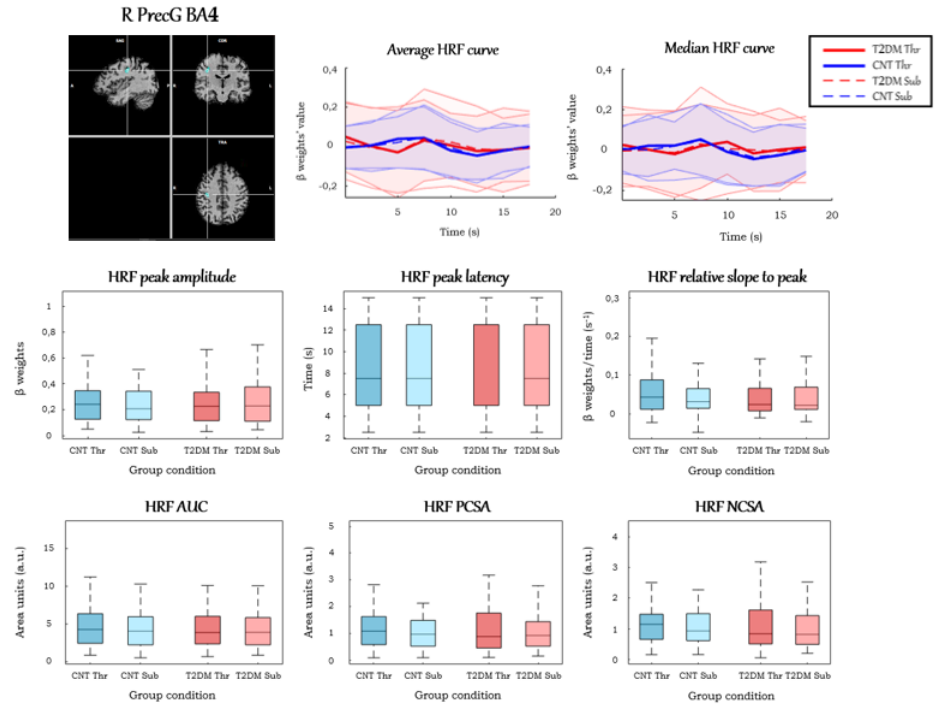

Figure A.12: Average and median HRFs and HRF parameters: R PrecG BA4.

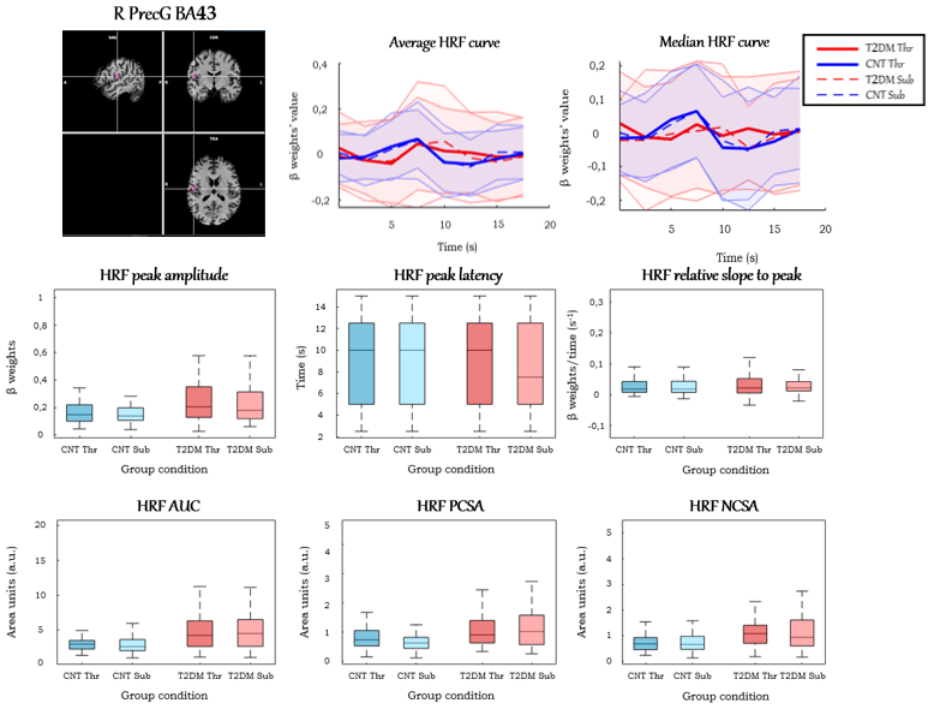

Figure A.13: Average and median HRFs and HRF parameters: R PrecG BA43.

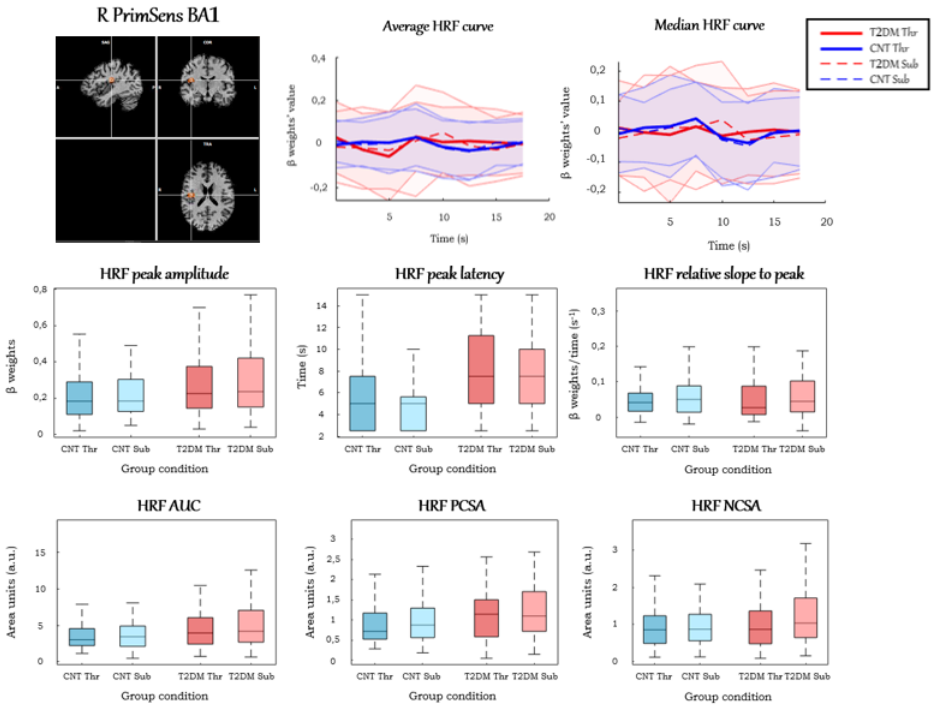

Figure A.14: Average and median HRFs and HRF parameters: R PrimSens BA1.

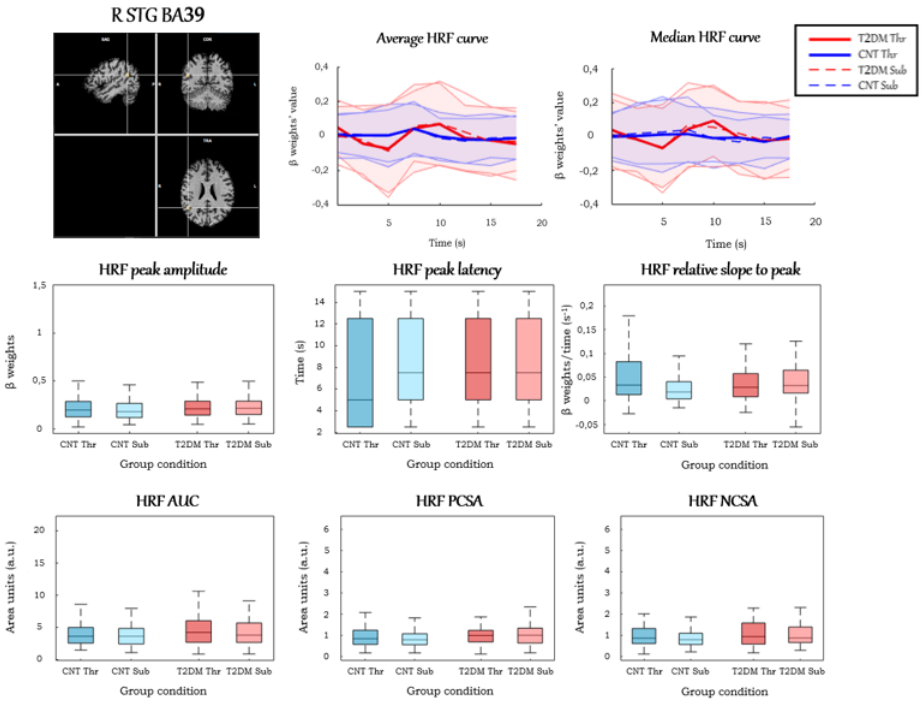

Figure A.15: Average and median HRFs and HRF parameters: R STG BA39.

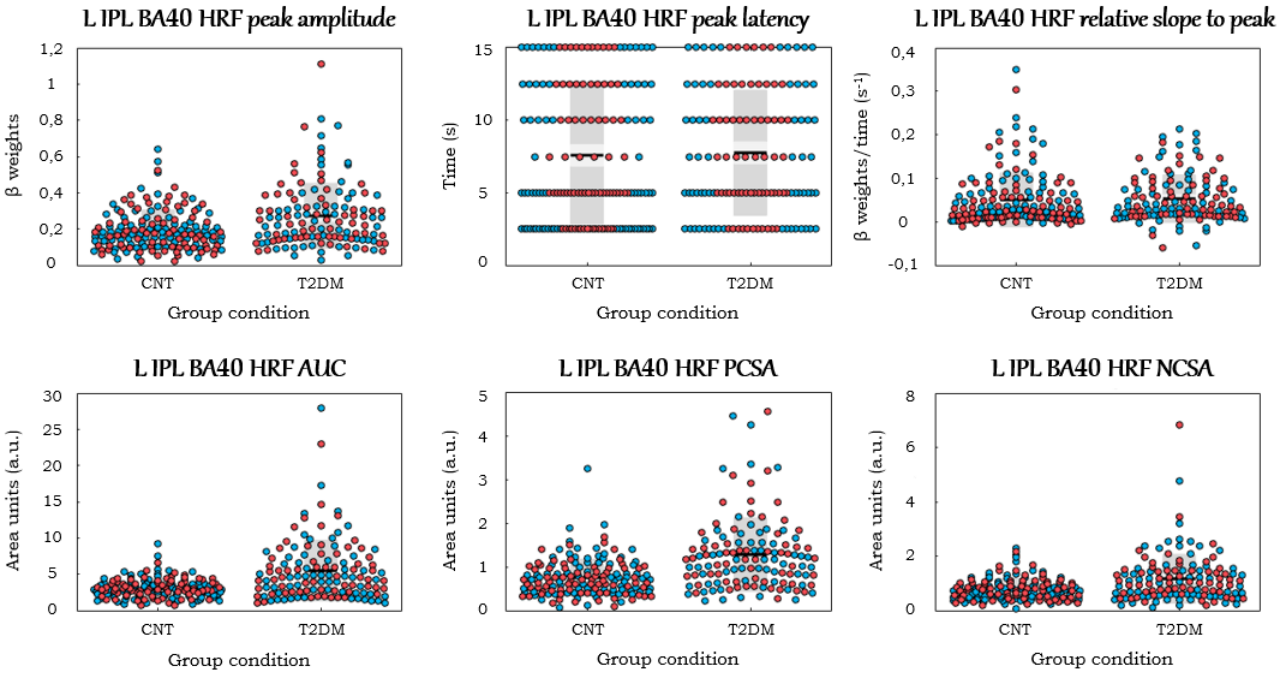

Figure A.16: Univariate scatterplots of the HRF parameters in L IPL BA40.

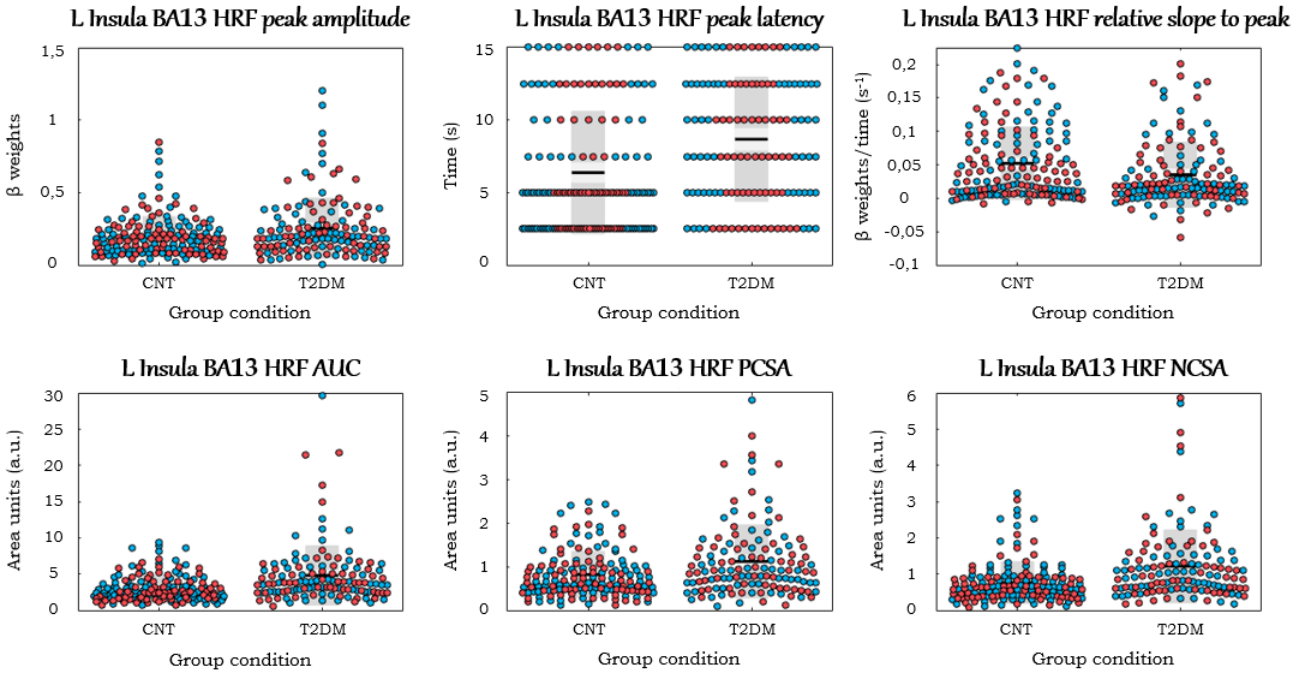

Figure A.17: Univariate scatterplots of the HRF parameters in L Insula BA13.

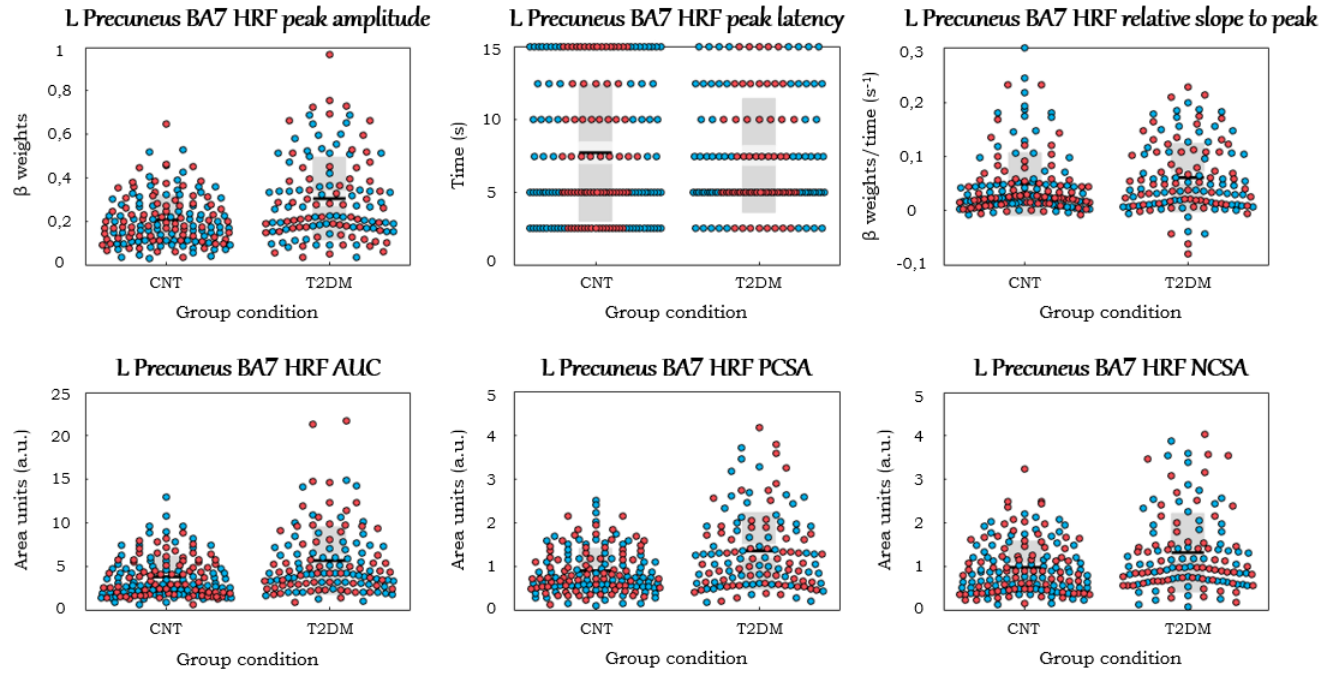

Figure A.18: Univariate scatterplots of the HRF parameters in L Precuneus BA7.

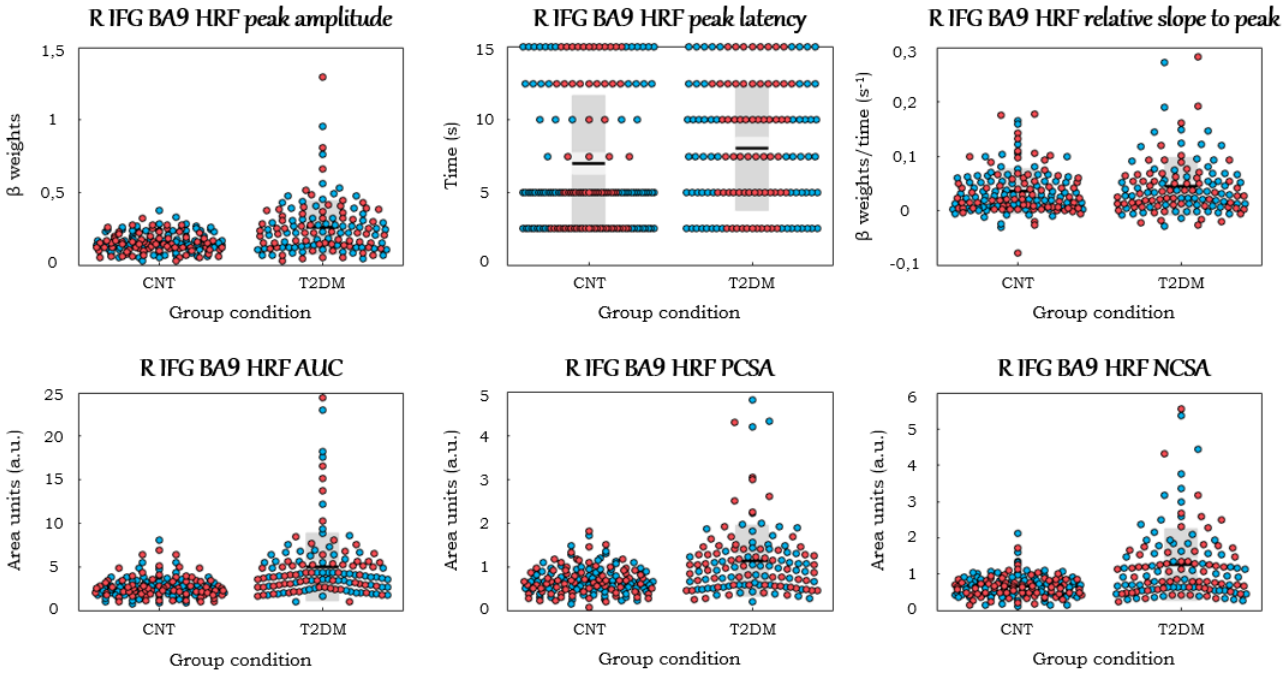

Figure A.19: Univariate scatterplots of the HRF parameters in R IFG BA9.

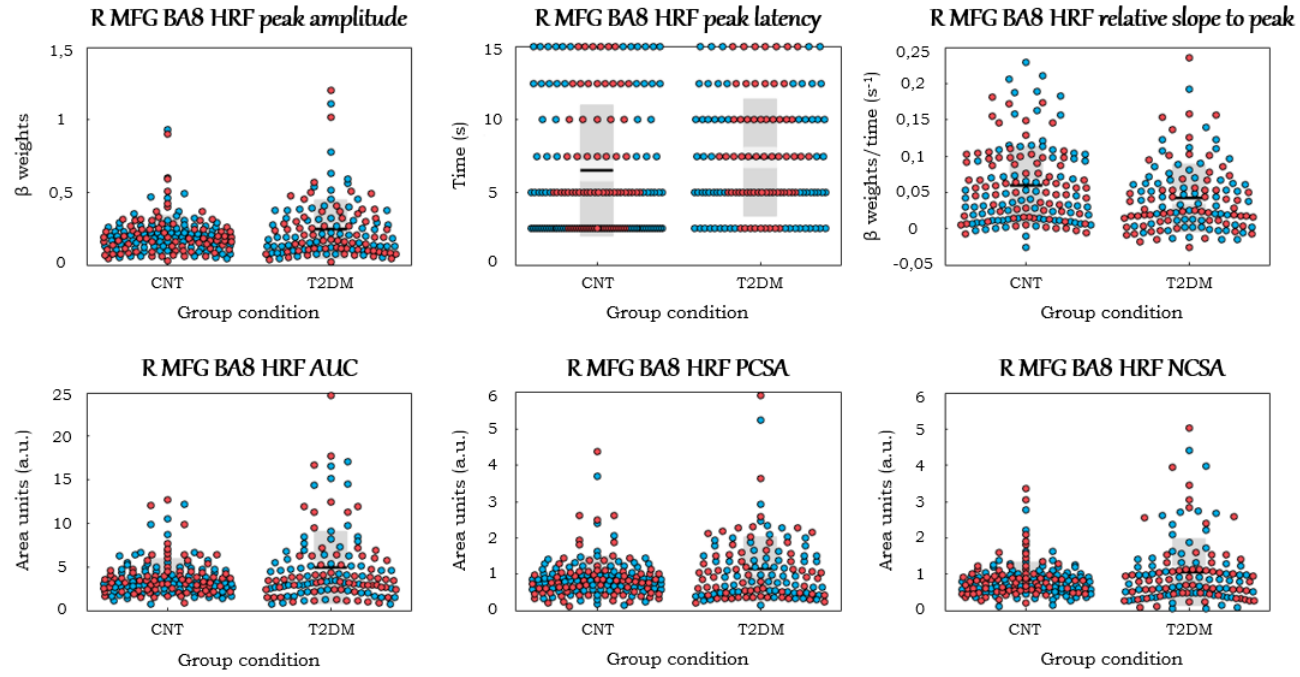

Figure A.20: Univariate scatterplots of the HRF parameters in R MFG BA8.

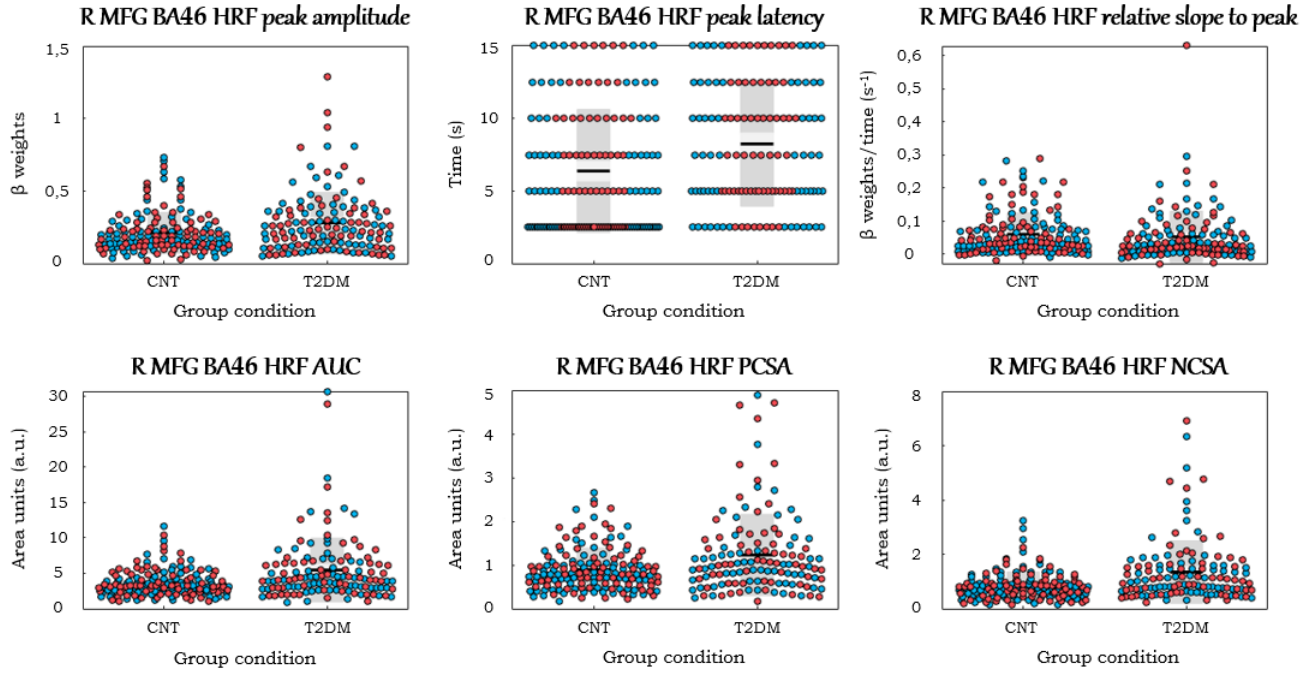

Figure A.21: Univariate scatterplots of the HRF parameters in R MFG BA46.

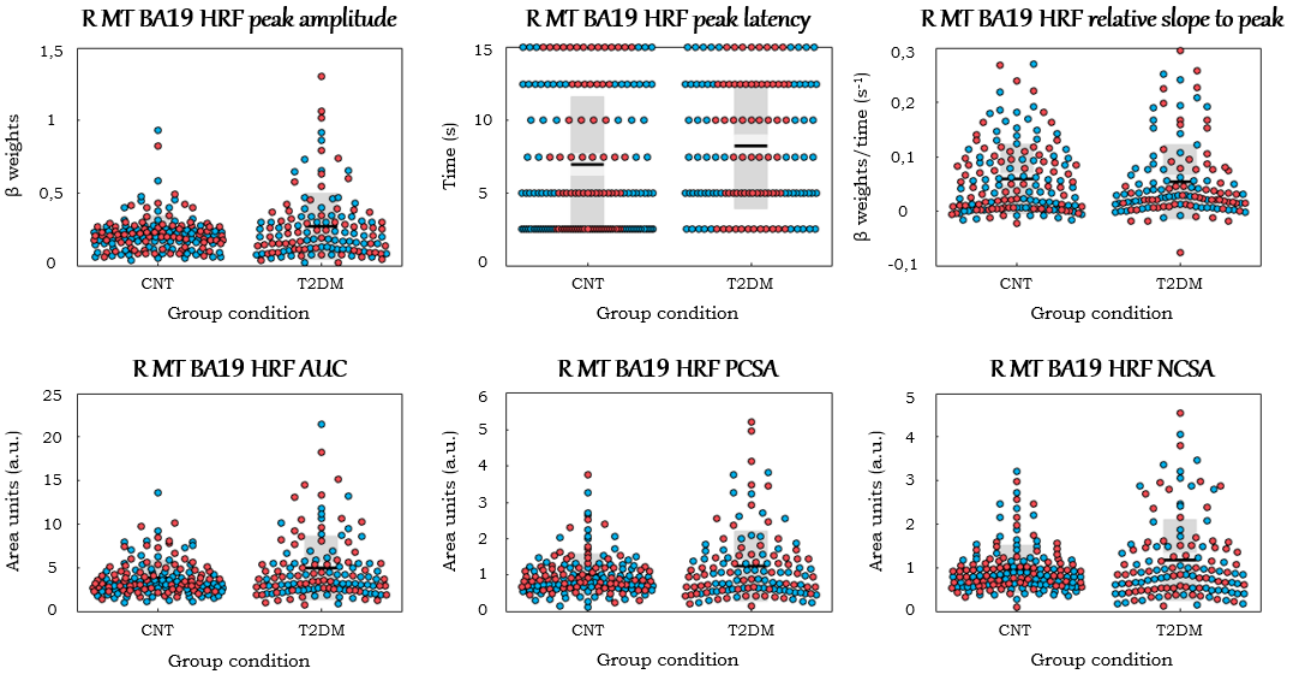

Figure A.22: Univariate scatterplots of the HRF parameters in R MT BA19.

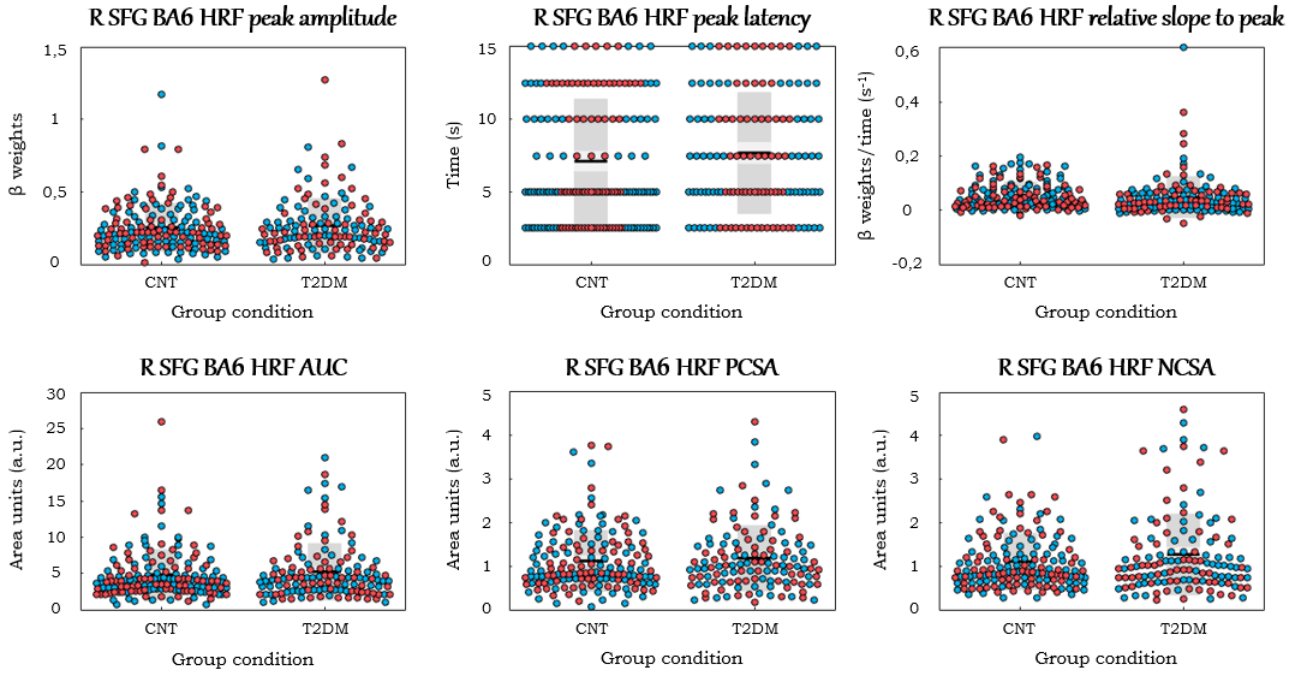

Figure A.23: Univariate scatterplots of the HRF parameters in R SFG BA6.

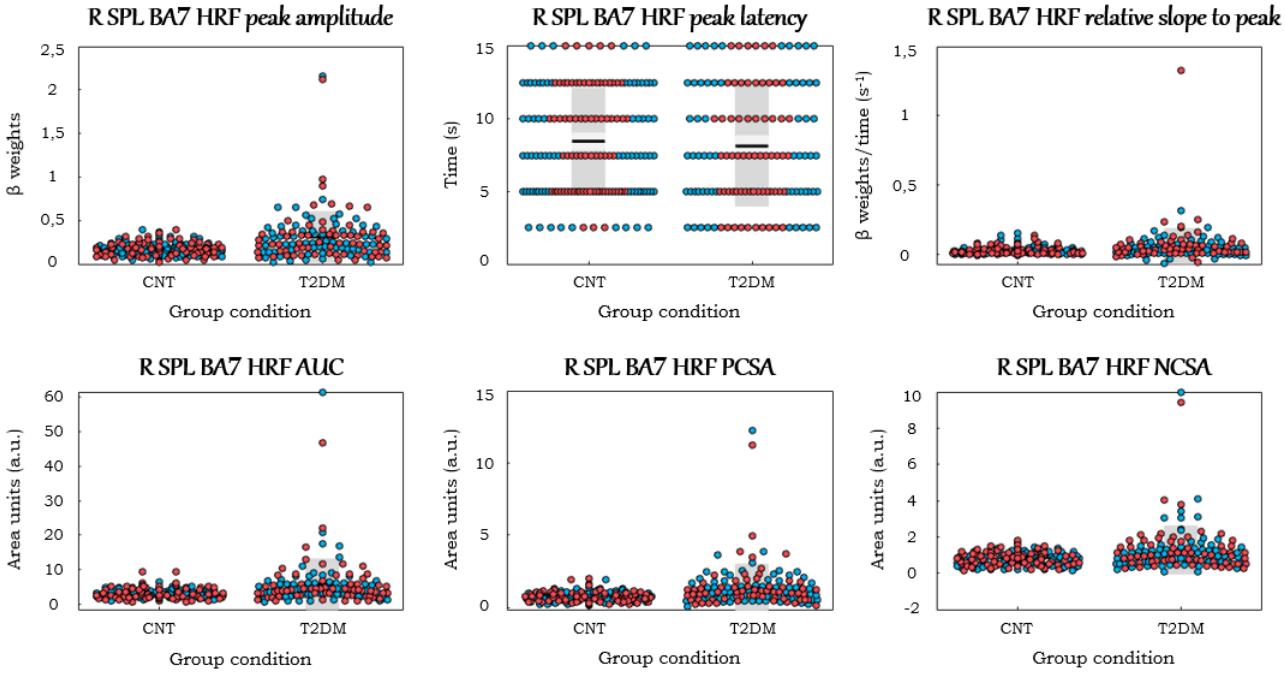

Figure A.24: Univariate scatterplots of the HRF parameters in R SPL BA7.

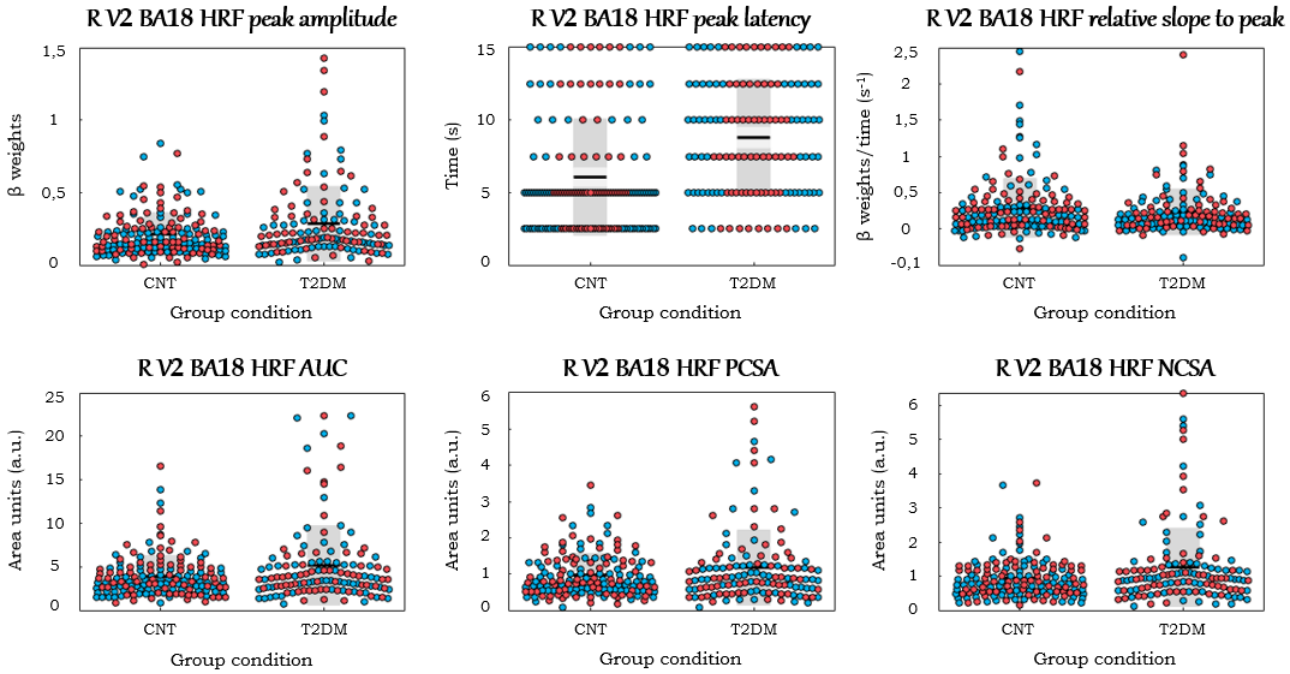

Figure A.25: Univariate scatterplots of the HRF parameters in R V2 BA18.

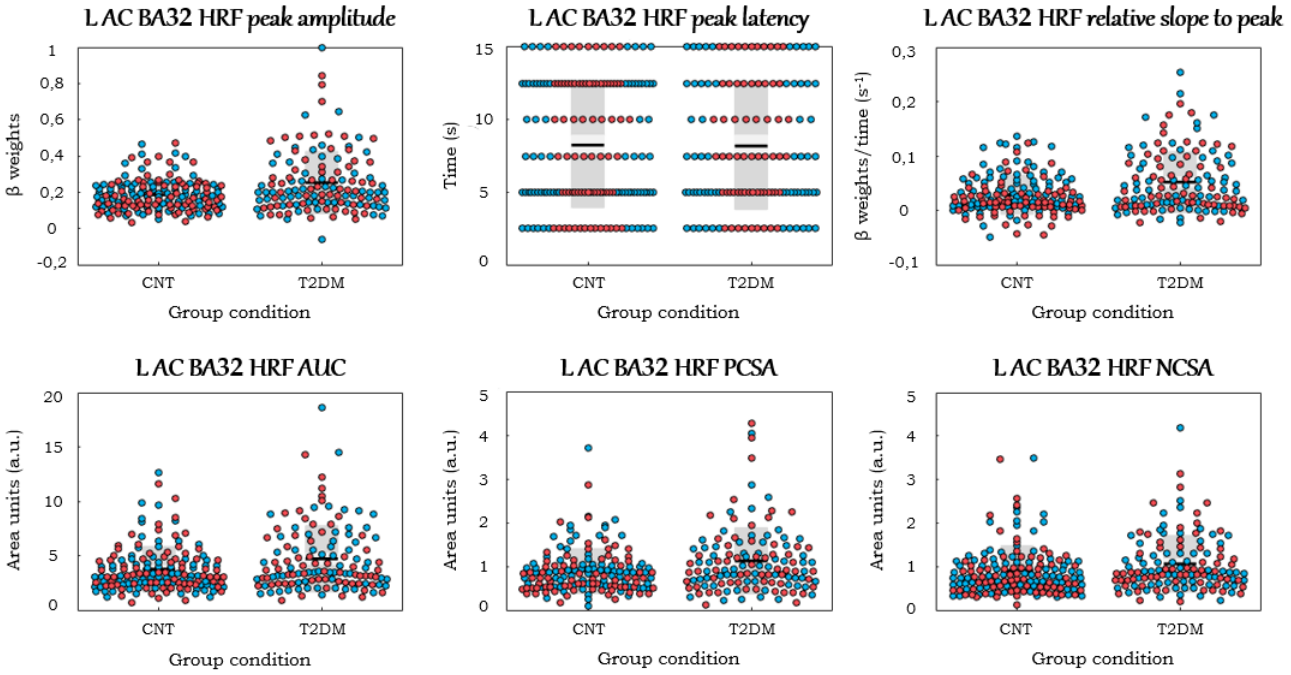

Figure A.26: Univariate scatterplots of the HRF parameters in L AC BA32.

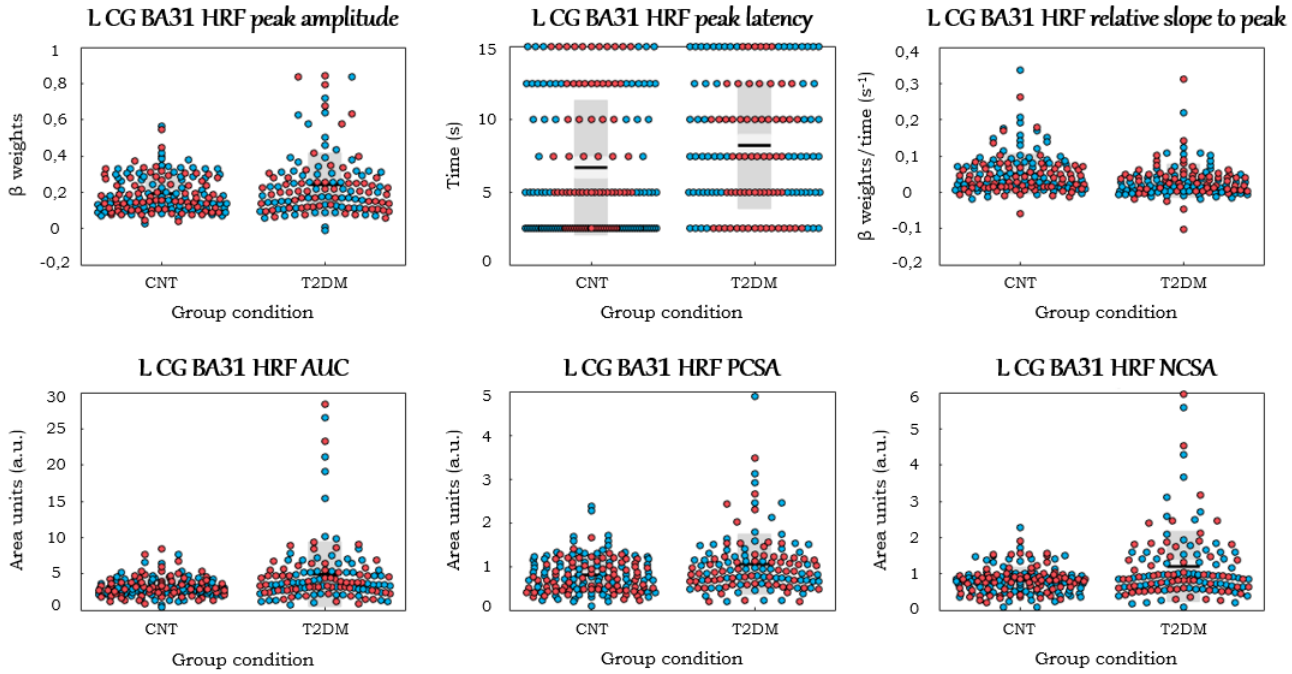

Figure A.27: Univariate scatterplots of the HRF parameters in L CG BA31.

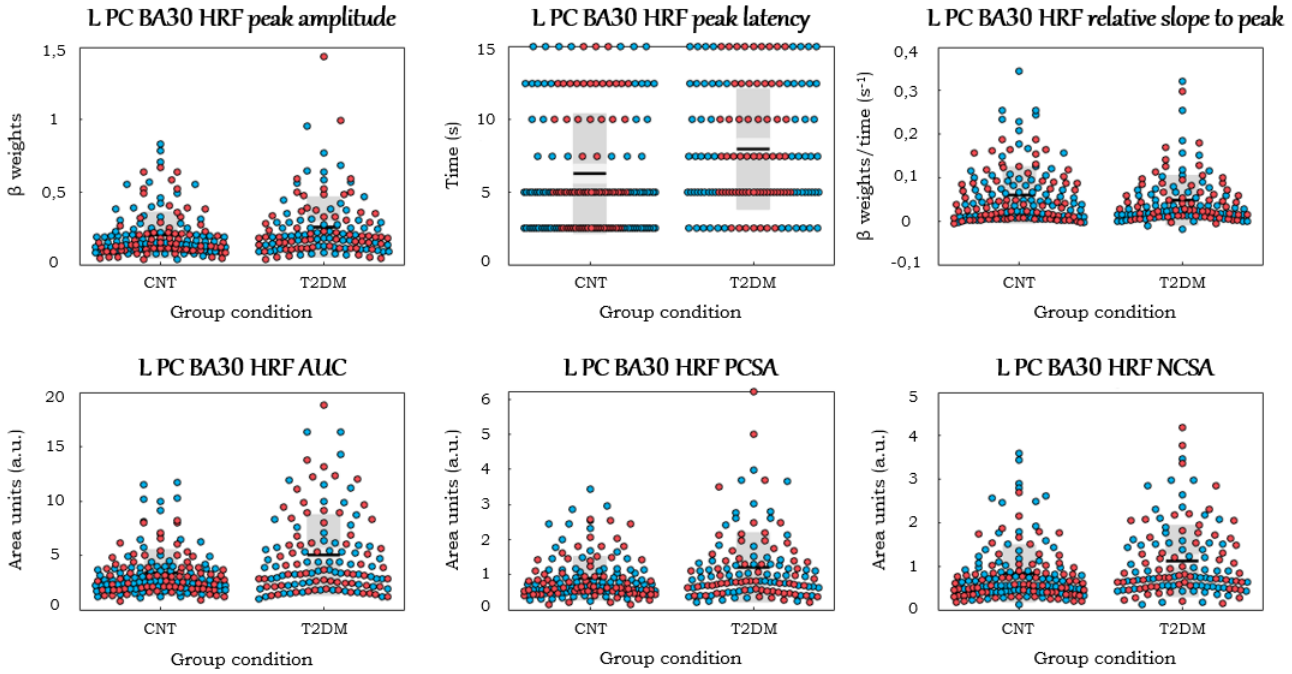

Figure A.28: Univariate scatterplots of the HRF parameters in L PC BA30.

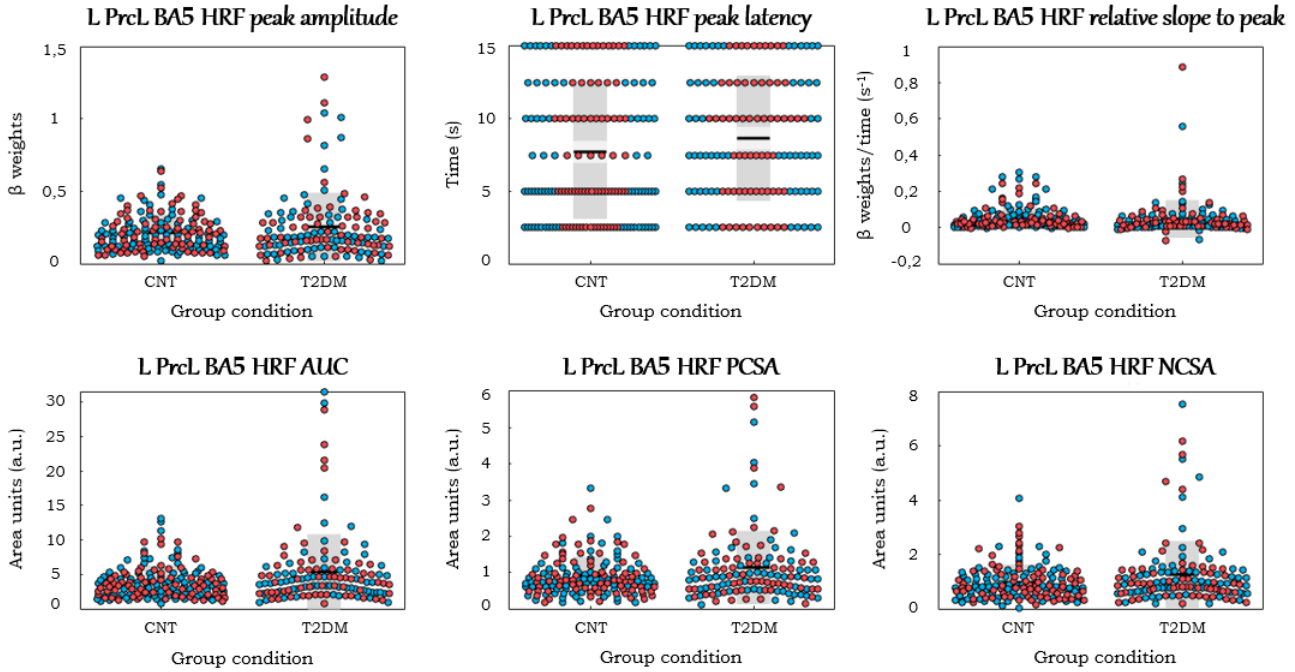

Figure A.29: Univariate scatterplots of the HRF parameters in L PrcL BA5.

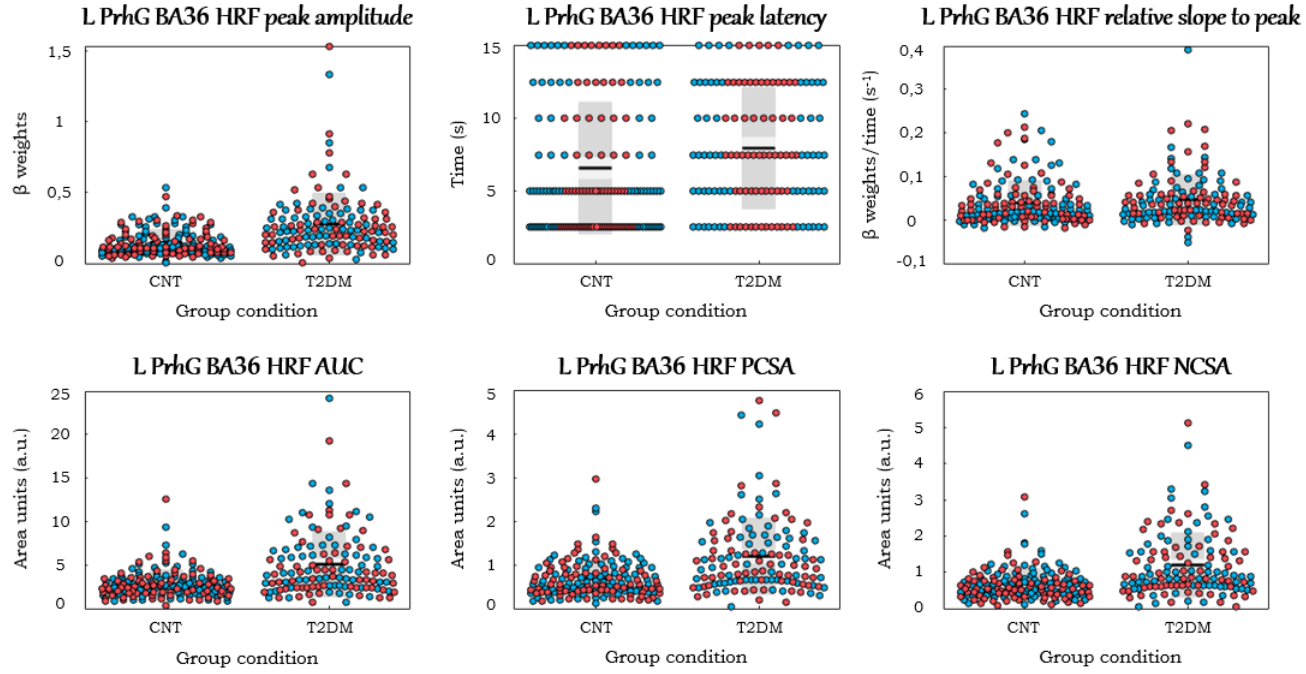

Figure A.30: Univariate scatterplots of the HRF parameters in L PrhG BA36.

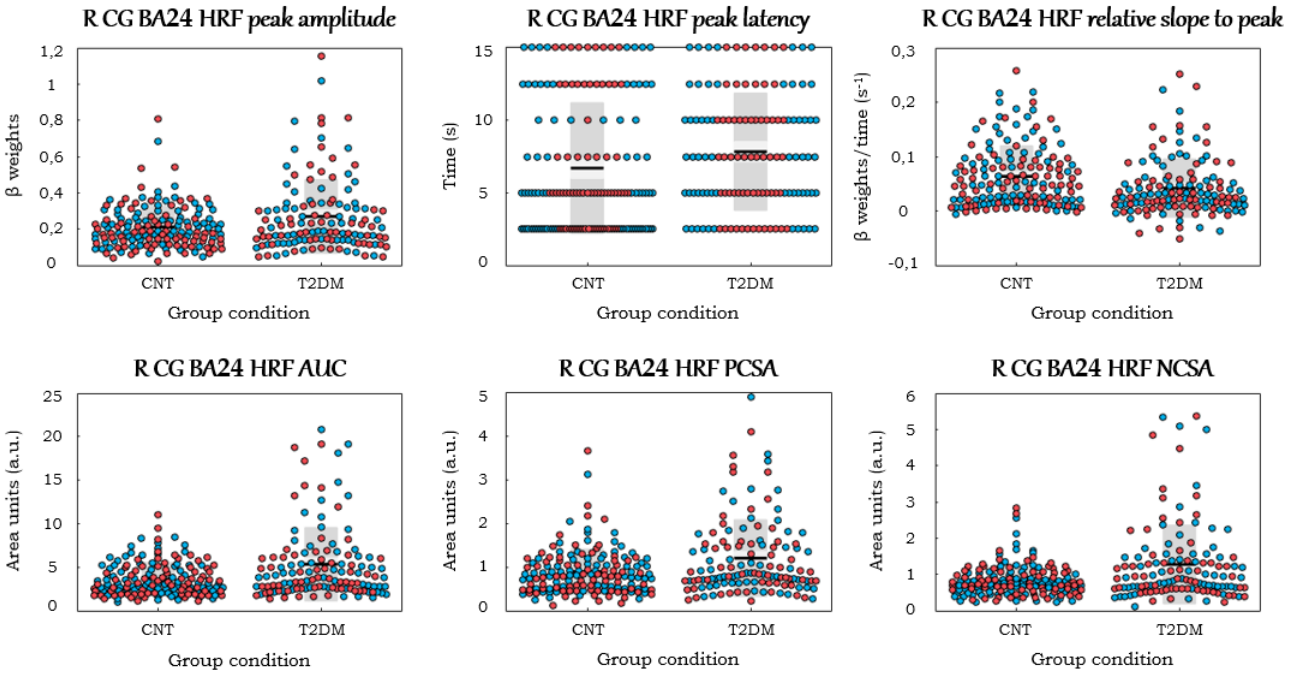

Figure A.31: Univariate scatterplots of the HRF parameters in R CG BA24.

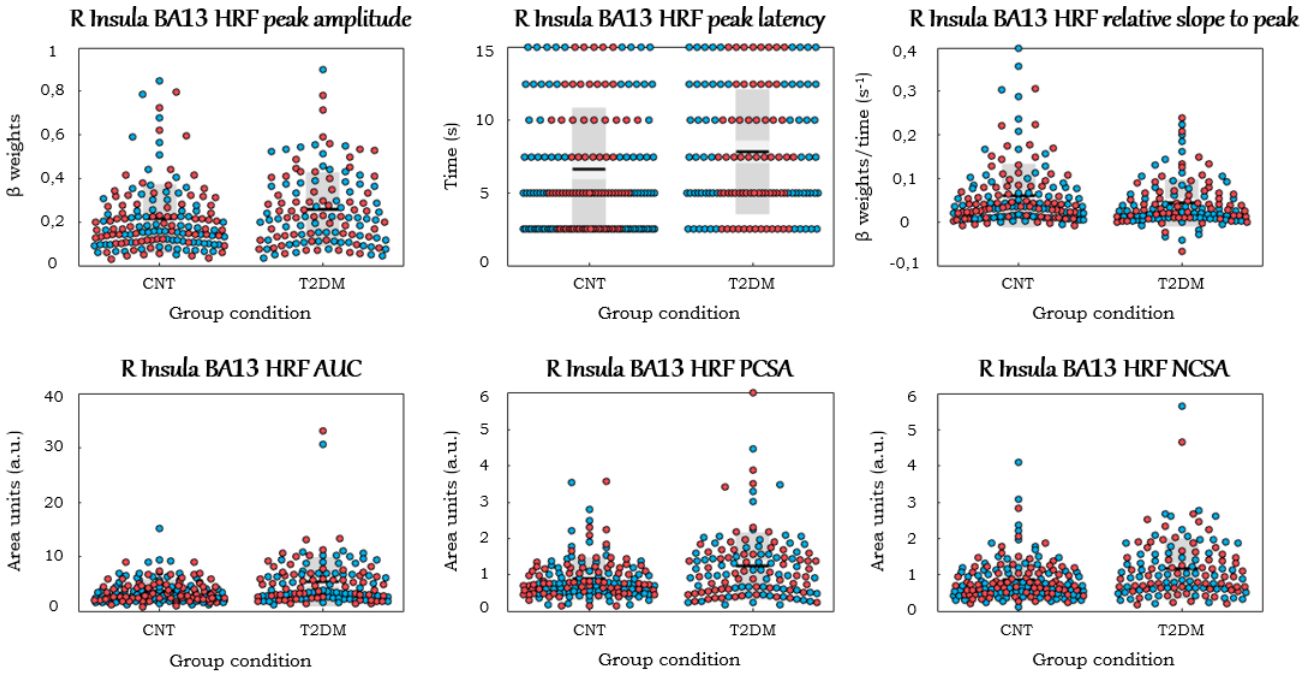

Figure A.32: Univariate scatterplots of the HRF parameters in R Insula BA13.

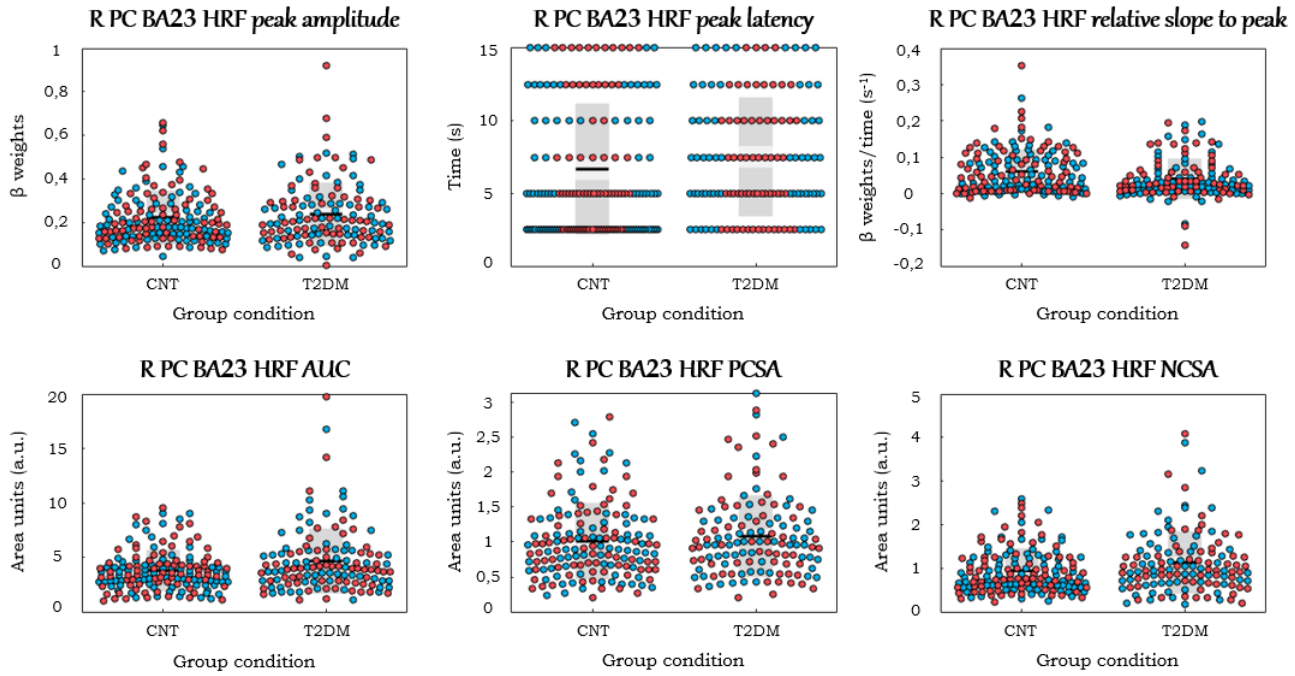

Figure A.33: Univariate scatterplots of the HRF parameters in R PC BA23.

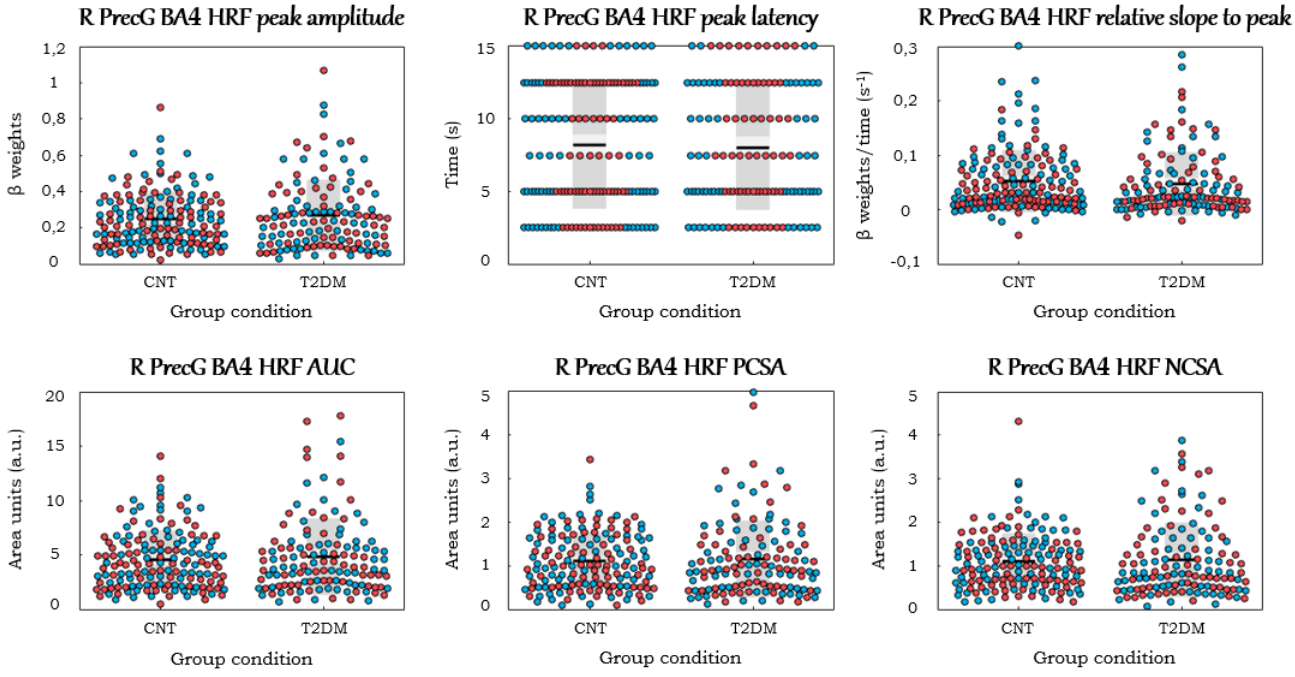

Figure A.34: Univariate scatterplots of the HRF parameters in R PrecG BA4.

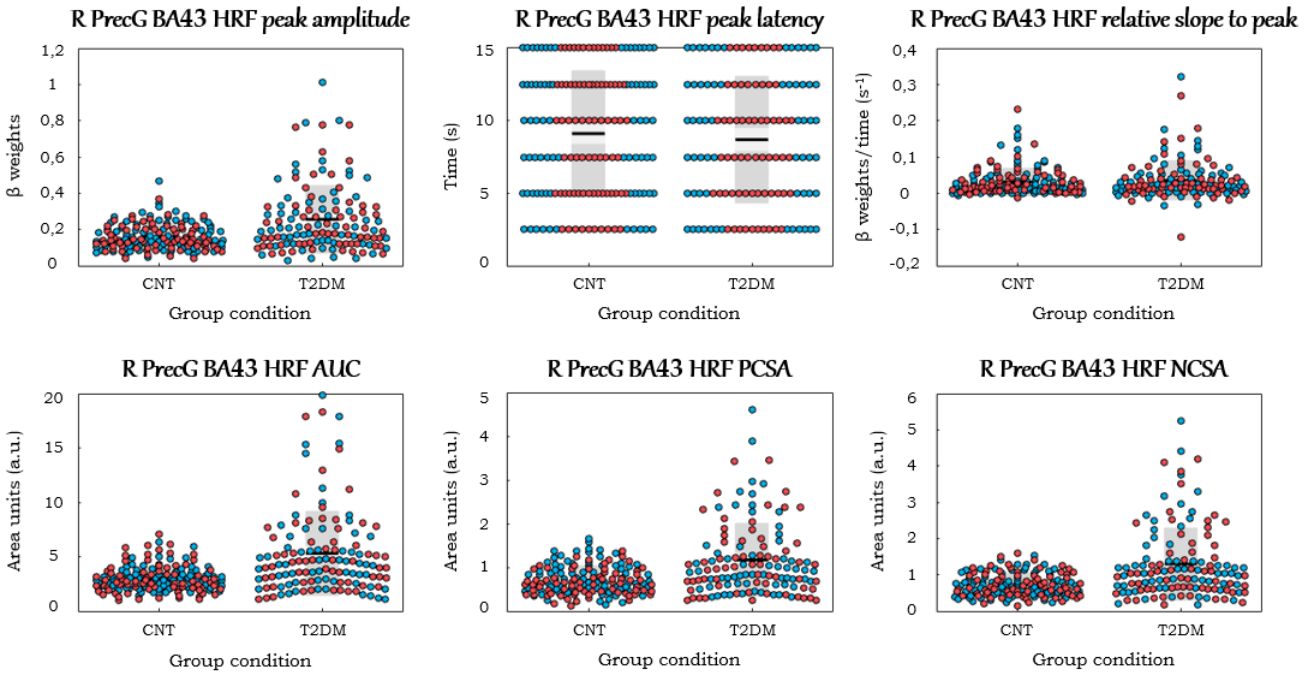

Figure A.35: Univariate scatterplots of the HRF parameters in R PrecG BA43.

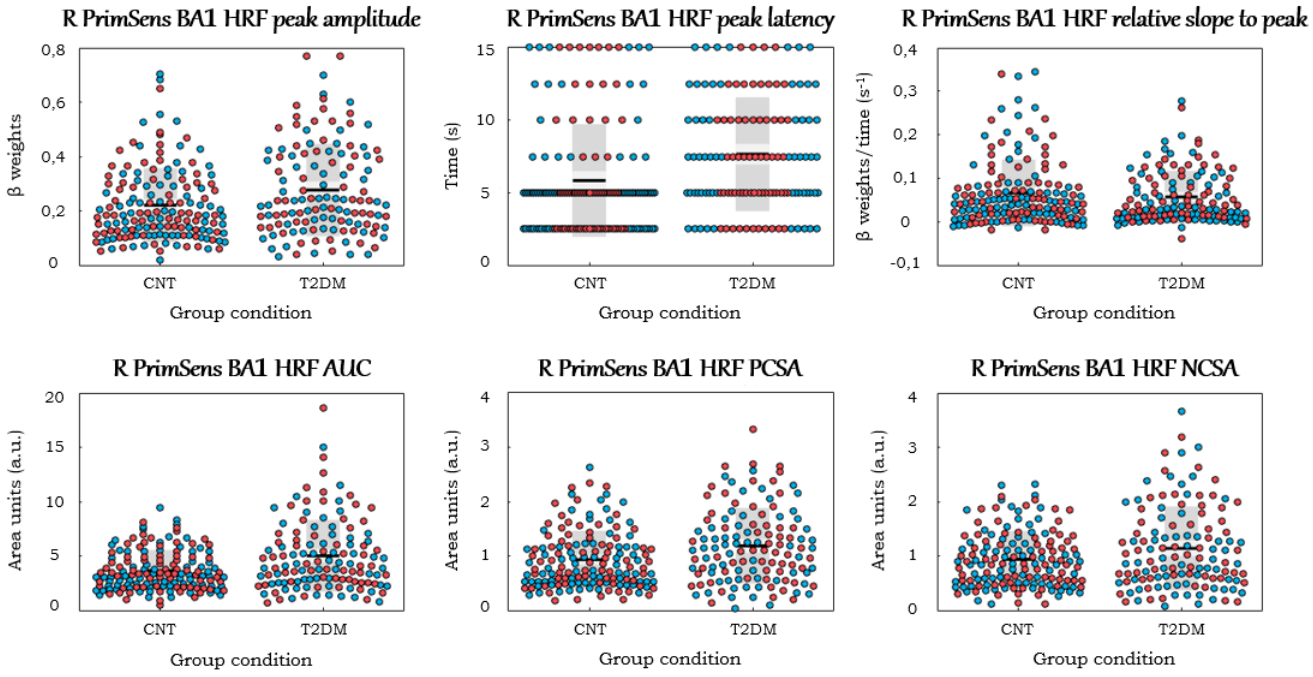

Figure A.36: Univariate scatterplots of the HRF parameters in R PrimSens BA1.

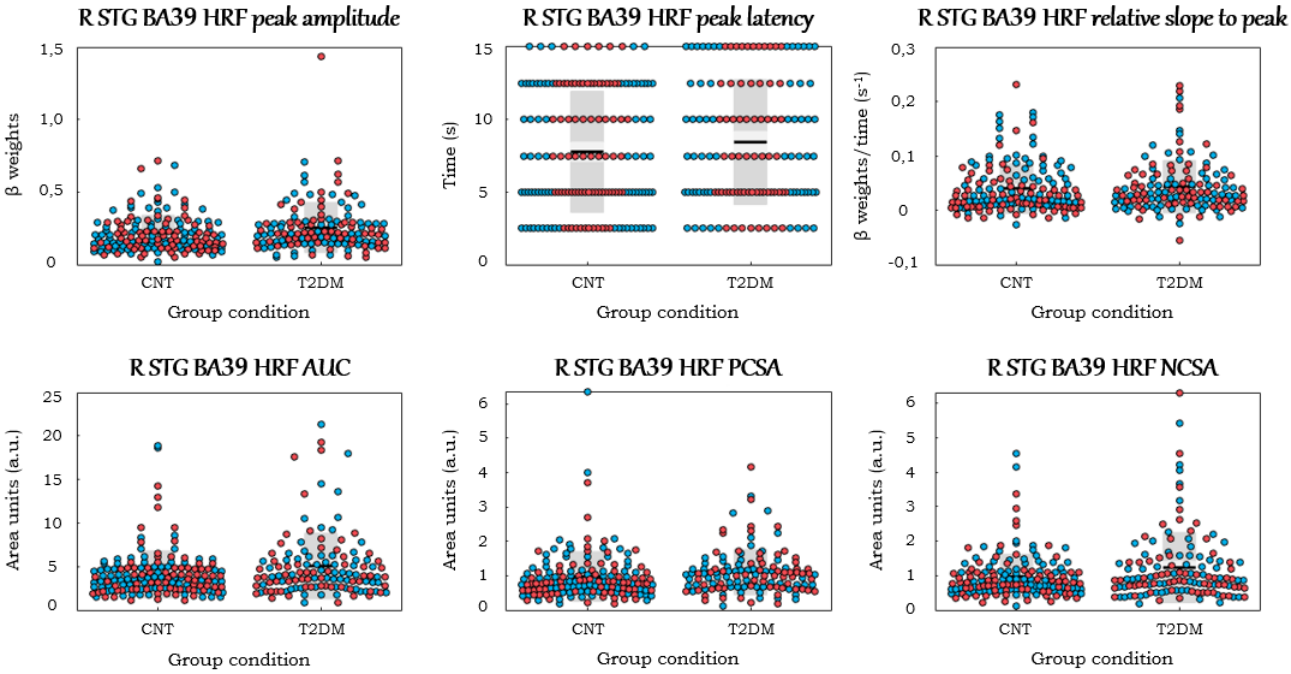

Figure A.37: Univariate scatterplots of the HRF parameters in R STG BA39.